

1 LEVERAGING MULTI-MESSENGER ASTROPHYSICS FOR DARK MATTER SEARCHES

By

Daniel Nicholas Salazar-Gallegos

A DISSERTATION

Submitted to  
Michigan State University  
in partial fulfillment of the requirements  
for the degree of

Physics—Doctor of Philosophy  
Computational Mathematics in Science and Engineering—Dual Major

Today

**ABSTRACT**

3 I did Dark Matter with HAWC and IceCube. I also used Graph Neural Networks

<sup>4</sup> Copyright by

<sup>5</sup> DANIEL NICHOLAS SALAZAR-GALLEGOS

<sup>6</sup> Today

## ACKNOWLEDGMENTS

8 I love my friends. Thanks to everyone that helped me figure this out. Amazing thanks to the people  
9 at LANL who supported me. Eames, etc Dinner Parties Jenny and her child Kaydince Kirsten, Pat,  
10 Andrea Family. You're so far but so critical to my formation. Unconditional love. Roommate

## TABLE OF CONTENTS

12	LIST OF TABLES . . . . .	vii
13	LIST OF FIGURES . . . . .	viii
14	LIST OF ABBREVIATIONS . . . . .	xiii
15	CHAPTER 1      INTRODUCTION . . . . .	1
16	CHAPTER 2      DARK MATTER IN THE COSMOS . . . . .	2
17	2.1 Introduction . . . . .	2
18	2.2 Dark Matter Basics . . . . .	3
19	2.3 Evidence for Dark Matter . . . . .	4
20	2.4 Searching for Dark Matter: Particle DM . . . . .	11
21	2.5 Sources for Indirect Dark Matter Searches . . . . .	16
22	2.6 Multi-Messenger Dark Matter . . . . .	18
23	CHAPTER 3      MULTIMESSENGER ASTROPHYSICS: DETECTING HIGH EN-	
24	ERGY NEUTRAL MESSENGERS . . . . .	21
25	3.1 Introduction . . . . .	21
26	3.2 Charged Particles in a Medium . . . . .	21
27	3.3 Photons ( $\gamma$ ) . . . . .	22
28	3.4 Neutrinos ( $\nu$ ) . . . . .	22
29	3.5 Opportunities to Combine for Dark Matter . . . . .	22
30	CHAPTER 4      HIGH ALTITUDE WATER CHERENKOV (HAWC) OBSERVATORY .	24
31	4.1 The Detector . . . . .	24
32	4.2 Events Reconstruction and Data Acquisition . . . . .	24
33	4.3 Remote Monitoring . . . . .	24
34	CHAPTER 5      ICECUBE NEUTRINO OBSERVATORY . . . . .	25
35	5.1 The Detector . . . . .	25
36	5.2 Events Reconstruction and Data Acquisition . . . . .	25
37	5.3 Northern Test Site . . . . .	25
38	CHAPTER 6      COMPUTATIONAL TECHNIQUES IN PARTICLE ASTROPHYSICS .	26
39	6.1 Neural Networks for Gamma/Hadron Separation . . . . .	26
40	6.2 Parallel Computing for Dark Matter Analyses . . . . .	26
41	CHAPTER 7      GLORY DUCK: MULTI-WAVELENGTH SEARCH FOR DARK MATT-	
42	TER ANNIHILATION TOWARDS DWARF SPHEROIDAL GALAX-	
43	IES . . . . .	27
44	7.1 Introduction . . . . .	27
45	7.2 Dataset and Background . . . . .	29
46	7.3 Analysis . . . . .	30

47	7.4	Likelihood Methods . . . . .	35
48	7.5	HAWC Results . . . . .	41
49	7.6	Glory Duck Combined Results . . . . .	44
50	7.7	HAWC Systematics . . . . .	49
51	7.8	<i>J</i> -factor distributions . . . . .	50
52	7.9	Discussion and Conclusions . . . . .	56
53	CHAPTER 8	MULTITHREADING HAWC ANALYSES FOR DARK MATTER SEARCHES . . . . .	60
54	8.1	Introduction . . . . .	60
55	8.2	Dataset and Background . . . . .	60
56	8.3	Analysis . . . . .	61
58	CHAPTER 9	HEAVY DARK MATTER ANNIHILATION SEARCH WITH ICE- CUBE'S NORTH SKY TRACK DATA . . . . .	65
59	CHAPTER 10	NU DUCK . . . . .	66
61	APPENDIX A	MULTI-EXPERIMENT SUPPLEMENTARY FIGURES . . . . .	67
62	BIBLIOGRAPHY	. . . . .	69

## LIST OF TABLES

64    Table 7.1    Summary of the relevant properties of the dSphs used in the present work. 65    Column 1 lists the dSphs. Columns 2 and 3 present their heliocentric distance 66    and galactic coordinates, respectively. Columns 4 and 5 report the $J$ -factors of 67    each source given from the $\mathcal{GS}$ and $\mathcal{B}$ independent studies and their estimated 68 $\pm 1\sigma$ uncertainties. The values $\log_{10} J$ ( $\mathcal{GS}$ set) [45] correspond to the mean 69 $J$ -factor values for a source extension truncated at the outermost observed star. 70    The values $\log_{10} J$ ( $\mathcal{B}$ set) [47] are provided for a source extension at the tidal 71    radius of each dSph. <b>Bolded sources are within HAWC's field of view and</b> 72 <b>provided to the Glory Duck analysis.</b>	. . . . .    35
73    Table 7.2    Summary of dSph observations by each experiment used in this work. A 74    ‘-’ indicates the experiment did not observe the dSph for this study. For 75    Fermi-LAT, the exposure at 1 GeV is given. For HAWC, $ \Delta\theta $ is the absolute 76    difference between the source declination and HAWC latitude. HAWC is more 77    sensitive to sources with smaller $ \Delta\theta $ . For IACTs, we show the zenith angle 78    range, the total exposure, the energy range, the angular radius $\theta$ of the signal or 79    ON region, the ratio of exposures between the background-control (OFF) and 80    signal (ON) regions ( $\tau$ ), and the significance of gamma-ray excess in standard 81    deviations, $\sigma$ .	. . . . .    36
82    Proof I know how to include	

## LIST OF FIGURES

84	Figure 2.1	Rotation curve fit to NGC 6503 from [7]. Dashed line is the contribution 85 from visible matter. Dotted curves are from gas. Dash-dot curves are from 86 dark matter (DM). Solid line is the composite contribution from all matter 87 and DM sources. Data are indicated with bold dots with error bars. Data 88 agree strongly with a matter + DM composite prediction. . . . .	5
89	Figure 2.2	Light from distant galaxy is bent in unique ways depending on the distribution 90 of mass between the galaxy and Earth. Yellow dashed lines indicate where 91 the light would have gone if the matter were not present [8]. . . . .	7
92	Figure 2.3	(left) Optical image of galactic cluster 1E0657-558. (right) X-ray image of the 93 cluster with redder meaning hotter and higher baryon density. (both) Green 94 contours are reconstruction of gravity contours from weak lensing. White 95 rings are the best fit mass maxima at 68.3%, 95.5%, and 99.7% confidence. 96 The matter maxima of the clusters are clearly separated from x-ray maxima. [9]	8
97	Figure 2.4	Plank CMB sky. Sky map features small variations in temperature in primor- 98 dial light. These anisotropies are used to make inferences about the universe's 99 energy budget and developmental history. [10] . . . . .	9
100	Figure 2.5	Observed Cosmic Microwave Background power spectrum as a function of 101 multipole moment from Plank [10]. Blue line is best fit model from $\Lambda$ CDM. 102 Red points and lines are data and error, respectively. . . . .	10
103	Figure 2.6	Predicted power spectra of CMB for different $\Omega_m h^2$ values for fixed baryon 104 density from [11]. (left) Low $\Omega_m h^2$ increases the prominence of first and 105 second peaks. (middle) $\Omega_m h^2$ is most similar to the observed power spectrum. 106 The second and third peaks are similar in height. (right) $\Omega_m h^2$ is large which 107 suppresses the first peak and raises the prominence of the third peak. . . . .	10
108	Figure 2.7	The Standard Model (SM) of particle physics. Figure taken from <a href="http://www.quantumdiaries.org/2014/03/14/the-standard-model-a-beautiful-but-flawed-theory/">http://www.quantumdiaries.org/2014/03/14/the-standard-model-a-beautiful-but-flawed-theory/</a> . . . . .	12
111	Figure 2.8	Simplified Feynman diagram demonstrating with different ways DM can 112 interact with SM particles. The 'X's refer to the DM particles whereas the 113 SM refer to fundamental particles in the SM. The large circle in the center 114 indicates the vertex of interaction and is purposely left vague. The colored 115 arrows refer to different directions of time as well as their respective labels. 116 The arrows indicate the initial and final state of the DM -SM interaction in time.	13

117	Figure 2.9 A single jet event in ATLAS detector from 2017 [16]. Jet momentum was 118 observed to be 1.9 TeV. Missing transverse momentum was observed to be 119 1.9 TeV compared to the initial transverse momentum of the event was 0. 120 Implied MET is traced by a red dashed line in event display. . . . .	14
121	Figure 2.10 More detailed pseudo-Feynman diagram of particle cascade from dark matter 122 annihilation into 2 quarks. The quarks hadronize and down to stable particles 123 like $\gamma$ or the anti-proton ( $p^-$ ). Diagram pulled from ICRC 2021 presentation 124 on DM annihilation search [17]. . . . .	15
125	Figure 2.11 Dark Matter (DM) decay spectrum for $b\bar{b}$ initial state and $\gamma$ final state. Redder 126 spectra are for larger DM masses. Bluer spectra are light DM masses. $x$ is a 127 unitless factor defined as the ratio of the mass of DM, $m_\chi$ , and the final state 128 particle energy $E_\gamma$ . Figure from [19]. . . . .	17
129	Figure 2.12 Different dark matter density profiles compared. Some models produce ex- 130 ceptionally large densities at small r [20]. . . . .	18
131	Figure 2.13 The Milky Way Galaxy in photons ( $\gamma$ ) and neutrinos ( $\nu$ ) [22]. The Galactic 132 center is at $l=0^\circ$ and is the brightest region in all panels. (top) An Optical 133 color image of the Milky Way galaxy seen from Earth. Clouds of gas and dust 134 obscure some light from stars. (2nd down) Integrated flux of $\gamma$ -rays observed 135 by the Fermi-LAT telescope [23]. (middle) Expected neutrino emission 136 that corresponds with Fermi-LAT observations. (2nd up) Expected neutrino 137 emission profile after considering detector systematics of IceCube. (bottom) 138 Observed neutrino emission from region of the galactic plane. Substantial 139 neutrino emission was detected. . . . .	19
140	Figure 2.14 Dark Matter annihilation spectra for different final state particle and standard 141 model annihilation channels [24]. Photons (red), $e^\pm$ (green), $\bar{p}$ (blue), $\nu$ (black). . . . .	20
142	Figure 3.1 TODO: Show a nuclear reactor with cherenkov radiation[NEEDS A SOURCE][FACT 143 CHECK THIS] . . . . .	22
144	Figure 3.2 TODO: absorption spectrum of liquid and solid water[NEEDS A SOURCE][FACT 145 CHECK THIS] . . . . .	23

146	Figure 7.1 Sensitivities of five gamma-ray experiments compared to percentages of the 147 Crab nebula's emission and dark matter annihilation. Solid lines present 148 estimated sensitivities to power law spectra [FACT CHECK THIS]for each 149 experiment. Green lines are Fermi-LAT sensitivities where lighter green is 150 the sensitivity to the galactic center and dark green is its sensitivity to higher 151 declinations. Orange, red, and purple solid lines represent the MAGIC, HESS, 152 and VERITAS 50 hour sensitivities respectively. The maroon and brown lines 153 are the HAWC 1 year and 5 year sensitivities. Across four decades of gamma- 154 ray energy, these experiments have similar sensitivities on the order $10^{-12}$ 155 erg cm $^{-2}$ s $^{-1}$ . The dotted lines are estimated dark matter fluxes assuming 156 $m_\chi = 5$ TeV DM annihilating to bottom quarks (red), tau leptons (blue), 157 and W bosons (green). Faded gray lines outline percentage flux of the Crab 158 nebula. Figure is an augmented version of [25] . . . . .	28
159	Figure 7.2 Effect of Electroweak (EW) corrections on expected DM annihilation spec- 160 trum for $\chi\chi \rightarrow W^-W^+$ . Solid lines are spectral models that consider EW 161 corrections. Dash-dot lines are spectral models without EW corrections. Red 162 lines are models for $M_\chi = 1$ TeV. Blue lines represent models for $M_\chi = 100$ 163 TeV. All models are sourced from the PPPC4DMID [44]. . . . .	32
164	Figure 7.3 $\frac{dJ}{d\Omega}$ maps for Segue1 (top) and Coma Berenices (bottom). Origin is centered 165 on the specific dwarf spheroidal galaxies (dSph). X and Y axes are the 166 angular separation from the center of the dwarf. Plots of the remaining 11 167 dSph HAWC studied are linked in Fig. A.1. . . . .	34
168	Figure 7.4 Illustration of the combination technique showing a comparison between 169 $-2 \ln \lambda$ provided by four instruments (colored lines) from the observation 170 of the same dSph without any $J$ nuisance and their sum, <i>i.e.</i> the resulting 171 combined likelihood (thin black line). According to the test statistics of 172 Equation (7.6), the intersection of the likelihood profiles with the line $-2 \ln \lambda$ 173 = 2.71 indicates the 95% C.L. upper limit on $\langle \sigma v \rangle$ . The combined likelihood 174 (thin black line) shows a smaller value of upper limit on $\langle \sigma v \rangle$ than those 175 derived by individual instruments. We also show how the uncertainties on 176 the $J$ factor effects the combined likelihood and degrade the upper limit on 177 $\langle \sigma v \rangle$ (thick black line). All likelihood profiles are normalized so that the global 178 minimum $\widehat{\langle \sigma v \rangle}$ is 0. We note that each profile depends on the observational 179 conditions in which a target object was observed. The sensitivity of a given 180 instrument can be degraded and the upper limits less constraining if the 181 observations are performed in non-optimal conditions such as a high zenith 182 angle or a short exposure time. . . . .	39
183	Figure 7.5 HAWC upper limits at 95% confidence level on $\langle \sigma v \rangle$ versus DM mass for 184 seven annihilation channels, using the set of $J$ -factors from Ref. [53] The 185 solid line represents the observed combined limit. Dashed lines represent 186 limits from individual dSphs. . . . .	42

187	Figure 7.6 HAWC TS values for best fit $\langle\sigma v\rangle$ versus $m_\chi$ for seven SM annihilation channels with $J$ factors from $\mathcal{GS}$ . The solid black line shows the combined best fit TS values. The colored, dashed lines are the TS values for each of the 13 sources HAWC studied.	43
191	Figure 7.7 HAWC Brazil bands at 95% confidence level on $\langle\sigma v\rangle$ versus DM mass for seven annihilation channels with $J$ -factors from $\mathcal{GS}$ [53]. The solid line represents the combined limit from 13 dSphs. The dashed line is the expected limit. The green band is the 68% containment. The yellow band is the 95% containment.	44
196	Figure 7.8 Upper limits at 95% confidence level on $\langle\sigma v\rangle$ in function of the DM mass for eight annihilation channels, using the set of $J$ factors from Ref. [53] ( $\mathcal{GS}$ set in Table 7.1). The black solid line represents the observed combined limit, the black dashed line is the median of the null hypothesis corresponding to the expected limit, while the green and yellow bands show the 68% and 95% containment bands. Combined upper limits for each individual detector are also indicated as solid, colored lines. The value of the thermal relic cross-section in function of the DM mass is given as the red dotted-dashed line [54].	45
205	Figure 7.9 Same as Fig. 7.8, using the set of $J$ factors from Ref. [47, 55] ( $\mathcal{B}$ set in Table 7.1).	46
206	Figure 7.10 Comparisons of the combined limits at 95% confidence level for each of the eight annihilation channels when using the $J$ factors from Ref. [53] ( $\mathcal{GS}$ set in Table 7.1), plain lines, and the $J$ factor from Ref. [47, 55] ( $\mathcal{B}$ set in Table 7.1), dashed lines. The cross-section given by the thermal relic is also indicated [54].	48
210	Figure 7.11 Comparisons of the combined limits at 95% confidence level for a point source analysis and extended source using [53] $\mathcal{GS}$ J-factor distributions and PPPC [44] annihilation spectra. Shown are the limits for Segue1 which will have the most significant impact on the combined limit. 6 of the 7 DM annihilation channels are shown. Solid lines are extended source studies. Dashed lines are point source studies. Overall, the extended source analysis improves the limit by a factor of 2.	50
217	Figure 7.12 Same as Fig. 7.11 on Coma Berenices. This dSph also contributes significantly to the limit. The limits are identical in this case.	51
219	Figure 7.13 Comparison of combined limits when correcting for HAWC's pointing systematic. All DM annihilation channels are shown. The solid black line is the ratio between published limit to the declination corrected limit. The blue solid line or "Combined_og" represented the limits computed for Glory Duck. The solid orange line or "Combined_ad" represented the limits computed after correcting for the pointing systematic.	52

225	Figure 7.14 Differential map of $dJ/\Omega$ from model built in Section 7.8.1 and profiles 226 provided directly from authors. (Top) Differential from Segue1. (bottom) 227 Differential from Coma Berenices. Note that their scales are not the same. 228 Segue1 shows the deepest discrepancies which is congruent with its large 229 uncertainties. Both models show anuli where unique models become apparent. . . . .	53
230	Figure 7.15 HAWC limits for Coma Berenices (top) and Segue1 (bottom) for two different 231 map sets. Blue lines are limits calculated on maps with poor model repre- 232 sentation. Orange lines are limits calculated on spatial profiles provided by 233 the authors of [45]. Black line is the ratio of the poor spatial model limits to 234 the corrected spatial models. The left y-axis measures $\langle\sigma v\rangle$ for the blue and 235 orange lines. The right y-axis measures the ratio and is unitless. . . . .	54
236	Figure 7.16 Comparisons between the $J$ -factors versus the angular radius for the com- 237 putation of $J$ factors from Ref. [53] ( $\mathcal{GS}$ set in Table 7.1) in blue and for 238 the computation from Ref. [47, 55] ( $\mathcal{B}$ set in Tab. 7.1) in orange. The solid 239 lines represent the central value of the $J$ -factors while the shaded regions 240 correspond to the $1\sigma$ standard deviation. . . . .	57
241	Figure 7.17 Comparisons between the $J$ -factors versus the angular radius for the computa- 242 tion of $J$ factors from Ref. [53] ( $\mathcal{GS}$ set in Tab. 7.1) in blue and for the 243 computation from Ref. [47, 55] ( $\mathcal{B}$ set in Tab. 7.1) in orange. The solid 244 lines represent the central value of the $J$ -factors while the shaded regions 245 correspond to the $1\sigma$ standard deviation. . . . .	58
246	Figure 8.1 Difference between spectral hypotheses from PPPC [44] and HDM [64]. 247 Shown is the expected DM annihilation spectrum for $\chi\chi \rightarrow W^-W^+$ . Solid 248 lines are spectral models with EW corrections from the PPPC. Dash-dot lines 249 are spectral models from HDM. Red lines are models for $M_\chi = 1$ TeV. Blue 250 lines represent models for $M_\chi = 100$ TeV. . . . .	63
251	Figure 8.2 This is a caption . . . . .	64
252	Figure A.1 Sister figure to Figure 7.3. Sources in the first row from left to right: Bootes 253 I, Canes Venatici I, II. In second row: Draco, Hercules, Leo I. In the first row: 254 Leo II, Leo IV, Sextans. In the final row: Ursa Major I, Ursa Major II. . . . .	68

**LIST OF ABBREVIATIONS**

- 256 **MSU** Michigan State University  
257 **LANL** Los Alamos National Laboratory  
258 **DM** Dark Matter  
259 **SM** Standard Model  
260 **HAWC** High Altitude Water Cherenkov Observatory

261

## **CHAPTER 1**

### **INTRODUCTION**

262 Is the text not rendering right? Ah ok it knows im basically drafting the doc still

## CHAPTER 2

263

### DARK MATTER IN THE COSMOS

264 **2.1 Introduction**

265 The dark matter problem can be summarized in part by the following thought experiment.

266 Let us say you are the teacher for an elementary school classroom. You take them on a field  
267 trip to your local science museum and among the exhibits is one for mass and weight. The exhibit  
268 has a gigantic scale, and you come up with a fun problem for your class.

269 You ask your class, "What is the total weight of the classroom? Give your best estimation to  
270 me in 30 minutes, and then we'll check your guess on the scale. If your guess is within 10% of the  
271 right answer, we will stop for ice cream on the way back."

272 The students are ecstatic to hear this, and they get to work. The solution is some variation of  
273 the following strategy. The students should give each other their weight or best guess if they do  
274 not know. Then, all they must do is add each student's weight and get a grand total for the class.  
275 The measurement on the giant scale should show the true weight of the class. When comparing  
276 the measured weight to your estimation, multiply the measurement by  $1.0 \pm 0.1$  to get the  $\pm 10\%$   
277 tolerances for your estimation.

278 Two of your students, Sandra and Mario, return to you with a solution.

279 They say, "We weren't sure of everyone's weight. We used 65 lbs. for the people we didn't  
280 know and added everyone who does know. There are 30 of us, and we got 2,000 lbs.! That's a ton!"

281 You estimated 1,900 lbs. assuming the average weight of a student in your class was 60 lbs.  
282 So, you are pleased with Sandra's and Mario's answer. You instruct your students to all gather on  
283 the giant scale and read off the weight together. To all your surprise, the scale reads *10,000 lbs.*!  
284 10,000 is significantly more than a 10% error from 2,000. In fact, it is approximately 5 times more  
285 massive than either your or your students' estimates. You think to yourself and conclude there  
286 must be something wrong with the scale. You ask an employee to check the scale and verify it is  
287 well calibrated. They confirm that the scale is in working order. You weigh a couple of students  
288 individually to assess that the scale is well calibrated. Sandra weighs 59 lbs., and Mario weighs

289 62 lbs., typical weights for their age. You then weigh each student individually and see that their  
290 weights individually do not deviate greatly from 60 lbs. So, where does all the extra weight come  
291 from?

292 This thought experiment serves as an analogy to the Dark Matter problem. The important  
293 substitution to make however is to replace the students with stars and the classroom with a galaxy,  
294 say the Milky Way. Individually the mass of stars is well measured and defined with the Sun as our  
295 nearest test case. However, when we set out to measure the mass of a collection of stars as large as  
296 galaxies, our well-motivated estimation is wildly incorrect. There simply is no way to account for  
297 this discrepancy except without some unseen, or dark, contribution to mass and matter in galaxies.  
298 I set out in my thesis to narrow the possibilities of what this Dark Matter could be.

299 This chapter is organized like the following... **TODO: Text should look like ... Chapter x has**  
300 **blah blah blah.**

301 **2.2 Dark Matter Basics**

302 Presently, a more compelling theory of cosmology that includes Dark Matter (DM) in order  
303 to explain a variety of observations is  $\Lambda$  Cold Dark Matter, or  $\Lambda$ CDM. I present the evidence  
304 supporting  $\Lambda$ CDM in Section 2.3 yet discuss the conclusions of the  $\Lambda$ CDM model here. According  
305 to  $\Lambda$ CDM fit to observations on the Cosmic Microwave Background (CMB), DM is 26.8% of the  
306 universe's current energy budget. Baryonic matter, stuff like atoms, gas, and stars, contributes to  
307 4.9% of the universe's current energy budget [1, 2, 3].

308 DM is dark; it does not interact readily with light at any wavelength. DM also does not interact  
309 noticeably with the other standard model forces (Strong and Weak) at a rate that is readily observed  
310 [3]. DM is cold, which is to say that the average velocity of DM is below relativistic speeds [1].  
311 'Hot' DM would not likely manifest the dense structures we observe like galaxies, and instead  
312 would produce much more diffuse galaxies than what is observed [3, 1]. DM is old; it played a  
313 critical role in the formation of the universe and the structures within it [1, 2].

314 Observations of DM have so far been only gravitational. The parameter space available to what  
315 DM could be therefore is extremely broad. The broad DM parameter space is iteratively tested in

316 DM searches by supposing a hypothesis that has not yet been ruled out and performing observations  
317 to test them. When the observations yield a null result, the parameter space is constrained further.  
318 I present some approaches for DM searches in Section 2.4.

319 **2.3 Evidence for Dark Matter**

320 Dark Matter (DM) has been a looming problem in physics for almost 100 years. Anomalies  
321 have been observed by astrophysicists in galactic dynamics as early as 1933 when Fritz Zwicky  
322 noticed unusually large velocity dispersion in the Coma cluster. Zwicky's measurement was the  
323 first recorded to use the Virial theorem to measure the mass fraction of visible and invisible matter  
324 in celestial bodies [4]. From Zwicky in [5], "*If this would be confirmed, we would get the surprising*  
325 *result that dark matter is present in much greater amount than luminous matter.*" Zwicky's and  
326 others' observation did not instigate a crisis in astrophysics because the measurements did not  
327 entirely conflict with their understanding of galaxies [4]. In 1978, Rubin, Ford, and Norbert  
328 measured rotation curves for ten spiral galaxies [6]. Rubin et al.'s 1978 publication presented a  
329 major challenge to the conventional understanding of galaxies that could no longer be dismissed by  
330 measurement uncertainties. Evidence has been mounting ever since for this exotic form of matter.  
331 The following subsections provide three compelling pieces of evidence in support of the existence  
332 of DM.

333 **2.3.1 First Clues: Stellar Velocities**

334 Zwicky, and later Rubin, measured the stellar velocities of various galaxies to estimate their  
335 virial mass. The Virial Theorem upon which these observations are interpreted is written as

$$2T + V = 0. \quad (2.1)$$

336 Where  $T$  is the kinetic energy and  $V$  is the potential energy in a self-gravitating system. The  
337 classical Newton's law of gravity from stars and gas was used for gravitational potential modeled in  
338 the observed galaxies:

$$V = -\frac{1}{2} \sum_i \sum_{j \neq i} \frac{m_i m_j}{r_{ij}}. \quad (2.2)$$

339 Zwicky et al. measured just the velocities of stars apparent in optical wavelengths [5]. Rubin et al.  
 340 added by measuring the velocity of the hydrogen gas via the 21 cm emission line of Hydrogen [6].  
 341 The velocities of the stars and gas are used to infer the total mass of galaxies and galaxy clusters  
 342 via Equation (2.1). An inferred mass is obtained from the luminosity of the selected sources. The  
 343 two inferences are compared to each other as a luminosity to mass ratio which typically yielded [1]

$$\frac{M}{L} \sim 400 \frac{M_{\odot}}{L_{\odot}} \quad (2.3)$$

344  $M_{\odot}$  and  $L_{\odot}$  referring to stellar mass and stellar luminosity, respectively. These ratios clearly indicate  
 345 a discrepancy in apparent light and mass from stars and gas and their velocities.

346 Rubin et al. [6] demonstrated that the discrepancy was unlikely to be an underestimation of  
 347 the mass of the stars and gas. The inferred "dark" mass was up to 5 times more than the luminous  
 348 mass. This dark mass also needed to extend well beyond the extent of the luminous matter.

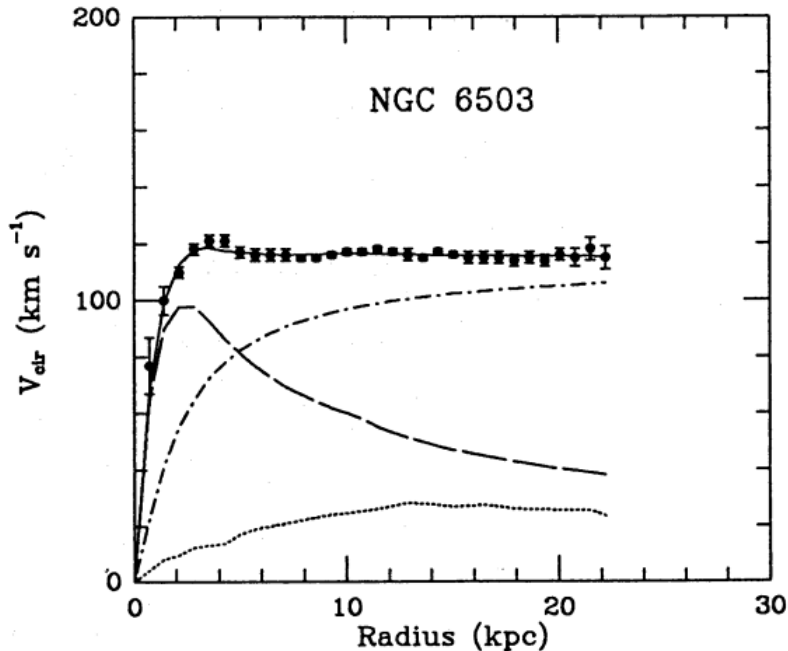


Figure 2.1 Rotation curve fit to NGC 6503 from [7]. Dashed line is the contribution from visible matter. Dotted curves are from gas. Dash-dot curves are from dark matter (DM). Solid line is the composite contribution from all matter and DM sources. Data are indicated with bold dots with error bars. Data agree strongly with a matter + DM composite prediction.

349 Figure 2.1 features one of many rotation curves plotted from the stellar velocities within galaxies.

350 The measured rotation curves mostly feature a flattening of velocities at higher radius which is not  
351 expected if the gravity was only coming from gas and luminous matter. The extension of the  
352 flat velocity region also indicates that the DM is distributed far from the center of the galaxy.  
353 Modern velocity measurements include significantly larger objects, galactic clusters, and smaller  
354 objects, dwarf galaxies. Yet, measurements along this regime are leveraging the Virial theorem  
355 with Newtonian potential energies. We know Newtonian gravity is not a comprehensive description  
356 of gravity. New observational techniques have been developed since 1978, and those are discussed  
357 in the following sections.

358 **2.3.2 Evidence for Dark Matter: Gravitational Lensing**

359 Modern evidence for dark matter comes from new avenues beyond stellar velocities. Grav-  
360 itational lensing from DM is a new channel from general relativity. General relativity predicts  
361 aberrations in light caused by massive objects. In recent decades we have been able to measure the  
362 lensing effects from compact objects and DM halos. Figure 2.2 shows how different massive ob-  
363 jects change the final image of a faraway galaxy resulting from gravitational lensing. Gravitational  
364 lensing developed our understanding of dark matter in two important ways.

365 Gravitational lensing provides additional compelling evidence for DM. The observation of two  
366 merging galactic clusters in 2006, shown in Figure 2.3, provided a compelling argument for DM  
367 outside the Standard Model. These clusters merged recently in astrophysical time scales. Galaxies  
368 and star cluster have mostly passed by each other as the likelihood of their collision is low. Therefore,  
369 these massive objects will mostly track the highest mass, dark and/or baryonic, density. Yet, the  
370 intergalactic gas is responsible for the majority of the baryonic mass in the systems [4]. These gas  
371 bodies will not phase through and will heat up as they collide together. The hot gas is located via  
372 x-ray emission from the cluster. Two observations of the clusters were performed independently of  
373 each other.

374 The first was the lensing of light around the galaxies due to their gravitational influences.  
375 When celestial bodies are large enough, the gravity they exert bends space and time itself. The  
376 warped space-time lenses light and will deflect in an analogous way to how glass lenses will bend

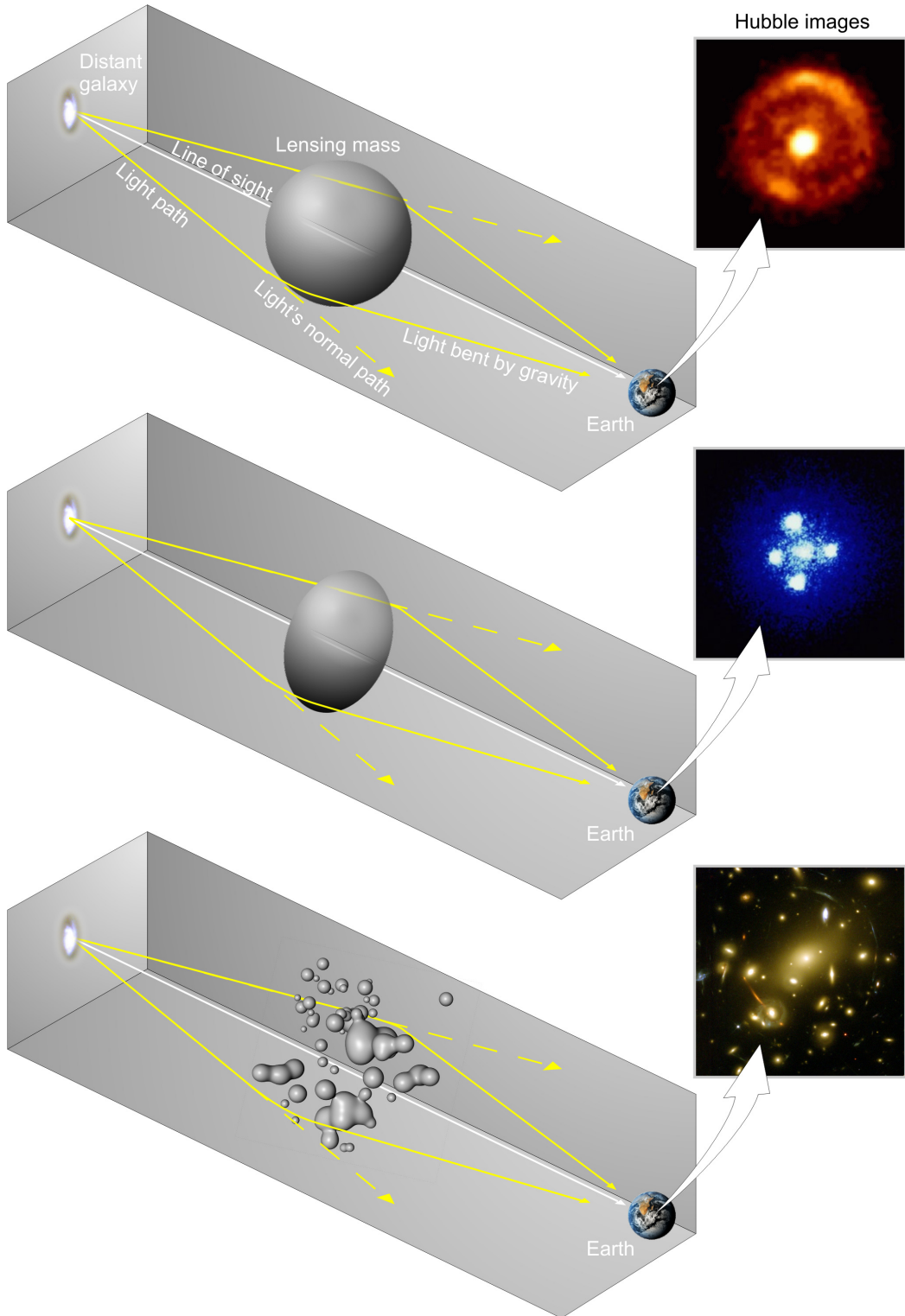


Figure 2.2 Light from distant galaxy is bent in unique ways depending on the distribution of mass between the galaxy and Earth. Yellow dashed lines indicate where the light would have gone if the matter were not present [8].

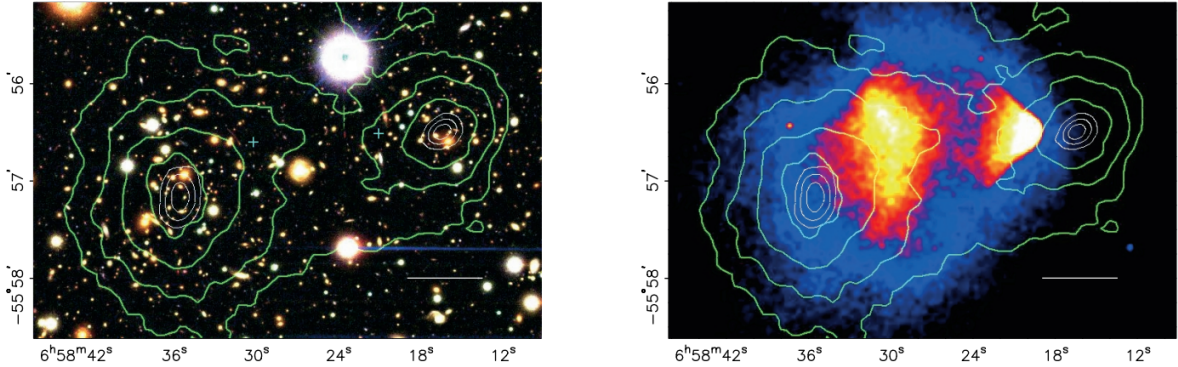


Figure 2.3 (left) Optical image of galactic cluster 1E0657-558. (right) X-ray image of the cluster with redder meaning hotter and higher baryon density. (both) Green contours are reconstruction of gravity contours from weak lensing. White rings are the best fit mass maxima at 68.3%, 95.5%, and 99.7% confidence. The matter maxima of the clusters are clearly separated from x-ray maxima. [9]

377 light, see Figure 2.2. With a sufficient understanding of light sources behind a massive object, we  
 378 can reconstruct the contours of the gravitational lenses. The gradient of the contours shown in  
 379 Figure 2.3 then indicates how dense the matter is and where it is.

380 The x-ray emission can then be observed from the clusters. Since these galaxies are mostly gas  
 381 and are merging, then the gas should be getting hotter. If they are merging, the x-ray emissions  
 382 should be the strongest where the gas is mostly moving through each other. Hence, X-ray emission  
 383 maps out where the gas is in the merging galaxy cluster.

384 The lensing and x-ray observations were done on the Bullet cluster featured on Figure 2.3.  
 385 The x-ray emissions do not align with the gravitational contours from lensing. The incongruence  
 386 in mass density and baryon density suggests that there is a lot of matter somewhere that does  
 387 not interact with light. Moreover, this dark matter cannot be baryonic [9]. The Bullet Cluster  
 388 measurement did not really tell us what DM is exactly, but it did give the clue that DM also does  
 389 not interact with itself very strongly. If DM did interact strongly with itself, then it would have been  
 390 more aligned with the x-ray emission [9]. There have been follow-up studies of galaxy clusters with  
 391 similar results. The Bullet Cluster and others like it provide a persuasive case against something  
 392 possibly amiss in our gravitational theories.

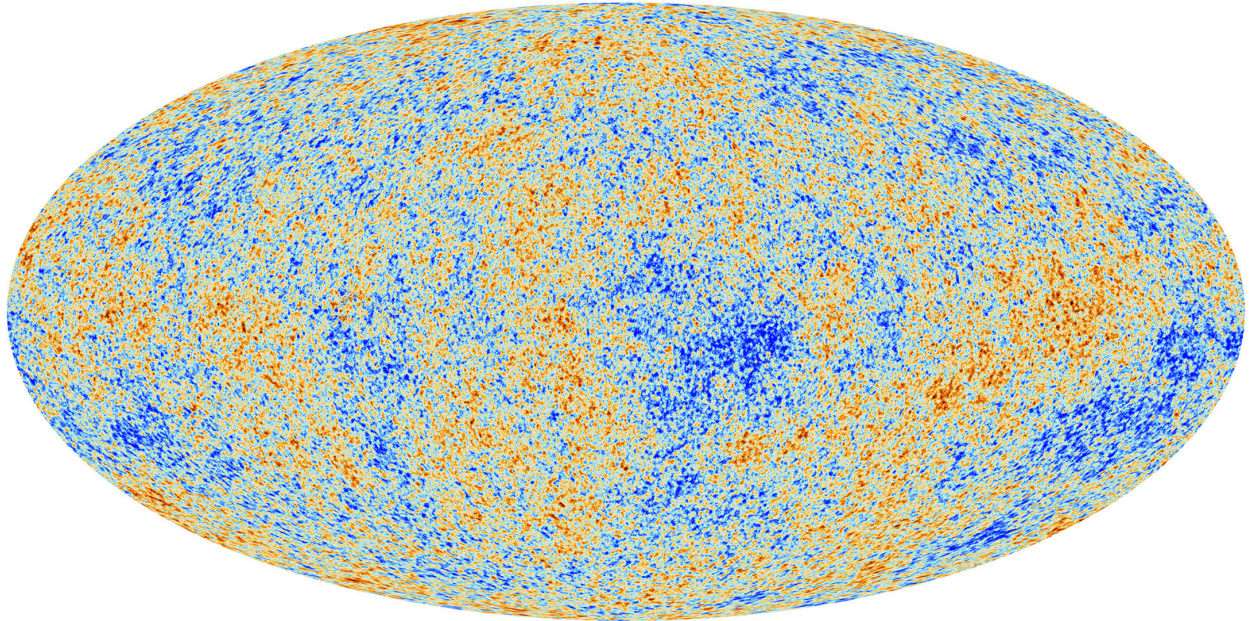


Figure 2.4 Plank CMB sky. Sky map features small variations in temperature in primordial light. These anisotropies are used to make inferences about the universe's energy budget and developmental history. [10]

393 **2.3.3 Evidence for Dark Matter: Cosmic Microwave Background**

394 The Cosmic Microwave Background (CMB) is the primordial light from the early universe  
395 when Hydrogen atoms formed from the free electron and proton soup in the early universe. The  
396 CMB is the earliest light we can observe; released when the universe was about 380,000 years old.  
397 Then we look at how the simulated universes look like compared to what we see. Figure 2.4 is the  
398 most recent CMB image from the Plank satellite after subtracting the average value and masking the  
399 galactic plane [10]. Redder regions indicate a slightly hotter region in the CMB, and blue indicates  
400 colder. The intensity variations are on the order of 1 in 1000 with respect to the average value.

401 The Cosmic Microwave Background shows that the universe had DM in it from an incredibly  
402 early stage. To measure the DM, Dark Energy, and matter fractions of the universe from the CMB,  
403 the image is analyzed into a power spectrum, which shows the amplitude of the fluctuations as  
404 a function of spherical multipole moments.  $\Lambda$ CDM provides the best fit to the power spectra of  
405 the CMB as shown in Figure 2.5. The CMB power spectrum is quite sensitive to the fraction  
406 of each energy contribution in the early universe. Low  $l$  modes are dominated by variations  
407 in gravitational potential. Intermediate  $l$  emerge from oscillations in photon-baryon fluid from

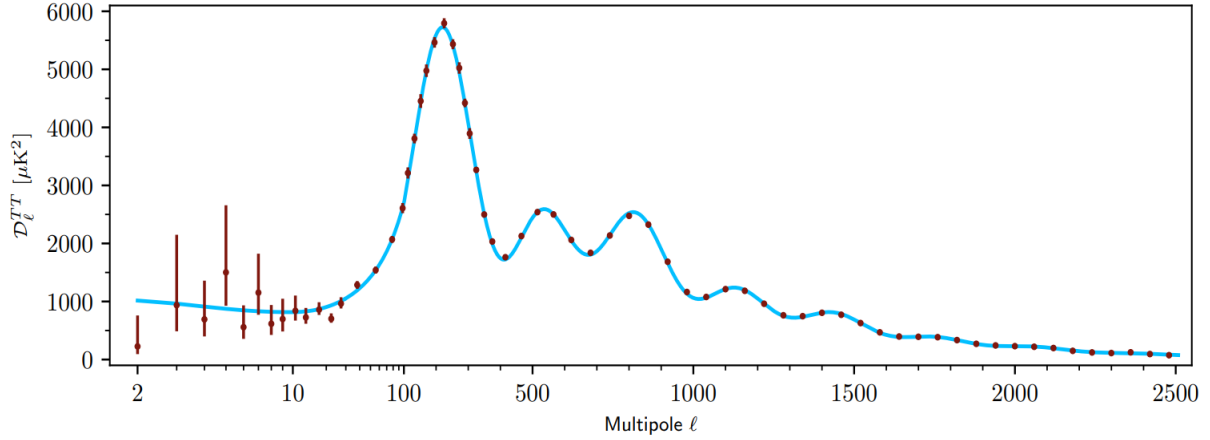


Figure 2.5 Observed Cosmic Microwave Background power spectrum as a function of multipole moment from Plank [10]. Blue line is best fit model from  $\Lambda$ CDM. Red points and lines are data and error, respectively.

408 competing baryon pressures and gravity. High  $l$  is a damped region from the diffusion of photons  
 409 during electron-proton recombination. [1]

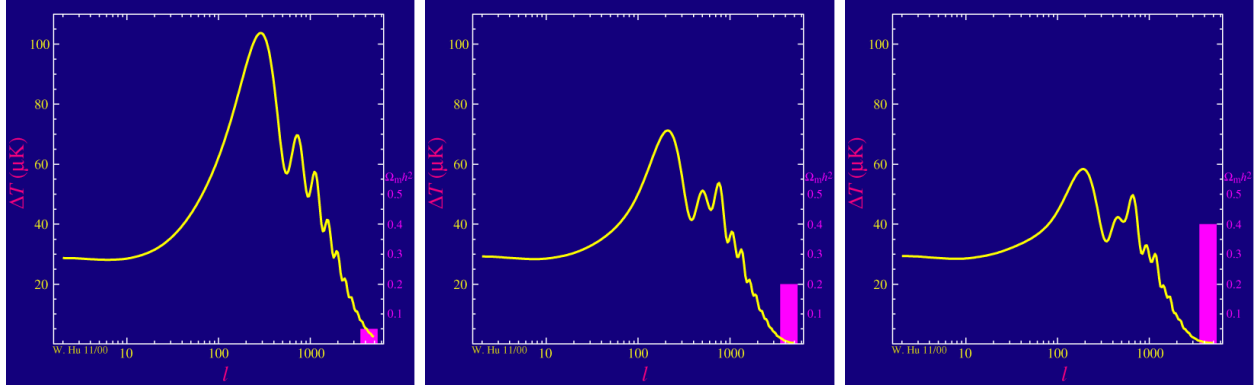


Figure 2.6 Predicted power spectra of CMB for different  $\Omega_m h^2$  values for fixed baryon density from [11]. (left) Low  $\Omega_m h^2$  increases the prominence of first and second peaks. (middle)  $\Omega_m h^2$  is most similar to the observed power spectrum. The second and third peaks are similar in height. (right)  $\Omega_m h^2$  is large which suppresses the first peak and raises the prominence of the third peak.

410 The harmonics would look quite different for a universe with less DM. Figure 2.6 demonstrates  
 411 the effect  $\Omega_m h^2$  has on the expected power spectrum for fixed baryon matter density. [11] Sweeping  
 412  $\Omega_m h^2$  in this way clearly shows the effect dark matter has on the CMB power spectrum. The  
 413 observations fit well with the  $\Lambda$ CDM model, and the derived fractions are as follows. The matter  
 414 fraction:  $\Omega_m = 0.3153$ ; and the baryon fraction:  $\Omega_b = 0.04936$  [10]. Plank's observations also  
 415 provide a measure of the Hubble constant,  $H_0$ .  $H_0$  especially has seen a growing tension in the

416 past decade that continues to deepened with observations from instruments like the James Webb  
417 Telescope [12, 13]. As Hubble tensions deepen, we may find that perhaps  $\Lambda$ **CDM**, despite its  
418 successes, is missing some critical physics.

419 Overall, the Newtonian motion of stars in galaxies, weak lensing from galactic clusters, and  
420 power spectra from primordial light form a compelling body of research in favor of dark matter.  
421 It takes another leap of theory and experimentation to make observations of DM that are non-  
422 gravitational in nature. In Section 2.3, the evidence for DM implies strongly that the DM is matter  
423 and not a lost parameter in the gravitational fields between massive objects. Finally, if we take one  
424 axiom: that this matter has quantum behavior, such as being described by some Bohr wavelength  
425 and abiding by some fermion or boson statistics; then we arrive at particle dark matter. One particle  
426 DM hypothesis is the Weakly Interacting Massive Particle (WIMP). This DM candidate theory is  
427 discussed further in the next section and is the focus of this thesis.

428 **2.4 Searching for Dark Matter: Particle DM**

429 Section 2.4 shows the Standard Model of particle physics and is currently the most accurate  
430 model for the dynamics of fundamental particles like electrons and photons. The current status  
431 of the SM does not have a viable DM candidate. When looking at the standard model, we can  
432 immediately exclude any charged particle because charged particles interact strongly with light.  
433 Specifically, this will rule out the following charged, fundamental particles:  $e, \mu, \tau, W, u, d, s, c, t, b$   
434 and their corresponding antiparticles. Recalling from Section 2.2 that DM must be long-lived and  
435 stable over the age of the universe which excludes all SM particles with decay half-lives at or shorter  
436 than the age of the universe. The lifetime constraint additionally eliminates the  $Z$  and  $H$  bosons.  
437 Finally, the candidate DM needs to be somewhat massive. Recall from Section 2.2 that DM is cold  
438 or not relativistic through the universe. This eliminates the remaining SM particles:  $\nu_{e,\mu,\tau}, g, \gamma$  as  
439 DM candidates. Because there are no DM candidates within the SM, the DM problem strongly  
440 hints to physics beyond the SM (BSM).

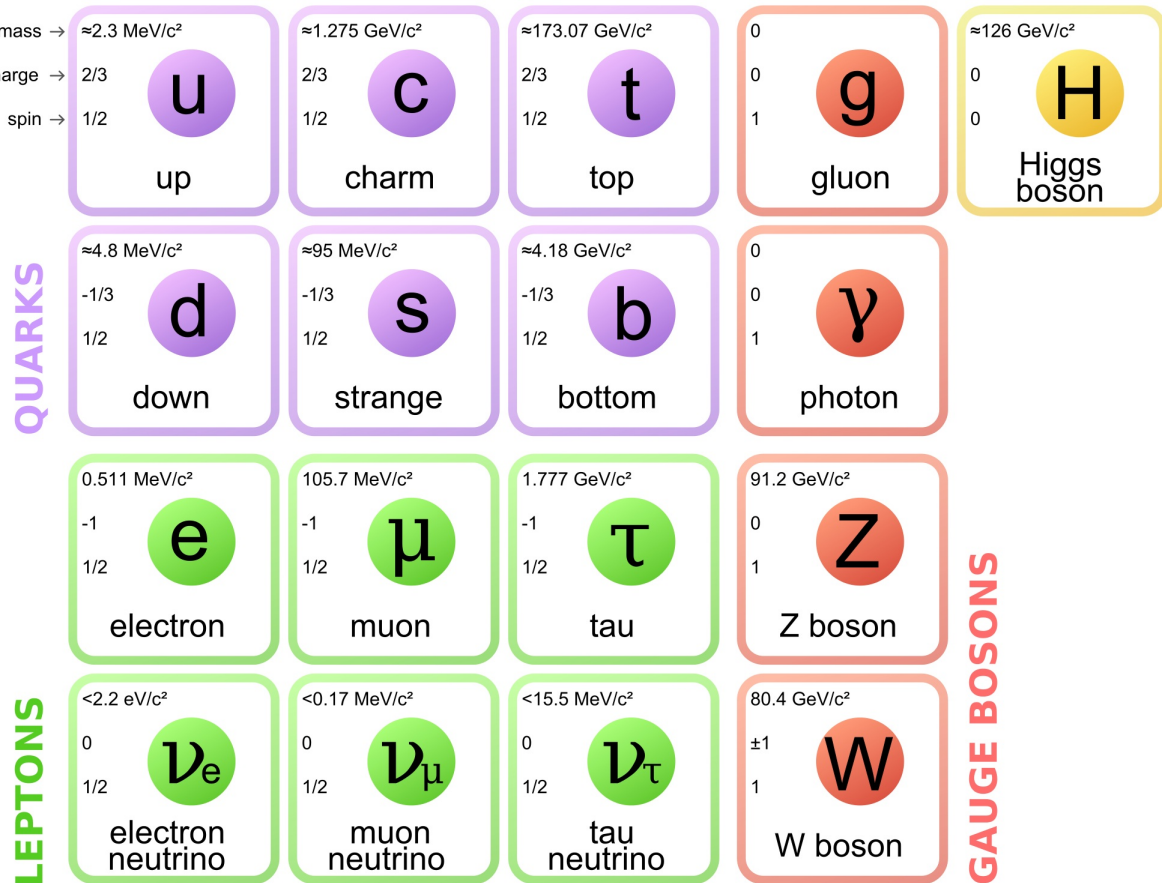


Figure 2.7 The Standard Model (SM) of particle physics. Figure taken from <http://www.quantumdiaries.org/2014/03/14/the-standard-model-a-beautiful-but-flawed-theory/>

#### 441 2.4.1 Shake it, Break it, Make it

442 When considering DM that couples in some way with the SM, the interactions are roughly  
 443 demonstrated by interaction demonstrated in Figure 2.8. The figure is a simplified Feynman  
 444 diagram where the arrow of time represents the interaction modes of: **Shake it, Break it, Make it**.

445 **Shake it** refers to the direct detection of dark matter. Direct detection interactions start with  
 446 a free DM particle and an SM particle. The DM and SM interact via elastic or inelastic collision  
 447 and recoil away from each other. The DM remains in the dark sector and imparts some momentum  
 448 onto the SM particle. The hope is that the momentum imparted onto the SM particle is sufficiently  
 449 high enough to pick up with extremely sensitive instruments. Because we cannot create the DM in  
 450 the lab, a direct detection experiment must wait until DM is incident on the detector. Most direct  
 451 detection experiments are therefore placed in low-background environments with inert detection

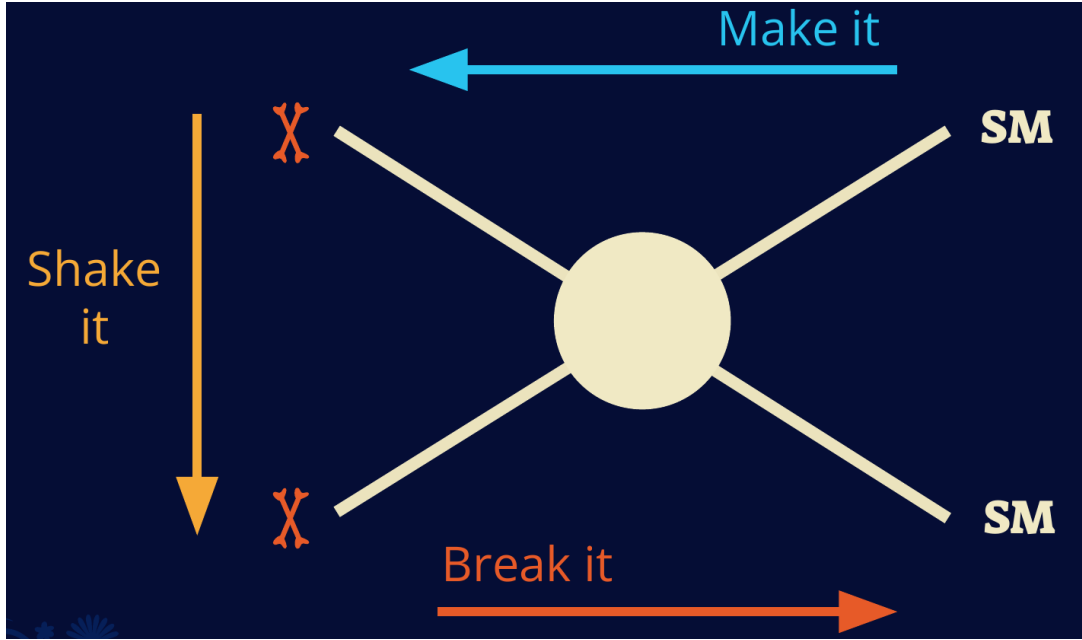


Figure 2.8 Simplified Feynman diagram demonstrating different ways DM can interact with SM particles. The 'X's refer to the DM particles whereas the SM refer to fundamental particles in the SM. The large circle in the center indicates the vertex of interaction and is purposely left vague. The colored arrows refer to different directions of time as well as their respective labels. The arrows indicate the initial and final state of the DM -SM interaction in time.

452 media like the noble gas Xenon. [14]

453 **Make it** refers to the production of DM from SM initial states. The experiment starts with  
 454 particles in the SM. These SM particles are accelerated to incredibly high energies and then collide  
 455 with each other. In the confluence of energy, DM hopefully emerges as a byproduct of the SM  
 456 annihilation. Often it is the collider experiments that are energetic enough to hypothetically produce  
 457 DM. These experiments include the world-wide collaborations ATLAS and CMS at CERN where  
 458 proton collide together at extreme energies. The DM searches, however, are complex. DM likely  
 459 does not interact with the detectors and lives long enough to escape the detection apparatus of  
 460 CERN's colliders. This means any DM production experiment searches for an excess of events  
 461 with missing momentum or energy in the events. An example event with missing transverse  
 462 momentum is shown in Figure 2.9. The missing momentum with no particle tracks implies a  
 463 neutral particle carried the energy out of the detector. However, there are other neutral particles  
 464 in the SM, like neutrons or neutrinos, so any analysis has to account for SM signatures of missing

465 momentum. [15]

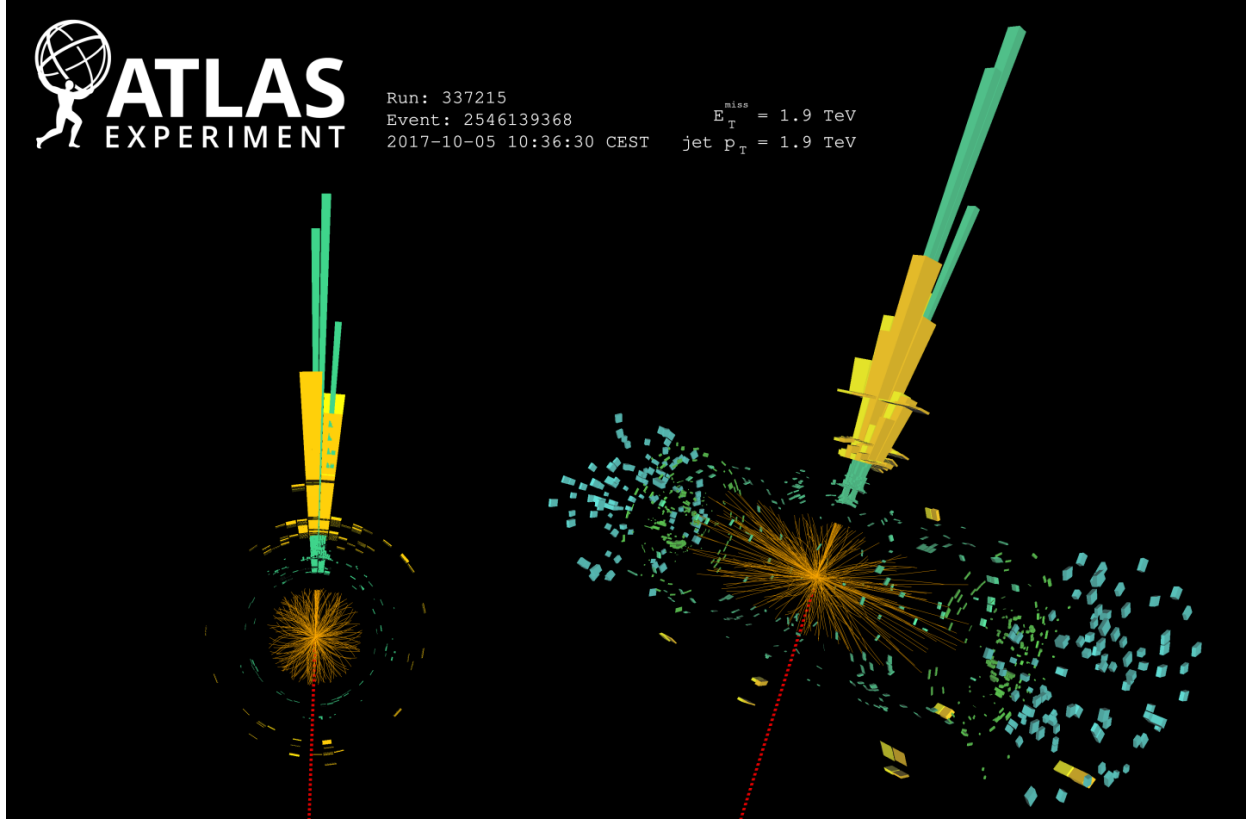


Figure 2.9 A single jet event in ATLAS detector from 2017 [16]. Jet momentum was observed to be 1.9 TeV. Missing transverse momentum was observed to be 1.9 TeV compared to the initial transverse momentum of the event was 0. Implied MET is traced by a red dashed line in event display.

#### 466 2.4.2 Break it: Standard Model Signatures of Dark Matter through Indirect Searches

467 **Break it** refers to the creation of SM particles from the dark sector, and it is the primary focus  
468 of this thesis. The interaction begins with DM or in the dark sector. The hypothesis is that this  
469 DM will either annihilate with itself or decay and produce an SM byproduct. This method is  
470 often referred to as the Indirect Detection of DM because we have no lab to directly control or  
471 manipulate the DM. Therefore, most indirect DM searches are performed using observations of  
472 known DM densities among the astrophysical sources. The strength is that we have the whole of the  
473 universe and its 13.6-billion-year lifespan to use as a detector and particle accelerator. Additionally,  
474 locations of dark matter are well cataloged since it was astrophysical observations that presented

475 the problem of DM in the first place.

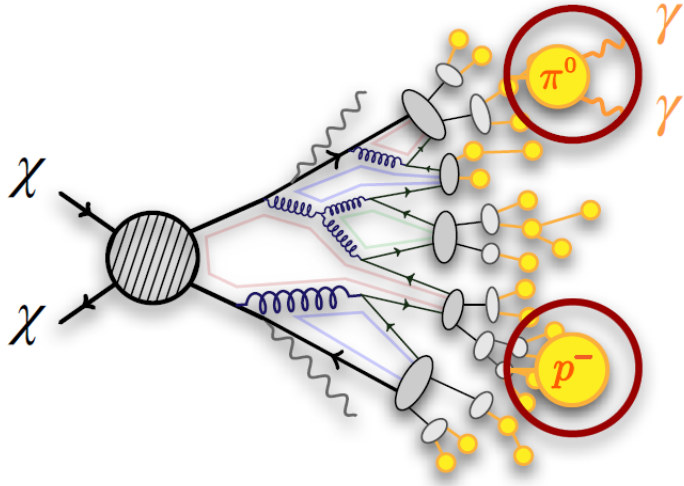


Figure 2.10 More detailed pseudo-Feynman diagram of particle cascade from dark matter annihilation into 2 quarks. The quarks hadronize and down to stable particles like  $\gamma$  or the anti-proton ( $p^-$ ). Diagram pulled from ICRC 2021 presentation on DM annihilation search [17].

476 However, anything can happen in the universe. There are many difficult to deconvolve back-  
477 grounds when searching for DM. One prominent example is the galactic center. We know the  
478 galactic center has a large DM content because of stellar kinematics in our Milky Way and DM halo  
479 simulations. Yet, any signal from the galactic center is challenging to parse apart from the extreme  
480 environment of our supermassive black hole, unresolved sources, and diffuse emission from the  
481 interstellar medium [18]. Despite the challenges, any DM model that yields evidence in the other  
482 two observation methods, **Shake it or Make it** must be corroborated with indirect observations of  
483 the known DM sources. Without corroborating evidence, DM observation in the lab is hard-pressed  
484 to demonstrate that it is the model contributing to the DM seen at the universal scale.

485 In the case of WIMP DM, signals are described in terms of primary SM particles produced  
486 from DM decay or annihilation. The SM initial state particles are then simulated down to stable  
487 final states such as the  $\gamma$ ,  $\nu$ ,  $p$ , or  $e$  which can traverse galactic lengths to reach Earth.

488 Figure 2.10 shows the quagmire of SM particles that emerges from SM initial states that are not  
489 stable [17]. There are many SM particles with varying energies that can be produced in such an

490 interaction. For any arbitrary DM source and stable SM particle, the SM flux from DM annihilating  
 491 to a neutral particle in the SM,  $\phi$ , from a region in the sky is described by the following.

$$\frac{d\Phi_\phi}{dE_\phi} = \frac{\langle\sigma v\rangle}{8\pi m_\chi^2} \frac{dN_\phi}{dE_\phi} \times \int_{\text{source}} d\Omega \int_{l.o.s} \rho_\chi^2 dl(r, \theta') \quad (2.4)$$

492 In Equation (7.1),  $\langle\sigma v\rangle$  is the velocity-weighted annihilation cross-section of DM to the SM.  $m_\chi$   
 493 refers to the mass of DM, noted with Greek letter  $\chi$ .  $\frac{dN_\phi}{dE_\phi}$  is the N particle flux weighted by the  
 494 particle energy. An example is provided in Figure 2.11 for the  $\gamma$  final state. The integrated terms  
 495 are performed over the solid angle,  $d\Omega$ , and line of sight, l.o.s.  $\rho$  is the density of DM for a  
 496 location  $(r, \theta')$  in the sky. The terms left of the ' $\times$ ' are often referred to as the particle physics  
 497 component. The terms on the right are referred to as the astrophysical component. For decaying  
 498 DM, the equation changes to...

$$\frac{d\Phi_\phi}{dE_\phi} = \frac{1}{4\pi\tau m_\chi} \frac{dN_\phi}{dE_\phi} \times \int_{\text{source}} d\Omega \int_{l.o.s} \rho_\chi dl(r, \theta') \quad (2.5)$$

499 In Equation (8.1),  $\tau$  is the decay lifetime of the DM. Just as in Equation (7.1), the left and right  
 500 terms are the particle physics and the astrophysical components respectively. The integrated  
 501 astrophysical component of Equation (7.1) is often called the J-Factor. Whereas the integrated  
 502 astrophysical component of Equation (8.1) is often called the D-Factor.

503     Exact DM  $\text{DM} \rightarrow \text{SM SM}$  branching ratios are not known, so it is usually assumed to go 100%  
 504 into an SM particle/anti-particle. Additionally, when a DM annihilation or decay produces one of  
 505 the neutral, long-lived SM particles ( $\nu$  or  $\gamma$ ), the particle is traced back to a DM source. For DM  
 506 above GeV energies, there are very few SM processes that can produce particles with such a high  
 507 energy. Seeing such a signal would almost certainly be an indication of the presence of dark matter.  
 508 Fortunately, the universe provides us with the largest volume and lifetime ever for a particle physics  
 509 experiment.

## 510 2.5 Sources for Indirect Dark Matter Searches

511     The first detection of DM relied on optical observations. Since then, we have developed new  
 512 techniques to find DM dense regions. As described in Section 2.3.1, many DM dense regions were  
 513 through observing galactic rotation curves. Our Milky Way galaxy is among DM dense regions

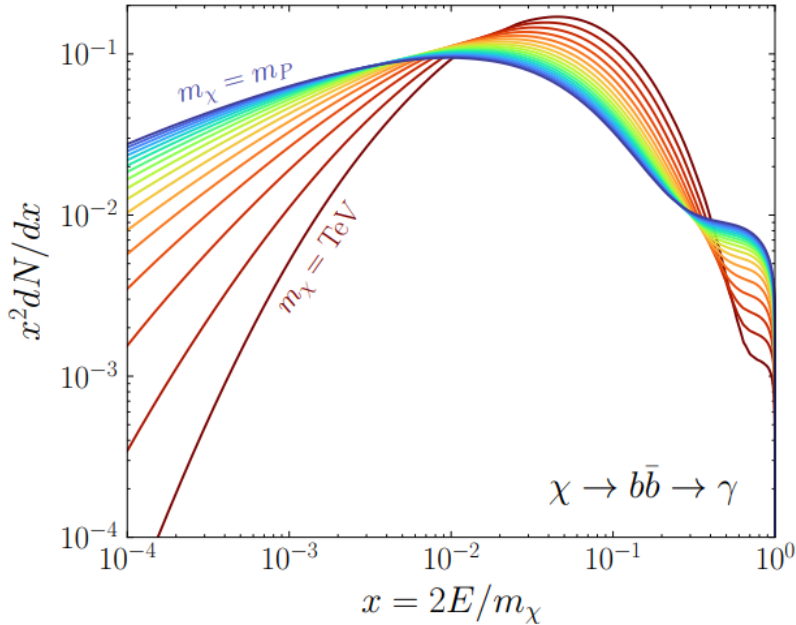


Figure 2.11 Dark Matter (DM) decay spectrum for  $b\bar{b}$  initial state and  $\gamma$  final state. Redder spectra are for larger DM masses. Bluer spectra are light DM masses.  $x$  is a unitless factor defined as the ratio of the mass of DM,  $m_\chi$ , and the final state particle energy  $E_\gamma$ . Figure from [19].

discovered, and it is the largest nearby DM dense region to look at. Additionally, the DM halo surrounding the Milky Way is clumpy [18]. There are regions in the DM halo of the Milky Way that have more DM than others that have captured gas over time. These sub-halos were dense enough collapse gas and form stars. These apparent sub galaxies are known as dwarf spheroidal galaxies and are the main sources studied in this thesis. Each source type comes with different trade-offs. Galactic Center studies will be very sensitive to the assumed distribution of DM. The central DM density can vary substantially as demonstrated in Figure 2.12. At distances close to the center of the galaxy, or small  $r$ , the differences in DM densities can be 3-4 orders of magnitude. Searches toward the galactic center will therefore be quite sensitive to the assumed DM distribution.

Searches toward Dwarf Spheroidal Galaxies (dSph's) suffer from uncertainties in the DM density less than the galactic center studies. This is mostly from their diminutive size being smaller than the angular resolution of most  $\gamma$ -ray observatories [18]. The DM content dSph's are typically determined with the Virial theorem, Equation (2.1), and are usually majority DM [18] in mass. DSph's tend to be ideal sources to look at for DM searches. Their environments are quiet with little

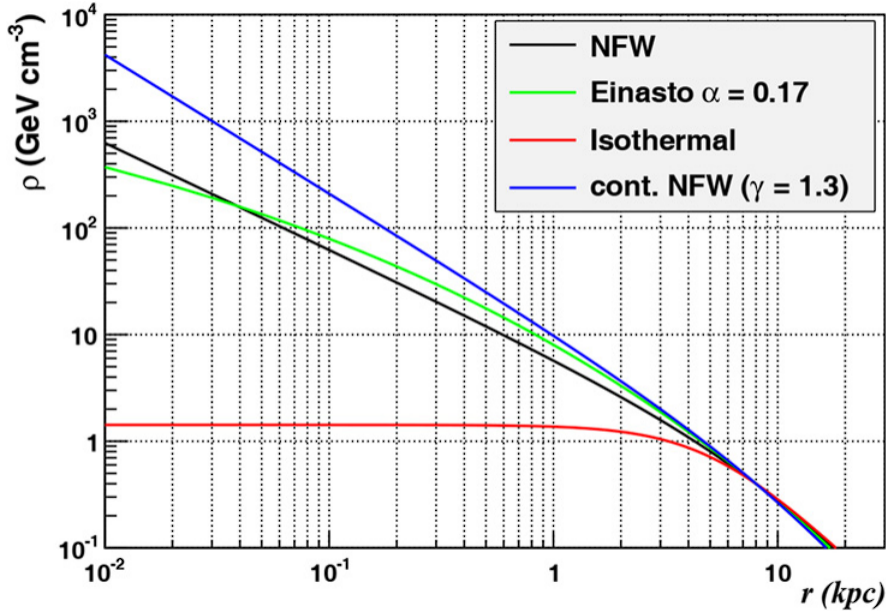


Figure 2.12 Different dark matter density profiles compared. Some models produce exceptionally large densities at small  $r$  [20].

528 astrophysical background. Unlike the galactic center, the most active components of dSph's are the  
 529 stars within them versus a violent accretion disc around a black hole. All this together means that  
 530 dSph's are among the best sources to look at for indirect DM searches. dSph's are the targets of  
 531 focus for this thesis.

## 532 2.6 Multi-Messenger Dark Matter

533 Astrophysics entered a new phase in the past few decades that leverages our increasing sensitivity  
 534 to SM channels and general relativity (GR). Up until the 21st century, astrophysical observations  
 535 were performed with photons ( $\gamma$ ) only. Astrophysics with this 'messenger' is fairly mature now.  
 536 Novel observations of the universe have since only adjusted the sensitivity of the wavelength of  
 537 light that is observed except at MeV energies. Gems like the CMB [10], and more have ultimately  
 538 been observations of different wavelengths of light. Multi-messenger astrophysics proposes using  
 539 other SM particles such the  $p^{+/-}$ , or  $\nu$  or gravitation waves predicted by general relativity.

540 The experiment LIGO had a revolutionary discovery in 2016 with the first detection of a binary  
 541 black hole merger [21]. This opened the collective imagination to observing the universe through  
 542 gravitational waves. There has also been a surge of interest in the neutrino ( $\nu$ ) sector. IceCube

543 demonstrated that we are sensitive to neutrinos in regions that correlate with significant photon  
 544 emission like the galactic plane [22]. Neutrinos, like gravitational waves and light, travel mostly  
 545 unimpeded from their source to our observatories. This makes pointing to the originating source  
 546 of these messengers much easier than it is for cosmic rays which are deflected from their source by  
 547 magnetic fields.

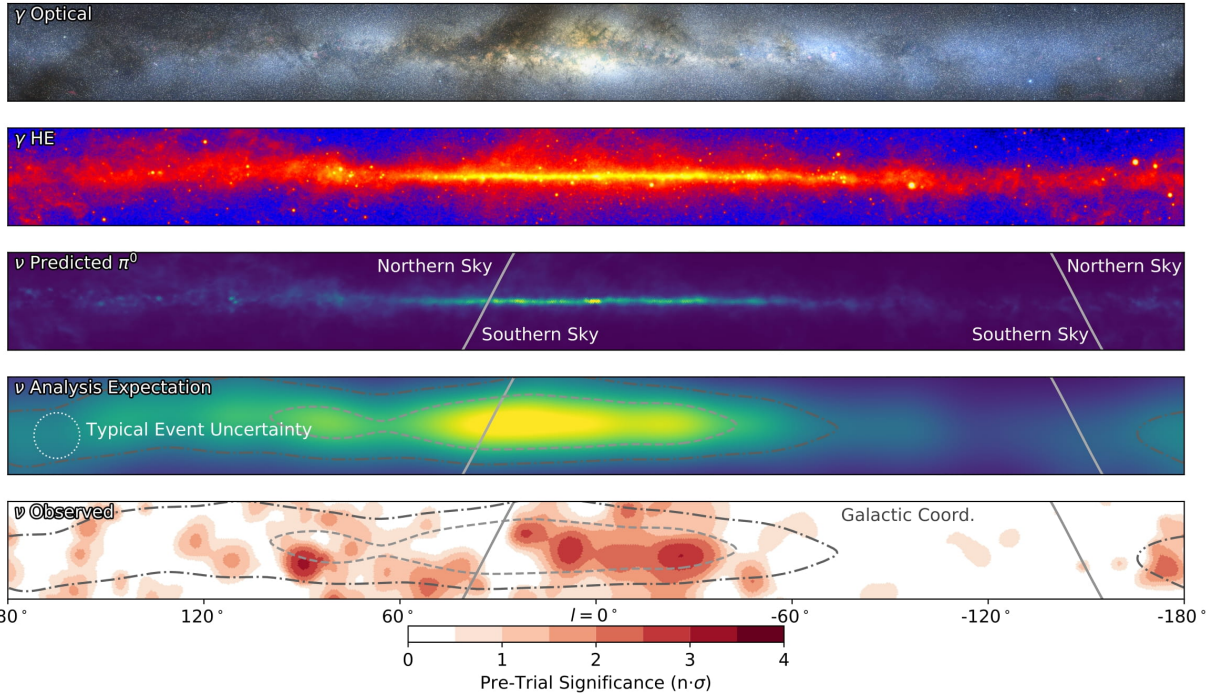


Figure 2.13 The Milky Way Galaxy in photons ( $\gamma$ ) and neutrinos ( $\nu$ ) [22]. The Galactic center is at  $l=0^\circ$  and is the brightest region in all panels. (top) An Optical color image of the Milky Way galaxy seen from Earth. Clouds of gas and dust obscure some light from stars. (2nd down) Integrated flux of  $\gamma$ -rays observed by the Fermi-LAT telescope [23]. (middle) Expected neutrino emission that corresponds with Fermi-LAT observations. (2nd up) Expected neutrino emission profile after considering detector systematics of IceCube. (bottom) Observed neutrino emission from region of the galactic plane. Substantial neutrino emission was detected.

548 The IceCube collaboration recently published a groundbreaking result of the Milky Way in  
 549 neutrinos. The recent result from IceCube, shown in Figure 2.13, proves that we can make  
 550 observations under different messenger regimes. The top two panels show the appearance of the  
 551 galactic plane to different wavelengths of light. Some sources are more apparent in some panels,  
 552 while others are not. This new channel is powerful because neutrinos are readily able to penetrate  
 553 through gas and dust in the Milky Way. This new image also refines our understanding of how high

554 energy particles are produced. For example, the fit to IceCube data prefers neutrino production  
 555 from the decay of  $\pi^0$  [22].

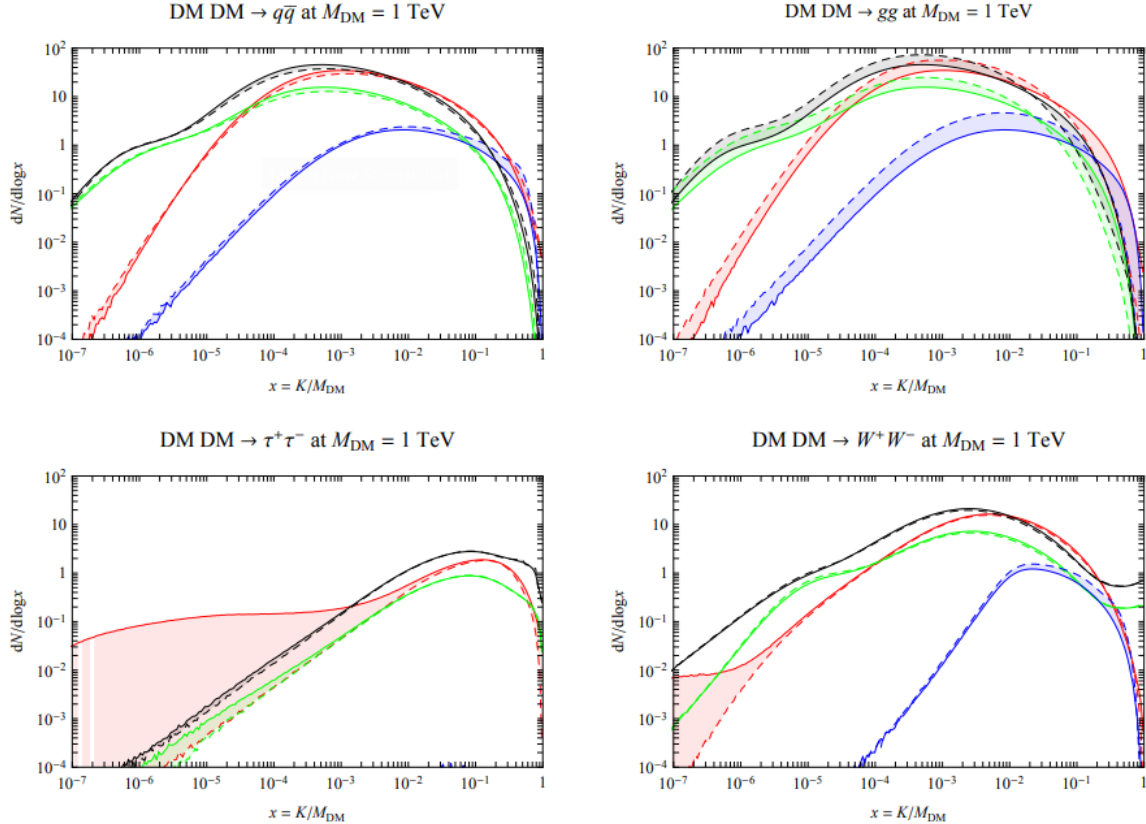


Figure 2.14 Dark Matter annihilation spectra for different final state particle and standard model annihilation channels [24]. Photons (red),  $e^\pm$  (green),  $\bar{p}$  (blue),  $\nu$  (black).

556 Exposing our observations to more cosmic messengers greatly increases our sensitivity to  
 557 rare processes. In the case of DM, Figure 2.14, there are many SM particles produced in DM  
 558 annihilation. Among the final state fluxes are gammas and neutrinos. Charged particles are also  
 559 produced however they would not likely make it to Earth since they will be deflected by magnetic  
 560 fields between the source and Earth. This means observatories that can see the neutral messengers  
 561 are especially good for DM searches and for combining data for a multi-messenger DM search.

## CHAPTER 3

### 562 MULTIMESSENGER ASTROPHYSICS: DETECTING HIGH ENERGY NEUTRAL 563 MESSENGERS

#### 564 3.1 Introduction

565 Before the 20th century, all astrophysics observations were optical in nature. We literally only  
566 saw things with highly magnified optical observations. Then we discovered cosmic rays. cosmic  
567 rays are charged particles, typically naked protons or H+. This was seen by Victor Hess in 19??.  
568 Around the same time we discovered neutrinos from beta decay. Sometime around 1950 we started  
569 to build neutrino detectors which were mostly sensitive to neutrinos from the sun. Finally, it was  
570 theorized that compact objects like black holes and neutron stars would create waves in space-time  
571 when they experience mergers or collisions.

572 In the 21st century, we have developed new observation techniques and detectors that are no only  
573 sensitive to these four messengers - photons ([TODO: photon](#)), neutrinos ([TODO: nu](#)), Cosmic  
574 Rays (CR), and Gravitational Wave (WV) - we're collect high energy versions of these events.  
575 For the standad model particles, we're now sensitive to all messengers above the MeV eneryg  
576 range. Additionally, the GW's were sensitive to are in the stellar mass black hole region and above  
577 within our galactic neighborhood. This means were becoming sensitive to the fundamental physics  
578 occuring within the universe and we can rely on the universe as a TeV+ particle accelerator. We  
579 also have the abaility to correlate high energy events across messengers and gain new insights on  
580 the processes that occur in our universe.

581 This thesis focuses on very high energy (VHE) gamma rays and neutrinos. These can both be  
582 observed through the water cherenkov detection technique altho not exclusively. Methods on how  
583 to detect and observe these neutral messengers are discussed Section 3.3 and Section 3.4

#### 584 3.2 Charged Particles in a Medium

585 For high enery gamma-rays and neutrinos, we can exploit the same effect that charged particles  
586 have with water. This effect is known as Cherenkov radiation. Cherenkov Radiation occurs when a  
587 charged particle, usually electrons ( $e$ ) or muons ( $\mu$ ), traverse a medium, like water, faster than the

588 speed of light in that medium. This is similar to sonic boom where an object moves through air  
589 faster than the speed of sound in air. Cherenkov radiation can therefore be thought of as an 'optic  
590 boom'. Many astro-particle physics experiments will use water as the medium as because water  
591 has a unique set of properties ideal for charged particle tracking.



Figure 3.1 TODO: Show a nuclear reactor with cherenkov radiation[NEEDS A SOURCE][FACT CHECK THIS]

592 The frequency of light emitted due to cherenkov radiation follows the equation:

$$INSERT\ Cherenkov\ wavelength\ calc\ HERE. \quad (3.1)$$

593 The absorption spectra is shown in the following figure:

594 **3.3 Photons ( $\gamma$ )**

595 **3.4 Neutrinos ( $\nu$ )**

596 **3.5 Opportunities to Combine for Dark Matter**



Figure 3.2 TODO: absorption spectrum of liquid and solid water[NEEDS A SOURCE][FACT CHECK THIS]

## CHAPTER 4

597

### HIGH ALTITUDE WATER CHERENKOV (HAWC) OBSERVATORY

598 **4.1 The Detector**

599 **4.2 Events Reconstruction and Data Acquisition**

600 **4.2.1 G/H Discrimination**

601 **4.2.2 Angle**

602 **4.2.3 Energy**

603 **4.3 Remote Monitoring**

604 **4.3.1 ATHENA Database**

605 **4.3.2 HOMER**

606

## **CHAPTER 5**

### **ICECUBE NEUTRINO OBSERVATORY**

607 **5.1 The Detector**

608 **5.2 Events Reconstruction and Data Acquisition**

609 **5.2.1 Angle**

610 **5.2.2 Energy**

611 **5.3 Northern Test Site**

612 **5.3.1 PIgeon remote dark rate testing**

613 **5.3.2 Bulkhead Construction**

## CHAPTER 6

### COMPUTATIONAL TECHNIQUES IN PARTICLE ASTROPHYSICS

615 **6.1 Neural Networks for Gamma/Hadron Separation**

616 **6.2 Parallel Computing for Dark Matter Analyses**

## CHAPTER 7

### GLORY DUCK: MULTI-WAVELENGTH SEARCH FOR DARK MATTER ANNIHILATION TOWARDS DWARF SPHEROIDAL GALAXIES

#### 7.1 Introduction

The field of astrophysics now has several instruments and observatories sensitive to high energy gamma-rays. The energy sensitivity for the modern gamma-ray program spans many orders of magnitude. Figure 7.1 demonstrates these similar sensitivities across energies for the five experiments: Fermi-LAT, HAWC, HESS, MAGIC, and VERITAS.

Each of the five experiments featured in Figure 7.1 have independently searched for DM annihilation from dwarf spheroidal galaxies (dSph) and set limits. Intriguingly, there are regions of substantial overlap in their energy sensitivities. This clearly motivates an analysis that combines data from these five. Each experiment has unique gamma-ray detection methods and their weaknesses and strengths can be leveraged with each other. The HAWC gamma-ray observatory is extensively introduced in chapter 4, so it is not introduced here. A brief description of the remaining experiments are in the following paragraphs.

The Large Area Telescope (LAT) is a pair conversion telescope mounted on the NASA Fermi satellite in orbit  $\sim$ 550 km above the Earth [26]. LAT's field of view covers about 20% of the whole sky, and it sweeps the whole sky approximately every 3 hours. LAT's gamma-ray energy sensitivity ranges from 20 MeV up to 1 TeV. Previous DM searches towards dSphs using Fermi-LAT are published in [27] and [28]

The High Energy Spectroscopic System (HESS), Major Atmospheric Gamma Imaging Cherenkov (MAGIC), and Very Energetic Radiation Imaging Telescope Array System (VERITAS) are arrays of Imaging Atmospheric Cherenkov Telescopes (IACT). These telescopes observe the Cherenkov light emitted from gamma-ray showers in the Earth's atmosphere. The field of view for these telescopes is no larger than  $5^\circ$  with energy sensitivities ranging from 30 GeV up to 100 TeV [29, 30, 31]. IACTs are able to make precise observations in selected regions of the sky, however can only be operated in ideal dark conditions. HESS's observations of the dwarves

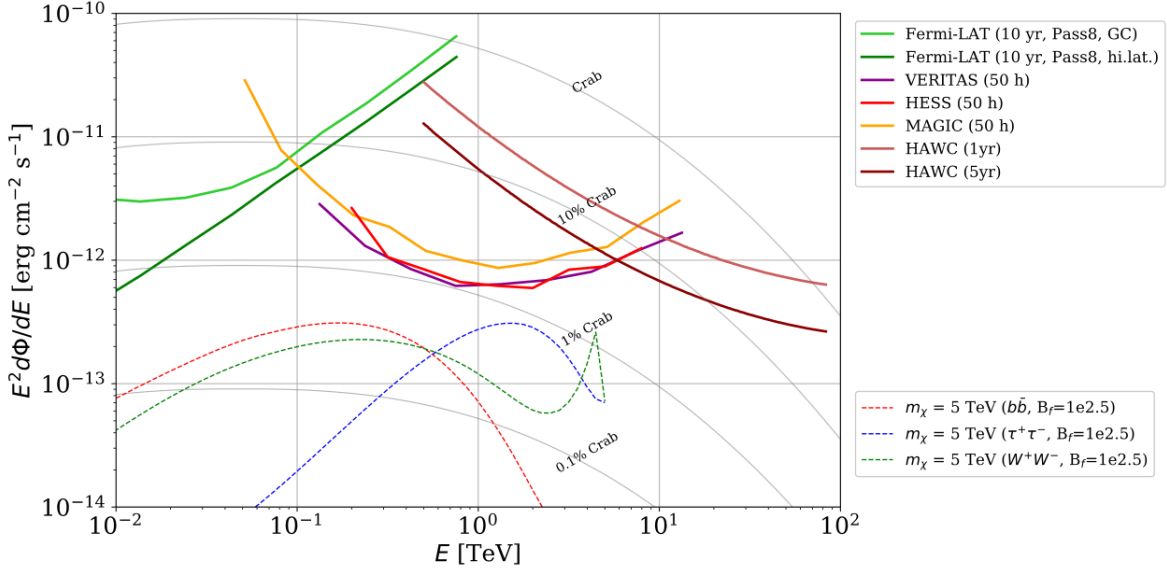


Figure 7.1 Sensitivities of five gamma-ray experiments compared to percentages of the Crab nebula’s emission and dark matter annihilation. Solid lines present estimated sensitivities to power law spectra [FACT CHECK THIS] for each experiment. Green lines are Fermi-LAT sensitivities where lighter green is the sensitivity to the galactic center and dark green is its sensitivity to higher declinations. Orange, red, and purple solid lines represent the MAGIC, HESS, and VERITAS 50 hour sensitivities respectively. The maroon and brown lines are the HAWC 1 year and 5 year sensitivities. Across four decades of gamma-ray energy, these experiments have similar sensitivities on the order  $10^{-12}$  erg  $\text{cm}^{-2}\text{s}^{-1}$ . The dotted lines are estimated dark matter fluxes assuming  $m_\chi = 5$  TeV DM annihilating to bottom quarks (red), tau leptons (blue), and W bosons (green). Faded gray lines outline percentage flux of the Crab nebula. Figure is an augmented version of [25]

643 Sculptor and Carina were between January 2008 and December 2009. HESS’s observations of  
 644 Coma Berenices were from 2010 to 2013, and Fornax was observed in 2010 [32, 33, 34]. MAGIC  
 645 provided deep observations of Segue1 between 2011 and 2013 [35]. MAGIC also provides data  
 646 for three dwarves: Coma Berenices, Draco, and Ursa Major II where observations were made  
 647 in: January - June 2019 [36], March - September 2018 [36], and 2014 - 2016 [37] respectively.  
 648 VERITAS provided data for Boötes I, Draco, Segue 1, and Ursa Minor from 2009 to 2016 [38].

649 This chapter presents the Glory Duck analysis, the name given for the search for dark matter  
 650 annihilation from dSph by combining data from the five gamma-ray observatories: Fermi-LAT,  
 651 HAWC, HESS, MAGIC, and VERITAS. Specifically, the methods in analysis and modeling are  
 652 presented for the HAWC gamma-ray observatory. This work was published to the Journal of  
 653 Cosmology and Astroparticle Physics and presented at the International Cosmic Ray Conference

654 in 2019, 2021, and 2023 [39, 40, 41] and others.

655 **7.2 Dataset and Background**

656 This section enumerates the data and background methods used for HAWC's study of dSphs.

657 Section 7.2.1 and Section 7.2.2 are most useful for fellow HAWC collaborators looking to replicate

658 the Glory Duck analysis.

659 **7.2.1 Itemized HAWC files**

660 • Detector Resolution: `response_aerie_svn_27754_systematics_best_mc_test_no`  
661 `broadpulse\_10pctlogchargesmearing_0.63qe_25kHzNoise_run5481_curvatu`  
662 `re0_index3.root`

663 • Data Map: `maps-20180119/liff/maptree_1024.root`

664 • Spectral Dictionary: `DM_CirrelliSpectrum_dict_gammas.npy`

665 • Analysis wiki: [https://private.hawc-observatory.org/wiki/index.php/Glory\\_Duck\\_Multi-Experiment\\_Dark\\_Matter\\_Search](https://private.hawc-observatory.org/wiki/index.php/Glory_Duck_Multi-Experiment_Dark_Matter_Search)

667 **7.2.2 Software Tools and Development**

668 This analysis was performed using HAL and 3ML [42, 43] in Python version 2. I built software  
669 to implement the *A Poor Particle Physicist Cookbook for Dark Matter Indirect Detection* (PPPC)  
670 [44] DM spectral model and dSphs spatial model from [45] for HAWC analysis. A NumPy version  
671 of this dictionary was made for both Py2 and Py3. The code base for creating this dictionary is  
672 linked on my GitLab sandbox:

673 • Py2: [Dictionary Generator \(Deprecated\)](#)

674 • Py3: [PPPC2Dict](#)

675 The analysis was performed using the  $f_{\text{hit}}$  framework performed in the HAWC Crab paper  
676 [42]. The Python2 NumPy dictionary file for gamma-ray final states is `dmCirSpecDict.npy`. The  
677 corresponding Python3 file is `DM_CirrelliSpectrum_dict_gammas.npy`. These files can also

678 be used for decay channels and the PPPC describes how [44]. All other software used for data  
679 analysis, DM profile generation, and job submission to SLURM are also kept in my sandbox for  
680 [the Glory Duck](#) project.

681 **7.2.3 Data Set and Background Description**

682 The HAWC data maps used for this analysis contain 1017 days of data between runs 2104  
683 (2014-11-26) and 7476 (2017-12-20). They were generated from pass 4.0 reconstruction. The  
684 analysis is performed using the  $f_{hit}$  energy binning scheme with bins (1-9) similar to what was done  
685 for the Crab and previous HAWC dSph analysis [42, 46]. Bin 0 was excluded as it has substantial  
686 hadronic contamination and poor angular resolution.

687 This analysis was done on dSphs because of their large DM mass content relative to baryonic  
688 mass. We consider the following to estimate the background to this study.

- 689 • The dSphs are small in HAWC’s field of view, so the analysis is not sensitive to large or small  
690 scale anisotropies.
- 691 • The dSphs used in this analysis are off the galactic plane.
- 692 • The dSphs are baryonically faint relative to their expected dark matter content and are not  
693 expected to contain high energy gamma-ray sources.

694 Therefor we make no additional assumptions on the background from our sources and use  
695 HAWC’s standard direct integration method for background estimation [42]. It is possible for  
696 gamma rays from DM annihilation to scatter in transit to HAWC via Inverse Compton Scattering  
697 (ICS). This was investigated and its impact on the flux is basically zero. Supporting information  
698 on this is in Section 7.7.1

699 **7.3 Analysis**

700 The expected differential photon flux from DM-DM annihilation to standard model particles,  
701  $d\Phi_\gamma/dE_\gamma$ , over solid angle,  $\Omega$  is described by the familiar equation.

$$\frac{d\Phi_\gamma}{dE_\gamma} = \frac{\langle\sigma v\rangle}{8\pi m_\chi^2} \frac{dN_\gamma}{dE_\gamma} \times \int_{\text{source}} d\Omega \int_{l.o.s} \rho_\chi^2 dl(r, \theta') \quad (7.1)$$

702 Where  $\langle \sigma v \rangle$  is the velocity weighted annihilation cross-section.  $\frac{dN}{dE}$  is the expected differential  
 703 number of photons produced at each energy per annihilation.  $m_\chi$  is the rest mass of the supposed  
 704 DM particle.  $\rho_\chi$  is the DM density.  $J$  is the astrophysical J-factor and is defined as

$$J = \int d\Omega \int_{l.o.s} dl \rho_\chi^2(r, \theta') \quad (7.2)$$

705  $l$  is the distance to the source from Earth.  $r$  is the radial distance from the center of the source.  $\theta'$  is  
 706 the half angle defining a cone containing the DM source. How each component is synthesized and  
 707 considered for HAWC's analysis is presented in the following sections. Section 7.3.1 presents the  
 708 particle physics model for DM annihilation. Section 7.3.2 presents the spatial distributions built  
 709 for each dSph.

### 710 7.3.1 $\frac{dN_\gamma}{dE_\gamma}$ - Particle Physics Component

711 For these spectra, we import the PPPC with Electroweak (EW) corrections [44]. The spectrum  
 712 is implemented as a model script in astromodels for 3ML. The EW corrections were previously not  
 713 considered for HAWC and are significant for DM annihilating to EW coupled SM particles such  
 714 as all leptons, and the  $\gamma$ ,  $Z$ , and  $W$  bosons [46]. Figure 7.2 demonstrates the significance of EW  
 715 corrections for W boson annihilation. Across EW SM channels, the gamma-ray spectra become  
 716 harder than spectra without EW corrections. Tables from the PPPC were reformatted into Python  
 717 NumPy dictionaries for collaboration-wide use. A class in astromodels was developed to include  
 718 the EW correction from the PPPC and is aptly named `PPPCSpectra` within `DM_models.py`.

### 719 7.3.2 $J$ - Astrophysical Component

720 The J-factor profiles for each source are imported from Geringer-Sameth (referred to with  $\mathcal{GS}$ )  
 721 [45]. These were pulled from the publication as  $J(\theta)$ , where  $\theta$  is the angular separation from the  
 722 center of the source. HAWC requires maps in terms of  $\frac{dJ}{d\Omega}$ , so the conversion from the maps was  
 723 done in the following way...

724 First, convert the angular distances to solid angles

$$\Omega = 2 \cdot \pi(1 - \cos(\theta)) \quad (7.3)$$

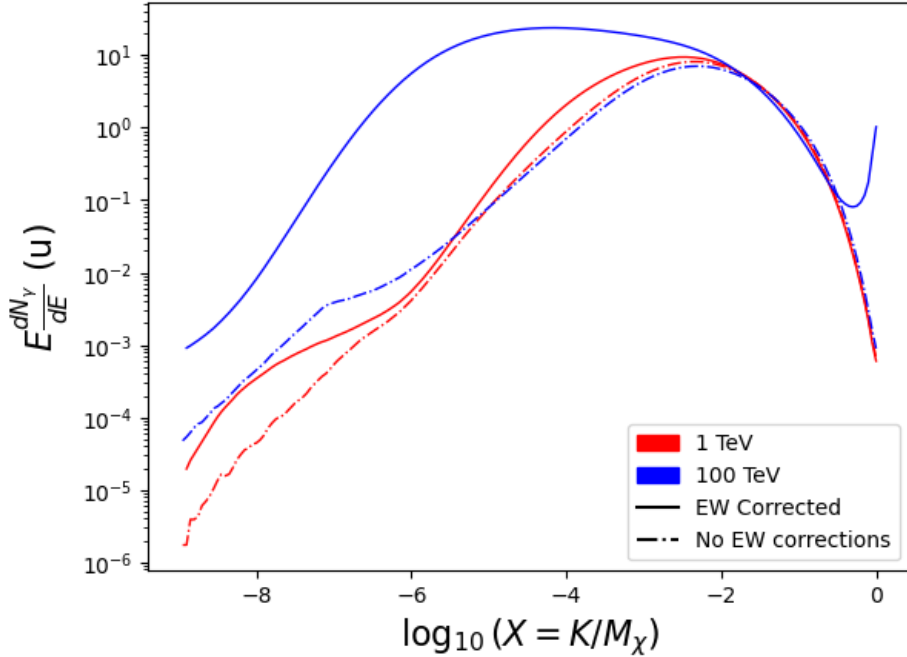


Figure 7.2 Effect of Electroweak (EW) corrections on expected DM annihilation spectrum for  $\chi\chi \rightarrow W^-W^+$ . Solid lines are spectral models that consider EW corrections. Dash-dot lines are spectral models without EW corrections. Red lines are models for  $M_\chi = 1$  TeV. Blue lines represent models for  $M_\chi = 100$  TeV. All models are sourced from the PPPC4DMID [44].

725 which reduces with a small angle approximation to  $\pi\theta^2$ . Next, the central difference for both the  
 726  $\Delta J$  and  $\Delta\Omega$  value were calculated from the discretized  $J(\theta)$  with the central difference stencil:

$$\Delta\phi_i = \phi_{i+1} - \phi_{i-1} \quad (7.4)$$

727 Where  $\phi$  is either  $\Omega$  or  $J$ . These were done separately in case the grid spacing in  $\theta$  was not uniform.  
 728 Finally, these lists are divided so that we are left with an approximation of the  $dJ/d\Omega$  profile that  
 729 is a function of  $\theta$ . Admittedly, this is an approximation method for the map which introduces small  
 730 errors compared to the true profile estimate. This was checked as a systematic against the author's  
 731 profiling of the spatial distribution and is documented in Section 7.8.1.

732 With  $\frac{dJ}{d\Omega}(\theta)$ , a map is generated, first by filling in the north-east quadrant of the map. This  
 733 quadrant is then reflected twice, vertically then horizontally, to fill the full map. Maps are then  
 734 normalized by dividing the discrete 2D integral of the map. The 2D integral was a simple height

735 of bins, Newton’s integral:

$$p^2 \cdot \sum_{i,j=0}^{N,M} \frac{dJ}{d\Omega}(\theta_{i,j}, \phi_{i,j}) \quad (7.5)$$

736 These maps are HEALpix maps with NSIDE 16384 and saved in the `.fits` format.

737 Another DM spatial distribution model from Bonnivard ( $\mathcal{B}$ ) [47] was used for the Glory Duck  
738 study. However, to save computational time, limits from  $\mathcal{GS}$  were scaled to  $\mathcal{B}$  instead of each  
739 experiment performing a full study a second time. How these models compare is demonstrated  
740 for each dSph in Figure 7.16 and Figure 7.17 Plots of these maps are provided for each source  
741 in chapter A Examples of the two most impactful dSphs derived from  $\mathcal{GS}$ , Segue1 and Coma  
742 Berenices are featured in Figure 7.3

### 743 7.3.3 Source Selection and Annihilation Channels

744 We use many of the dSphs presented in HAWC’s previous dSph DM search [46]. HAWC’s  
745 sources for Glory Duck include Boötes I, Coma Berenices, Canes Venatici I + II, Draco, Hercules,  
746 Leo I, II, + IV, Segue 1, Sextans, and Ursa Major I + II. A full description of all sources used  
747 in Glory Duck is found in Table 7.1. Triangulum II was excluded from the Glory Duck analysis  
748 because of large uncertainties in its  $J$  factor. Ursa Minor was excluded from HAWC’s contribution  
749 to the combination because the source extension model extended Ursa Minor beyond HAWC’s field  
750 of view. Ursa Minor was not expected to contribute significantly to the combined limit, so work  
751 was not invested in a solution to include Ursa Minor.

752 This analysis improves on the previous HAWC dSph paper [46] in the following ways. Pre-  
753 viously, the dSphs were treated and implemented as point sources. For this analysis, dSphs are  
754 modeled and treated as extended source. The impact of this change with respect to the upper limit  
755 is source dependent and is explored in Section 7.7.2. Previously, the particle physics model used for  
756 gamma-ray spectra from DM annihilation did not have EW corrections where the PPPC includes  
757 them. Finally, the gamma-ray ray dataset is much larger. The study performed here analyzes over  
758 1000 days of data compared to 507.

759 The SM annihilation channels probed for the Glory Duck combination include  $b\bar{b}$ ,  $e\bar{e}$ ,  $\mu\bar{\mu}$ ,  $\tau\bar{\tau}$ ,  
760  $t\bar{t}$ ,  $W^+W^-$ , and  $ZZ$ . A summary of all sources, with a description of each experiments’ sensitivity

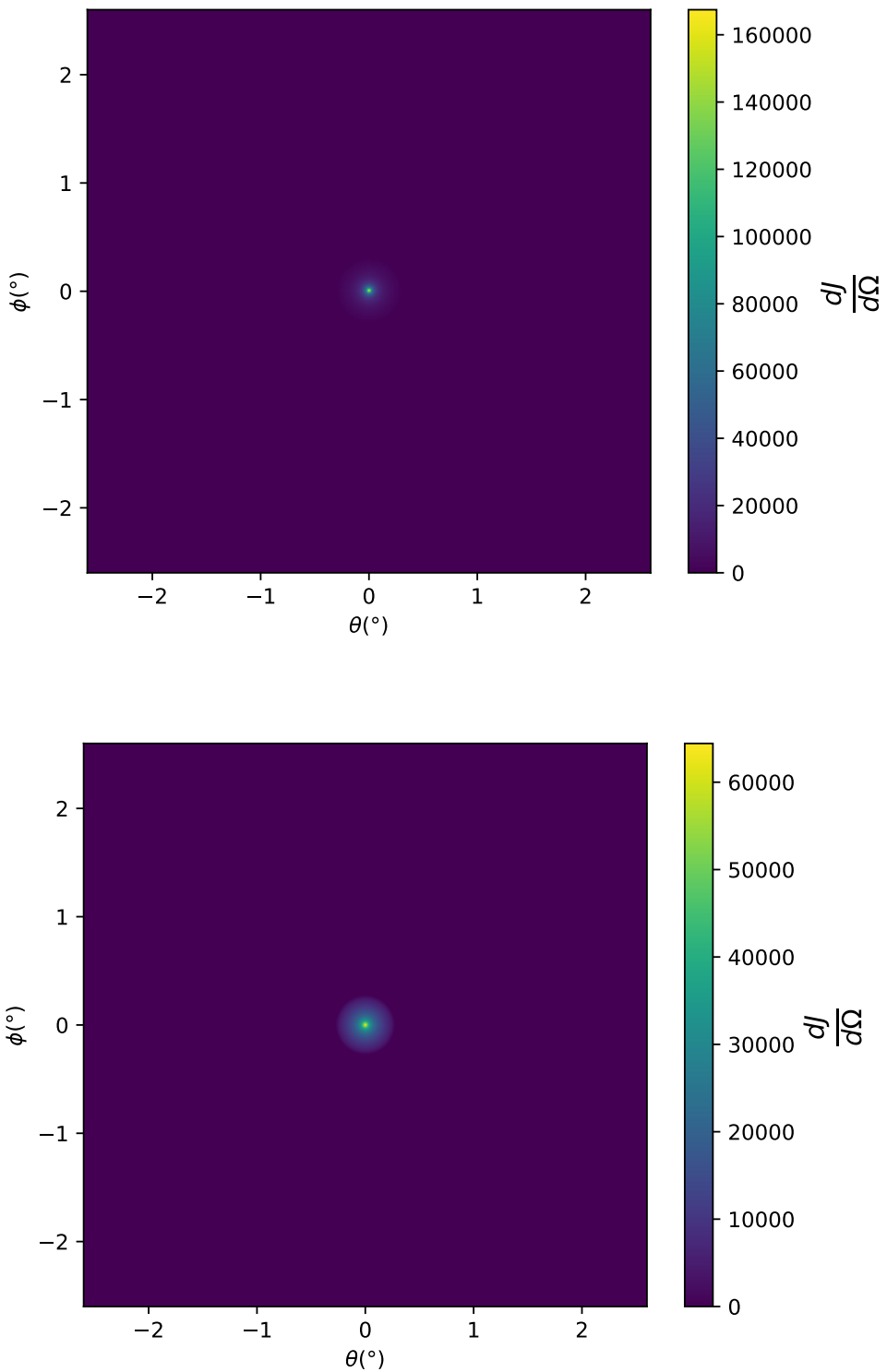


Figure 7.3  $\frac{dJ}{d\Omega}$  maps for Segue1 (top) and Coma Berenices (bottom). Origin is centered on the specific dwarf spheroidal galaxies (dSph). X and Y axes are the angular separation from the center of the dwarf. Plots of the remaining 11 dSph HAWC studied are linked in Fig. A.1.

Table 7.1 Summary of the relevant properties of the dSphs used in the present work. Column 1 lists the dSphs. Columns 2 and 3 present their heliocentric distance and galactic coordinates, respectively. Columns 4 and 5 report the  $J$ -factors of each source given from the  $\mathcal{GS}$  and  $\mathcal{B}$  independent studies and their estimated  $\pm 1\sigma$  uncertainties. The values  $\log_{10} J$  ( $\mathcal{GS}$  set) [45] correspond to the mean  $J$ -factor values for a source extension truncated at the outermost observed star. The values  $\log_{10} J$  ( $\mathcal{B}$  set) [47] are provided for a source extension at the tidal radius of each dSph. **Bolded sources are within HAWC's field of view and provided to the Glory Duck analysis.**

Name	Distance (kpc)	$l, b$ ( $^{\circ}$ )	$\log_{10} J$ ( $\mathcal{GS}$ set) $\log_{10}(\text{GeV}^2 \text{cm}^{-5} \text{sr})$	$\log_{10} J$ ( $\mathcal{B}$ set) $\log_{10}(\text{GeV}^2 \text{cm}^{-5} \text{sr})$
<b>Boötes I</b>	66	358.08, 69.62	$18.24^{+0.40}_{-0.37}$	$18.85^{+1.10}_{-0.61}$
<b>Canes Venatici I</b>	218	74.31, 79.82	$17.44^{+0.37}_{-0.28}$	$17.63^{+0.50}_{-0.20}$
<b>Canes Venatici II</b>	160	113.58, 82.70	$17.65^{+0.45}_{-0.43}$	$18.67^{+1.54}_{-0.97}$
Carina	105	260.11, -22.22	$17.92^{+0.19}_{-0.11}$	$18.02^{+0.36}_{-0.15}$
<b>Coma Berenices</b>	44	241.89, 83.61	$19.02^{+0.37}_{-0.41}$	$20.13^{+1.56}_{-1.08}$
<b>Draco</b>	76	86.37, 34.72	$19.05^{+0.22}_{-0.21}$	$19.42^{+0.92}_{-0.47}$
Fornax	147	237.10, -65.65	$17.84^{+0.11}_{-0.06}$	$17.85^{+0.11}_{-0.08}$
<b>Hercules</b>	132	28.73, 36.87	$16.86^{+0.74}_{-0.68}$	$17.70^{+1.08}_{-0.73}$
<b>Leo I</b>	254	225.99, 49.11	$17.84^{+0.20}_{-0.16}$	$17.93^{+0.65}_{-0.25}$
<b>Leo II</b>	233	220.17, 67.23	$17.97^{+0.20}_{-0.18}$	$18.11^{+0.71}_{-0.25}$
<b>Leo IV</b>	154	265.44, 56.51	$16.32^{+1.06}_{-1.70}$	$16.36^{+1.44}_{-1.65}$
Leo V	178	261.86, 58.54	$16.37^{+0.94}_{-0.87}$	$16.30^{+1.33}_{-1.16}$
Leo T	417	214.85, 43.66	$17.11^{+0.44}_{-0.39}$	$17.67^{+1.01}_{-0.56}$
Sculptor	86	287.53, -83.16	$18.57^{+0.07}_{-0.05}$	$18.63^{+0.14}_{-0.08}$
<b>Segue I</b>	23	220.48, 50.43	$19.36^{+0.32}_{-0.35}$	$17.52^{+2.54}_{-2.65}$
Segue II	35	149.43, -38.14	$16.21^{+1.06}_{-0.98}$	$19.50^{+1.82}_{-1.48}$
<b>Sextans</b>	86	243.50, 42.27	$17.92^{+0.35}_{-0.29}$	$18.04^{+0.50}_{-0.28}$
<b>Ursa Major I</b>	97	159.43, 54.41	$17.87^{+0.56}_{-0.33}$	$18.84^{+0.97}_{-0.43}$
<b>Ursa Major II</b>	32	152.46, 37.44	$19.42^{+0.44}_{-0.42}$	$20.60^{+1.46}_{-0.95}$
Ursa Minor	76	104.97, 44.80	$18.95^{+0.26}_{-0.18}$	$19.08^{+0.21}_{-0.13}$

761 to the source, is provided in Table 7.2.

## 762 7.4 Likelihood Methods

### 763 7.4.1 HAWC Likelihoods

764 For every analysis bin in energy,  $f_{hit}$  bins (1-9), and location, we can expect  $N$  signal events and  
765  $B$  background events. The expected number of excess signal events from dark matter annihilation,

Table 7.2 Summary of dSph observations by each experiment used in this work. A ‘-’ indicates the experiment did not observe the dSph for this study. For Fermi-LAT, the exposure at 1 GeV is given. For HAWC,  $|\Delta\theta|$  is the absolute difference between the source declination and HAWC latitude. HAWC is more sensitive to sources with smaller  $|\Delta\theta|$ . For IACTs, we show the zenith angle range, the total exposure, the energy range, the angular radius  $\theta$  of the signal or ON region, the ratio of exposures between the background-control (OFF) and signal (ON) regions ( $\tau$ ), and the significance of gamma-ray excess in standard deviations,  $\sigma$ .

Source name	Fermi-LAT	HAWC	H.E.S.S, MAGIC, VERITAS						
	Exposure ( $10^{11}$ s m $^2$ )	$ \Delta\theta $ ( $^\circ$ )	IACT	Zenith ( $^\circ$ )	Exposure (h)	Energy range (GeV)	$\theta$ ( $^\circ$ )	$\tau$	$S$ ( $\sigma$ )
Boötes I	2.6	4.5	VERITAS	15 – 30	14.0	100–41000	0.10	8.6	-1.0
Canes Venatici I	2.9	14.6	–	–	–	–	–	–	–
Canes Venatici II	2.9	15.3	–	–	–	–	–	–	–
Carina	3.1	–	H.E.S.S.	27 – 46	23.7	310 – 70000	0.10	18.0	-0.3
Coma Berenices	2.7	4.9	H.E.S.S.	47 – 49	11.4	550 – 70000	0.10	14.4	-0.4
			MAGIC	5 – 37	49.5	60 – 10000	0.17	1.0	–
			MAGIC	29 – 45	52.1	70 – 10000	0.22	1.0	–
Draco	3.8	38.1	VERITAS	25 – 40	49.8	120 – 70000	0.10	9.0	-1.0
Fornax	2.7	–	H.E.S.S.	11 – 25	6.8	230 – 70000	0.10	45.5	-1.5
Hercules	2.8	6.3	–	–	–	–	–	–	–
Leo I	2.5	6.7	–	–	–	–	–	–	–
Leo II	2.6	3.1	–	–	–	–	–	–	–
Leo IV	2.4	19.5	–	–	–	–	–	–	–
Leo V	2.4	–	–	–	–	–	–	–	–
Leo T	2.6	–	–	–	–	–	–	–	–
Sculptor	2.7	–	H.E.S.S.	10 – 46	11.8	200 – 70000	0.10	19.8	-2.2
Segue I	2.5	2.9	MAGIC	13 – 37	158.0	60 – 10000	0.12	1.0	-0.5
			VERITAS	15 – 35	92.0	80 – 50000	0.10	7.6	0.7
Segue II	2.7	–	–	–	–	–	–	–	–
Sextans	2.4	20.6	–	–	–	–	–	–	–
Ursa Major I	3.4	32.9	–	–	–	–	–	–	–
Ursa Major II	4.0	44.1	MAGIC	35 – 45	94.8	120 – 10000	0.30	1.0	-2.1
Ursa Minor	4.1	–	VERITAS	35 – 45	60.4	160 – 93000	0.10	8.4	-0.1

766  $S$ , is estimated by convolving Equation (7.1) with HAWC's energy response and pixel point spread  
 768 functions. I then compute the test statistic (TS) with the log-likelihood ratio test,

$$\text{TS} = -2 \ln \left( \frac{\mathcal{L}_0}{\mathcal{L}^{\max}} \right) \quad (7.6)$$

769 where  $\mathcal{L}_0$  is the null hypothesis, or no DM emission, likelihood.  $\mathcal{L}^{\max}$  is the best fit signal  
 770 hypothesis where  $\langle \sigma v \rangle$  maximizes the likelihood. We calculate the likelihood of each source and  
 771 model, assuming events are Poisson distributed, with

$$\mathcal{L} = \prod_i \frac{(B_i + S_i)^{N_i} e^{-(B_i + S_i)}}{N_i!} \quad (7.7)$$

772 where  $S_i$  is the sum of expected number of signal counts.  $B_i$  is the number of background counts  
 773 observed.  $N_i$  is the total number of counts.

774 I also calculate an upper limit on  $\langle \sigma v \rangle$  by calculating the 95% confidence level (CL). For the  
 775 CL, we define a parameter,  $\text{TS}_{95}$ , as

$$\text{TS}_{95} \equiv \sum_{\text{bins}} \left[ 2N \ln \left( 1 + \frac{\epsilon S_{\text{ref}}}{B} \right) - 2\epsilon S_{\text{ref}} \right] \quad (7.8)$$

776 where the expected signal counts from a dSph is scaled by  $\epsilon$ .  $S_{\text{ref}}$  is the expected number of excess  
 777 counts in a bin from DM emission from a dSph with a corresponding annihilation cross-section,  
 778  $\langle \sigma v \rangle$ . We scan  $\epsilon$  such that

$$2.71 = \text{TS}_{\max} - \text{TS}_{95} \quad (7.9)$$

#### 779 7.4.2 Glory Duck Joint Likelihood

780 The joint likelihood for the 5-experiment combination was done similarly as Section 7.4.1. We  
 781 calculate upper limits on  $\langle \sigma v \rangle$  from the TS, Eq. (7.6), and define the likelihood ratio more generally

$$\lambda(\langle \sigma v \rangle | \mathcal{D}_{\text{dSphs}}) = \frac{\mathcal{L}(\langle \sigma v \rangle; \hat{\nu} | \mathcal{D}_{\text{dSphs}})}{\mathcal{L}(\widehat{\langle \sigma v \rangle}; \hat{\nu} | \mathcal{D}_{\text{dSphs}})} \quad (7.10)$$

782  $\mathcal{D}_{\text{dSphs}}$  is the totality of observations across experiments and dSphs.  $\nu$  are the nuisance parameters  
 783 which are the  $J$  factors in this study.  $\widehat{\langle \sigma v \rangle}$  and  $\hat{\nu}$  are the respective estimate that maximize  $\mathcal{L}$   
 784 globally. Finally,  $\hat{\nu}$  is the set of nuisance parameters that maximize  $\mathcal{L}$  for a fixed value of  $\langle \sigma v \rangle$ .

785        The *complete* joint likelihood,  $\mathcal{L}$  that encompasses all observations from all instruments and  
 786   dSphs can be factorized into *partial* functions for each dSph  $l$  (with  $\mathcal{L}_{\text{dSph},l}$ ) and its  $J$  factor ( $\mathcal{J}_l$ ):

$$\mathcal{L} (\langle \sigma v \rangle; \nu | \mathcal{D}_{\text{dSphs}}) = \prod_{l=1}^{N_{\text{dSphs}}} \mathcal{L}_{\text{dSph},l} (\langle \sigma v \rangle; J_l, \nu_l | \mathcal{D}_l) \times \mathcal{J}_l (J_l | J_{l,\text{obs}}, \sigma_{\log J_l}). \quad (7.11)$$

787   For this study,  $N_{\text{dSphs}} = 20$  is the number of dSphs studied.  $\mathcal{D}_l$  are the gamma-ray observations  
 788   of dSph,  $l$ .  $\nu_l$  are the nuisance parameters modifying the gamma-ray observations of dSph,  $l$ ,  
 789   but excludes  $\mathcal{J}_l$ .  $\mathcal{J}_l$  is the  $J$  factor for dSph,  $l$ , as defined in Equation (7.2), and it is a nuisance  
 790   parameter whose value is unknown.  $\log_{10} J_{l,\text{obs}}$  and  $\sigma_{\log J_l}$  are obtained from fitting a log-normal  
 791   function of  $J_{l,\text{obs}}$  to the posterior distribution of  $J_l$  [48].  $\log_{10} J_{l,\text{obs}}$  and  $\sigma_{\log J_l}$  values are provided  
 792   in Table 7.1. The term  $\mathcal{J}_l$  constraining  $J_l$  is written as:

$$\mathcal{J}_l (J_l | J_{l,\text{obs}}, \sigma_{\log J_l}) = \frac{1}{\ln(10) J_{l,\text{obs}} \sqrt{2\pi} \sigma_{\log J_l}} \exp\left(-\frac{(\log_{10} J_l - \log_{10} J_{l,\text{obs}})^2}{2\sigma_{\log J_l}^2}\right). \quad (7.12)$$

793   Both the  $\mathcal{GS}$  and  $\mathcal{B}$ , displayed in Table 7.1, sets of  $J$  factors are used in this analysis. Equation (7.12)  
 794   is also normalized, so it can also be interpreted as a probability density function (PDF) for  $J_{l,\text{obs}}$ .  
 795   From Equation (7.1), we can also see that  $\langle \sigma v \rangle$  and  $J_l$  are degenerate when computing  $\mathcal{L}_{\text{dSph},l}$ .  
 796   Therefore, as noted in [49], it is sufficient to compute  $\mathcal{L}_{\text{dSph},l}$  versus  $\langle \sigma v \rangle$  for a fixed value of  $J_l$ .  
 797   We used  $J_{l,\text{obs}}(\mathcal{GS})$  reported in Tab. 7.1, in order to perform the profile of  $\mathcal{L}$  with respect to  $J_l$ .  
 798   The degeneracy implies that for any  $J'_l \neq J_{l,\text{obs}}$  (in practice in our case we used  $J'_l = J_{l,\text{obs}}(\mathcal{B})$  to  
 799   compute results from a different set of  $J$  factors):

$$\mathcal{L}_{\text{dSph},l} (\langle \sigma v \rangle; J'_l, \nu_l | \mathcal{D}_l) = \mathcal{L}_{\text{dSph},l} \left( \frac{J'_l}{J_{l,\text{obs}}} \langle \sigma v \rangle; J_{l,\text{obs}}, \nu_l | \mathcal{D}_l \right), \quad (7.13)$$

800   which is a straightforward rescaling operation that reduces the computational needs of the profiling  
 801   operation since:

$$\mathcal{L} (\langle \sigma v \rangle; \hat{\nu} | \mathcal{D}_{\text{dSphs}}) = \prod_{l=1}^{N_{\text{dSphs}}} \max_{J_l} \left[ \mathcal{L}_{\text{dSph},l} (\langle \sigma v \rangle; J_l, \hat{\nu}_l | \mathcal{D}_l) \times \mathcal{J}_l (J_l | J_{l,\text{obs}}, \sigma_{\log J_l}) \right]. \quad (7.14)$$

802   In addition, Eq. (7.13) enables the combination of data from different gamma-ray instruments and  
 803   observed dSphs via tabulated values of  $\mathcal{L}_{\text{dSph},l}$ , or equivalently of  $\lambda$  from Eq. (7.10) as was done in

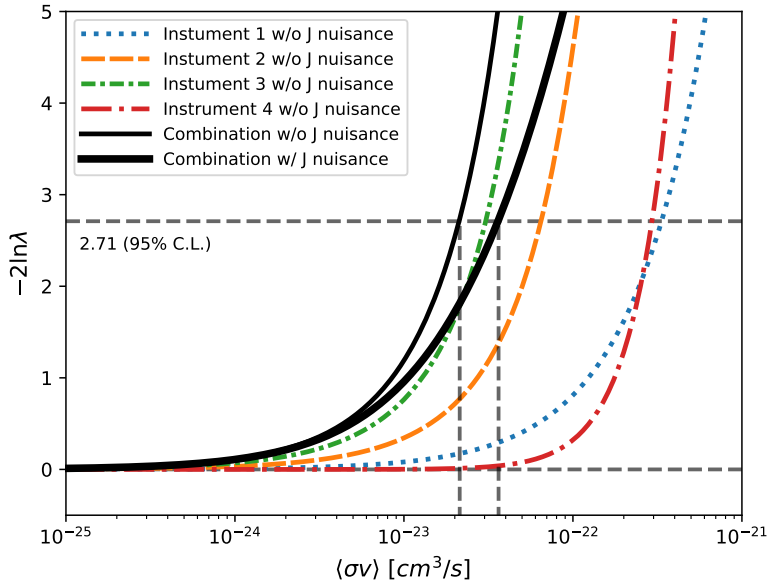


Figure 7.4 Illustration of the combination technique showing a comparison between  $-2 \ln \lambda$  provided by four instruments (colored lines) from the observation of the same dSph without any  $J$  nuisance and their sum, *i.e.* the resulting combined likelihood (thin black line). According to the test statistics of Equation (7.6), the intersection of the likelihood profiles with the line  $-2 \ln \lambda = 2.71$  indicates the 95% C.L. upper limit on  $\langle \sigma v \rangle$ . The combined likelihood (thin black line) shows a smaller value of upper limit on  $\langle \sigma v \rangle$  than those derived by individual instruments. We also show how the uncertainties on the  $J$  factor effects the combined likelihood and degrade the upper limit on  $\langle \sigma v \rangle$  (thick black line). All likelihood profiles are normalized so that the global minimum  $\widehat{\langle \sigma v \rangle}$  is 0. We note that each profile depends on the observational conditions in which a target object was observed. The sensitivity of a given instrument can be degraded and the upper limits less constraining if the observations are performed in non-optimal conditions such as a high zenith angle or a short exposure time.

804 this work, versus  $\langle \sigma v \rangle$ .  $\mathcal{L}_{\text{dSph},l}$  is computed for a fixed value of  $J_l$  and profiled with respect to all  
 805 instrumental nuisance parameters  $\nu_l$ , these nuisance parameters are discussed in more detail below.  
 806 These values are produced by each detector independently and therefore there is no need to share  
 807 sensitive low-level information used to produce them, such as event lists. Figure 7.4 illustrates the  
 808 multi-instrument combination technique used in this study with a comparison of the upper limit  
 809 on  $\langle \sigma v \rangle$  obtained from the combination of the observations of four experiments towards one dSph  
 810 versus the upper limit from individual instruments. It also shows graphically the effect of the  
 811  $J$ -factor uncertainty on the combined observations.

812 The *partial* joint likelihood function for gamma-ray observations of each dSph ( $\mathcal{L}_{\text{dSph},l}$ ) is

written as the product of the likelihood terms describing the  $N_{\text{exp},l}$  observations performed with any of our observatories:

$$\mathcal{L}_{\text{dSph},l} (\langle \sigma v \rangle; J_l, \nu_l | \mathcal{D}_l) = \prod_{k=1}^{N_{\text{exp},l}} \mathcal{L}_{lk} (\langle \sigma v \rangle; J_l, \nu_{lk} | \mathcal{D}_{lk}), \quad (7.15)$$

where each  $\mathcal{L}_{lk}$  term refers to an observation of the  $l$ -th dSph with associated  $k$ -th instrument responses.  $N_{\text{exp},l}$  varies from dSph to dSph and can be inferred from Table 7.2.

Each collaboration separately analyzes their data for  $\mathcal{D}_{lk}$  corresponding to dSph  $l$  and gamma-ray detector  $k$ , using as many common assumptions as possible in the analysis. HAWC's treatment was described earlier in Section 7.4.1 whereas the specifics of the remaining experiments is left to the publication. We compute the values for the likelihood functions  $\mathcal{L}_{lk}$  (see Eq. (7.15)) for a fixed value of  $J_l$  and profile over the rest of the nuisance parameters  $\nu_{lk}$ . Then, values of  $\lambda$  from Eq. (7.10) are computed as a function of  $\langle \sigma v \rangle$ , and shared using a common format. Results are computed for seven annihilation channels,  $W^+W^-$ ,  $ZZ$ ,  $b\bar{b}$ ,  $t\bar{t}$ ,  $e^+e^-$ ,  $\mu^+\mu^-$ , and  $\tau^+\tau^-$  over 62  $m_\chi$  values between 5 GeV and 100 TeV provided in [44]. The  $\langle \sigma v \rangle$  range is defined between  $10^{-28}$  and  $10^{-18} \text{cm}^3 \cdot \text{s}^{-1}$ , with 1001 logarithmically spaced values. The likelihood combination, i.e. Equation (7.11), and profile over the  $J$ -factor to compute the profile likelihood ratio  $\lambda$ , Equation (7.10), are carried out with two different public analysis software packages, namely `gLike` [50] and `LklCom` [51], that provide the same results [52].

As mentioned previously, each experiment computes the  $\mathcal{L}_{lk}$  from Equation (7.10) differently. The remainder of this section highlights the differences in this calculation across the experiments. Four experiments, namely *Fermi*-LAT, H.E.S.S., HAWC and MAGIC, use a binned likelihood to compute the  $\mathcal{L}_{lk}$ . For these experiments, for each observation  $\mathcal{D}_{lk}$  of a given dSph  $l$  carried out using a given gamma-ray detector  $k$ , the binned likelihood function is:

$$\mathcal{L}_{lk} (\langle \sigma v \rangle; J_l, \nu_{lk} | \mathcal{D}_{lk}) = \prod_{i=1}^{N_E} \prod_{j=1}^{N_P} \left[ \mathcal{P}(s_{lk,ij}(\langle \sigma v \rangle, J_l, \nu_{lk}) + b_{lk,ij}(\nu_{lk}) | N_{lk,ij}) \right] \times \mathcal{L}_{lk,\nu} (\nu_{lk} | \mathcal{D}_{\nu_{lk}}) \quad (7.16)$$

where  $N_E$  and  $N_P$  are the number of considered bins in reconstructed energy and arrival direction, respectively;  $\mathcal{P}$  represents a Poisson PDF for the number of gamma-ray candidate events  $N_{lk,ij}$

836 observed in the  $i$ -th bin in energy and  $j$ -th bin in arrival direction, when the expected number is  
 837 the sum of the expected mean number of signal events  $s_{ij}$  (produced by DM annihilation) and of  
 838 background events  $b_{ij}$ ;  $\mathcal{L}_{lk,\nu}$  is the likelihood term for the extra  $\nu_{lk}$  nuisance parameters that vary  
 839 from one instrument  $k$  to another. The expected counts for signal events  $s_{ij}$  for a given dSph  $l$  and  
 840 detector  $k$  is given by:

$$s_{ij}(\langle\sigma\nu\rangle, J) = \int_{E'_{\min,i}}^{E'_{\max,i}} dE' \int_{P'_{\min,j}}^{P'_{\max,j}} d\Omega' \int_0^\infty dE \int_{\Delta\Omega_{tot}} d\Omega \int_0^{T_{\text{obs}}} dt \frac{d^2\Phi(\langle\sigma\nu\rangle, J)}{dEd\Omega} \text{IRF}(E', P' | E, P, t) \quad (7.17)$$

841 where  $E'$  and  $E$  are the reconstructed and true energies,  $P'$  and  $P$  the reconstructed and true  
 842 arrival directions;  $E'_{\min,i}$ ,  $P'_{\min,j}$ ,  $E'_{\max,i}$ , and  $P'_{\max,j}$  are their lower and upper limits of the  $i$ -th  
 843 energy bin and the  $j$ -th arrival direction bin;  $T_{\text{obs}}$  is the (dead-time corrected) total observation  
 844 time;  $t$  is the time along the observations;  $d^2\Phi/dEd\Omega$  is the DM flux in the source region (see  
 845 Equation (7.1)); and  $\text{IRF}(E', P' | E, P, t)$  is the IRF, which can be factorized as the product of the  
 846 effective collection area of the detector  $A_{\text{eff}}(E, P, t)$ , the PDFs for the energy estimator  $f_E(E' | E, t)$ ,  
 847 and arrival direction  $f_P(P' | E, P, t)$  estimators. Note that for Fermi-LAT, HAWC, MAGIC, and  
 848 VERITAS the effect of the finite angular resolution is taken into account through the convolution  
 849 of  $d\Phi/dEd\Omega$  with  $f_P$  in Equation (7.17), whereas in the cases of H.E.S.S.  $f_P$  is approximated by a  
 850 delta function. This approximation has been made in order to maintain compatibility of the result  
 851 with what has been previously published. The difference introduced by this approximation is  $< 5\%$   
 852 for all considered dSphs. A more comprehensive review of the differences between the analyses of  
 853 different instruments can be found in [25].

## 854 7.5 HAWC Results

855 13 of the 20 dSphs considered for the Glory Duck analysis are within HAWC's field of view.  
 856 These dSph are analyzed for emission from DM annihilation according to the likelihood method  
 857 described in Section 7.4. The 13 likelihood profiles are then stacked to synthesize a combined  
 858 limit on the dark matter cross-section,  $\langle\sigma\nu\rangle$ . This combination is done for the 7 SM annihilation  
 859 channels used in the Glory Duck analysis. Figure 7.5 shows the combined limit for all annihilation  
 860 channels with HAWC only observations. We also perform 300 studies of Poisson trials on the

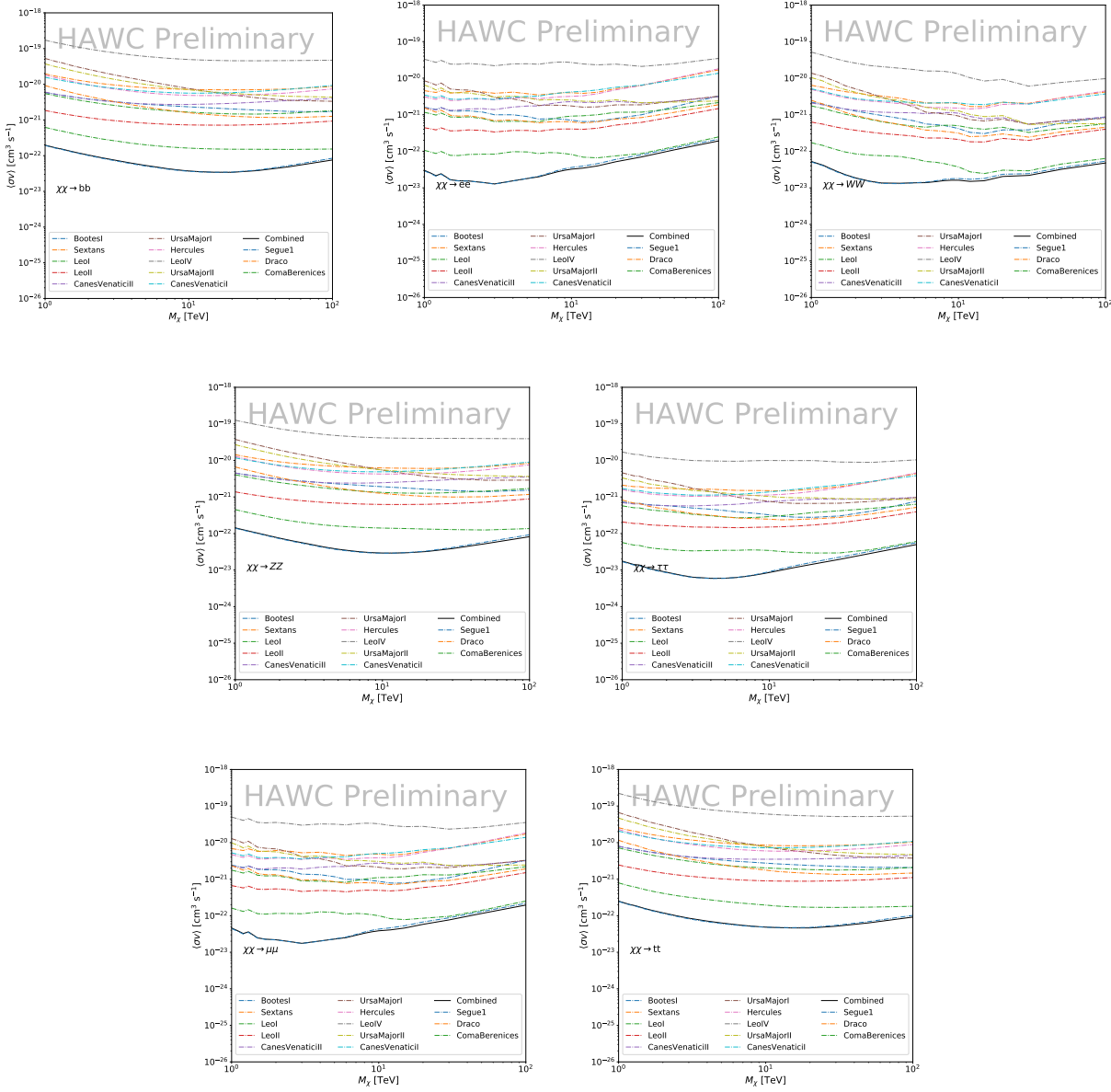


Figure 7.5 HAWC upper limits at 95% confidence level on  $\langle\sigma v\rangle$  versus DM mass for seven annihilation channels, using the set of  $J$ -factors from Ref. [53]. The solid line represents the observed combined limit. Dashed lines represent limits from individual dSphs.

background. These trials are used to produce HAWC Brazil bands which were shared with the other collaborators for combined Brazil Bands. The results on fitting to HAWC's Poisson trials of the DM hypothesis is shown in Figure 7.7 for all the DM annihilation channels studied for Glory Duck.

No DM was found in HAWC observations. HAWC's limits are dominated by the dSphs Segue1

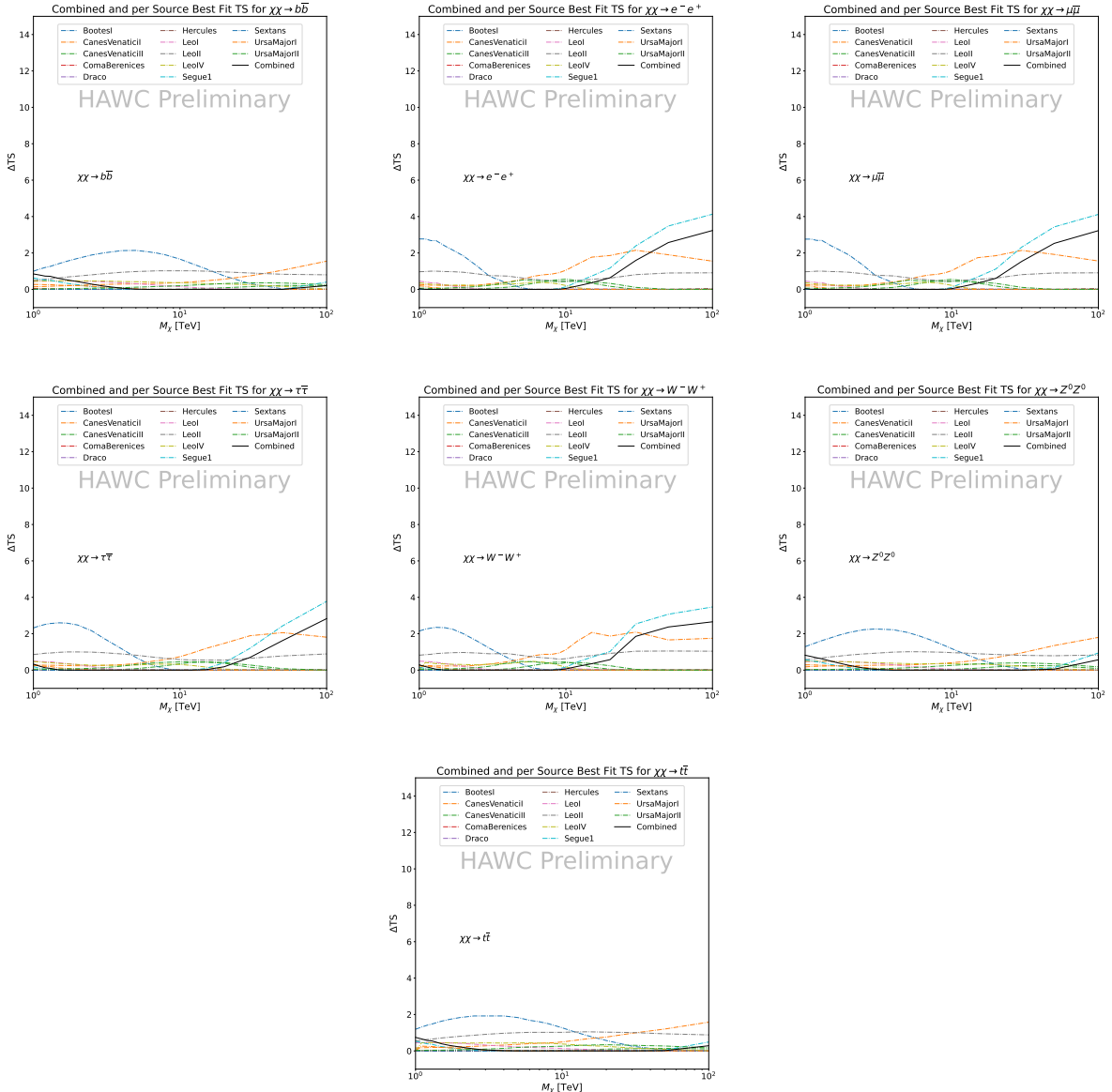


Figure 7.6 HAWC TS values for best fit  $\langle \sigma v \rangle$  versus  $m_\chi$  for seven SM annihilation channels with  $J$  factors from  $\mathcal{GS}$ . The solid black line shows the combined best fit TS values. The colored, dashed lines are the TS values for each of the 13 sources HAWC studied.

and Coma Berenices. The remaining 11 dSphs do not contribute significantly to the limit because they are at high zenith and/or have much smaller  $J$  factors. Even though some remaining dSphs have large  $J$  factors, they are towards the edge of HAWC's field of view where HAWC analysis is less sensitive.

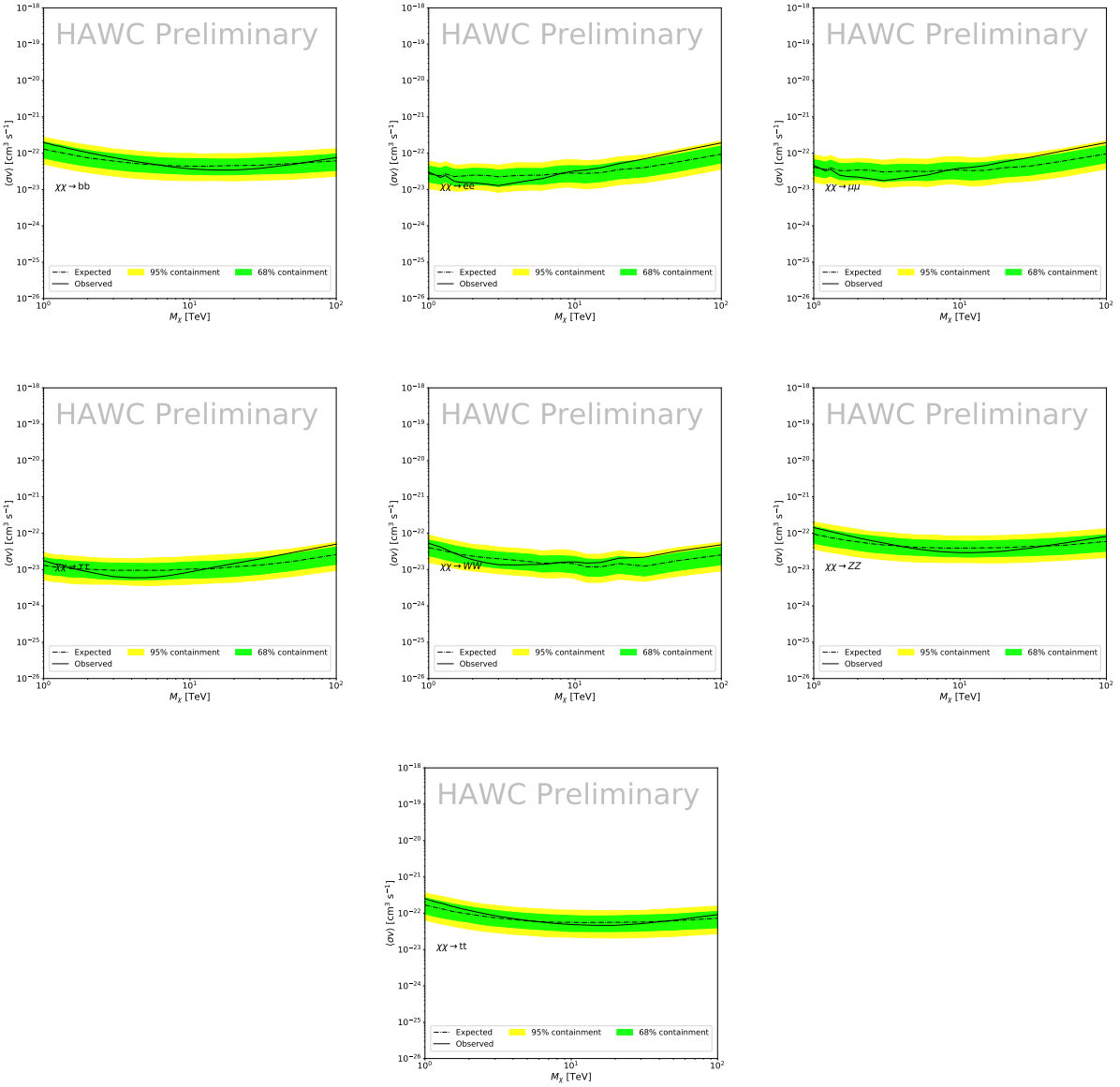


Figure 7.7 HAWC Brazil bands at 95% confidence level on  $\langle\sigma v\rangle$  versus DM mass for seven annihilation channels with  $J$ -factors from  $\mathcal{GS}$  [53]. The solid line represents the combined limit from 13 dSphs. The dashed line is the expected limit. The green band is the 68% containment. The yellow band is the 95% containment.

## 870 7.6 Glory Duck Combined Results

871 The crux of this analysis is that HAWC's results are combined with 4 other gamma-ray observa-  
 872 tories: Fermi-LAT, H.E.S.S., MAGIC, and VERITAS. No significant DM emission was observed  
 873 by any of the five instruments. We present the upper limits on  $\langle\sigma v\rangle$  assuming seven independent  
 874 DM self annihilation channels, namely  $W^+W^-$ ,  $Z^+Z^-$ ,  $b\bar{b}$ ,  $t\bar{t}$ ,  $e^+e^-$ ,  $\mu^+\mu^-$ , and  $\tau^+\tau^-$ . The 68%

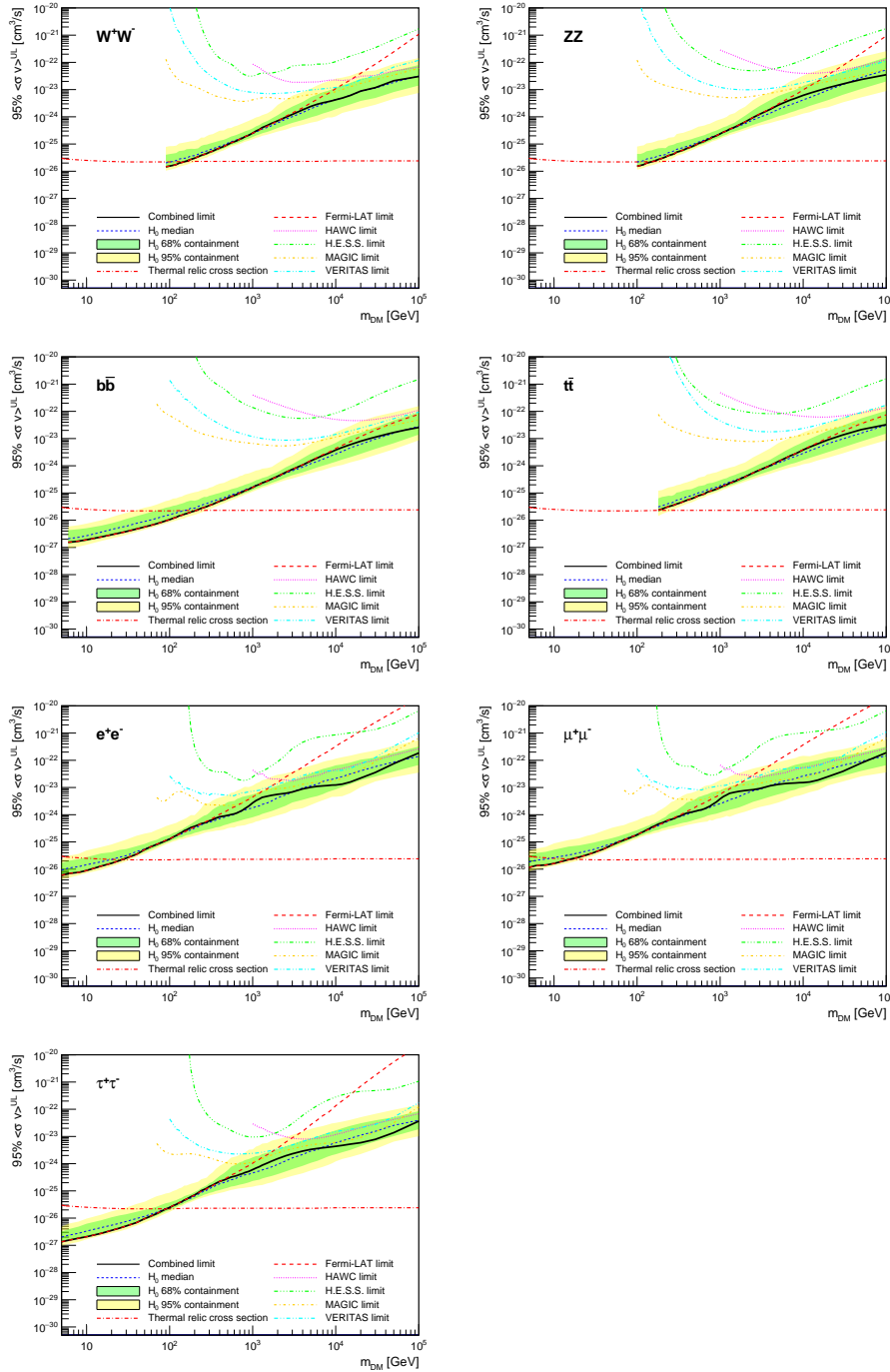


Figure 7.8 Upper limits at 95% confidence level on  $\langle\sigma v\rangle$  in function of the DM mass for eight annihilation channels, using the set of  $J$  factors from Ref. [53] ( $\mathcal{GS}$  set in Table 7.1). The black solid line represents the observed combined limit, the black dashed line is the median of the null hypothesis corresponding to the expected limit, while the green and yellow bands show the 68% and 95% containment bands. Combined upper limits for each individual detector are also indicated as solid, colored lines. The value of the thermal relic cross-section in function of the DM mass is given as the red dotted-dashed line [54].

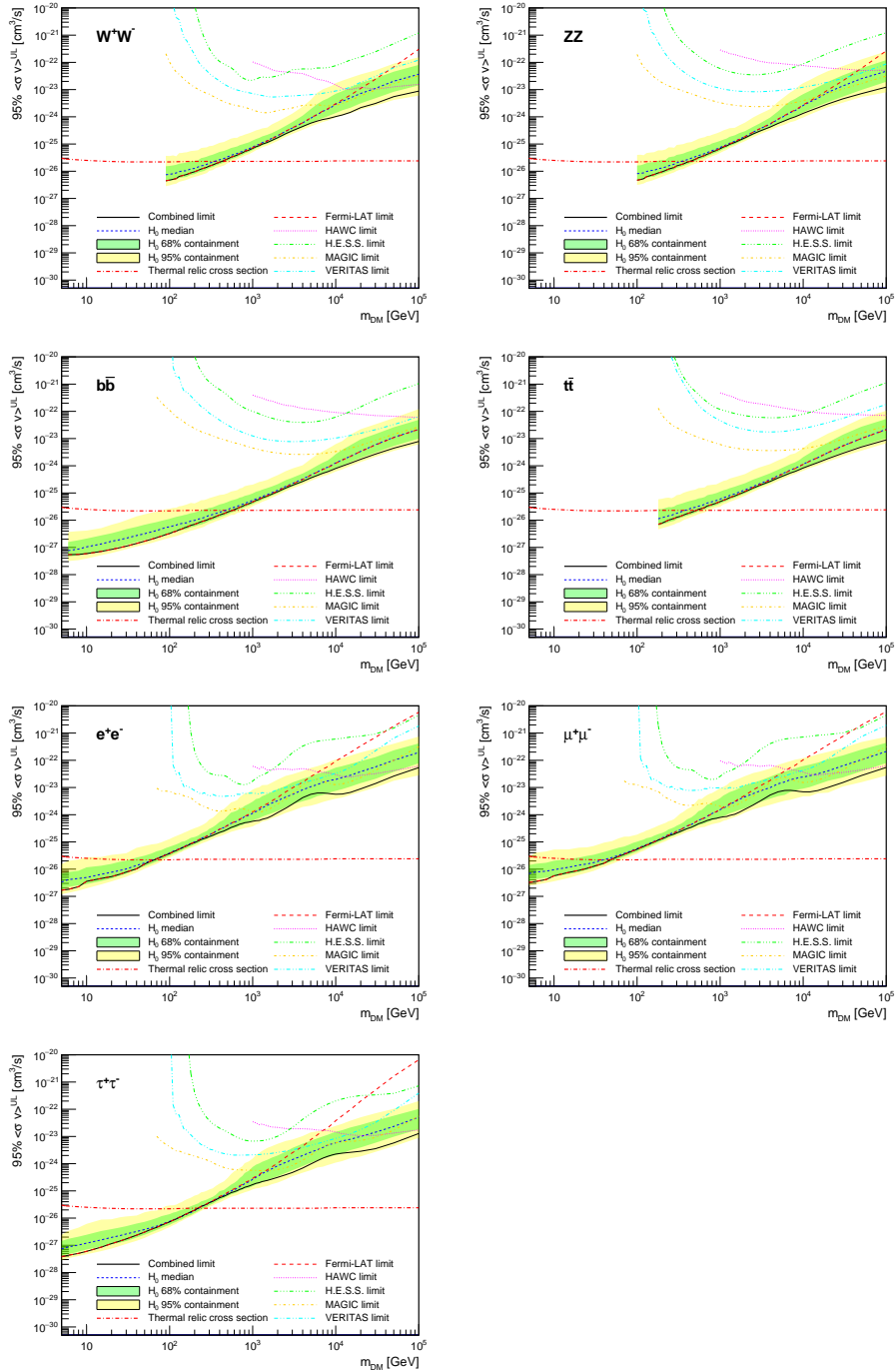


Figure 7.9 Same as Fig. 7.8, using the set of  $J$  factors from Ref. [47, 55] ( $\mathcal{B}$  set in Table 7.1).

and 95% containment bands are produced from 300 Poisson realizations of the null hypothesis corresponding to each of the combined datasets. These 300 realizations are combined identically to dSph observations. The containment bands and the median are extracted from the distribution of resulting limits on the null hypothesis. These 300 realizations are obtained either by fast simu-

879 lations of the OFF observations, for H.E.S.S., MAGIC, VERITAS, and HAWC, or taken from real  
880 observations of empty fields of view in the case of Fermi-LAT [48, 56, 57].

881 The obtained limits are shown in Figure 7.8 for the  $\mathcal{G}\mathcal{S}$  set of  $J$ -factors [53] and in Figure 7.9  
882 for the  $\mathcal{B}$  set of  $J$ -factors [47, 55]. The combined limits are presented with their 68% and 95%  
883 containment bands, and are expected to be close to the median limit when no signal is present.  
884 We observe agreement with the null hypothesis for all channels, within  $2\sigma$  standard deviations,  
885 between the observed limits and the expectations given by the median limits. Limits obtained from  
886 each detector are also indicated in the figures, where limits for all dSphs observed by the specific  
887 instrument have been combined.

888 Below  $\sim 300$  GeV, the *Fermi*-LAT dominates the DM limits for all annihilation channels. From  
889  $\sim 300$  GeV to  $\sim 2$  TeV, *Fermi*-LAT continues to dominate for the hadronic and bosonic DM channels,  
890 yet the IACTs (H.E.S.S., MAGIC, and VERITAS) and *Fermi*-LAT all contribute to the limit for  
891 leptonic DM channels. For DM masses between  $\sim 2$  TeV to  $\sim 10$  TeV, the IACTs dominate leptonic  
892 DM annihilation channels, whereas both the *Fermi*-LAT and the IACTs dominate bosonic and  
893 hadronic DM annihilation channels. From  $\sim 10$  TeV to  $\sim 100$  TeV, both the IACTs and HAWC  
894 contribute significantly to the leptonic DM limit. For hadronic and bosonic DM, the IACTs and  
895 *Fermi*-LAT both contribute strongly.

896 We notice that the limits computed using the  $\mathcal{B}$  set of  $J$ -factor are always better compared to the  
897 ones calculated with the  $\mathcal{G}\mathcal{S}$  set. For the  $W^+W^-$ ,  $Z^+Z^-$ ,  $b\bar{b}$ , and  $t\bar{t}$  channels, the ratio between the  
898 limits computed with the two sets of  $J$ -factor is varying between a factor of  $\sim 3$  and  $\sim 5$  depending  
899 on the energy, with the largest ratio around 10 TeV. For the channels  $e^+e^-$ ,  $\mu^+\mu^-$ , and  $\tau^+\tau^-$ , the  
900 ratio lies between  $\sim 2$  to  $\sim 6$ , being maximum around 1 TeV. Examining Figure 7.16 and Figure 7.17  
901 in Section 7.8, these differences are explained by the fact that the  $\mathcal{B}$  set provides higher  $J$ -factors  
902 for the majority of the studied dSphs, with the notable exception of Segue I. The variation on the  
903 ratio of the limits for the two sets is due to different dSph dominating the limits depending on the  
904 energy. This pushes the range of thermal cross-section which can be excluded to higher mass. This  
905 comparison demonstrates the magnitude of systematic uncertainties associated with the choice of

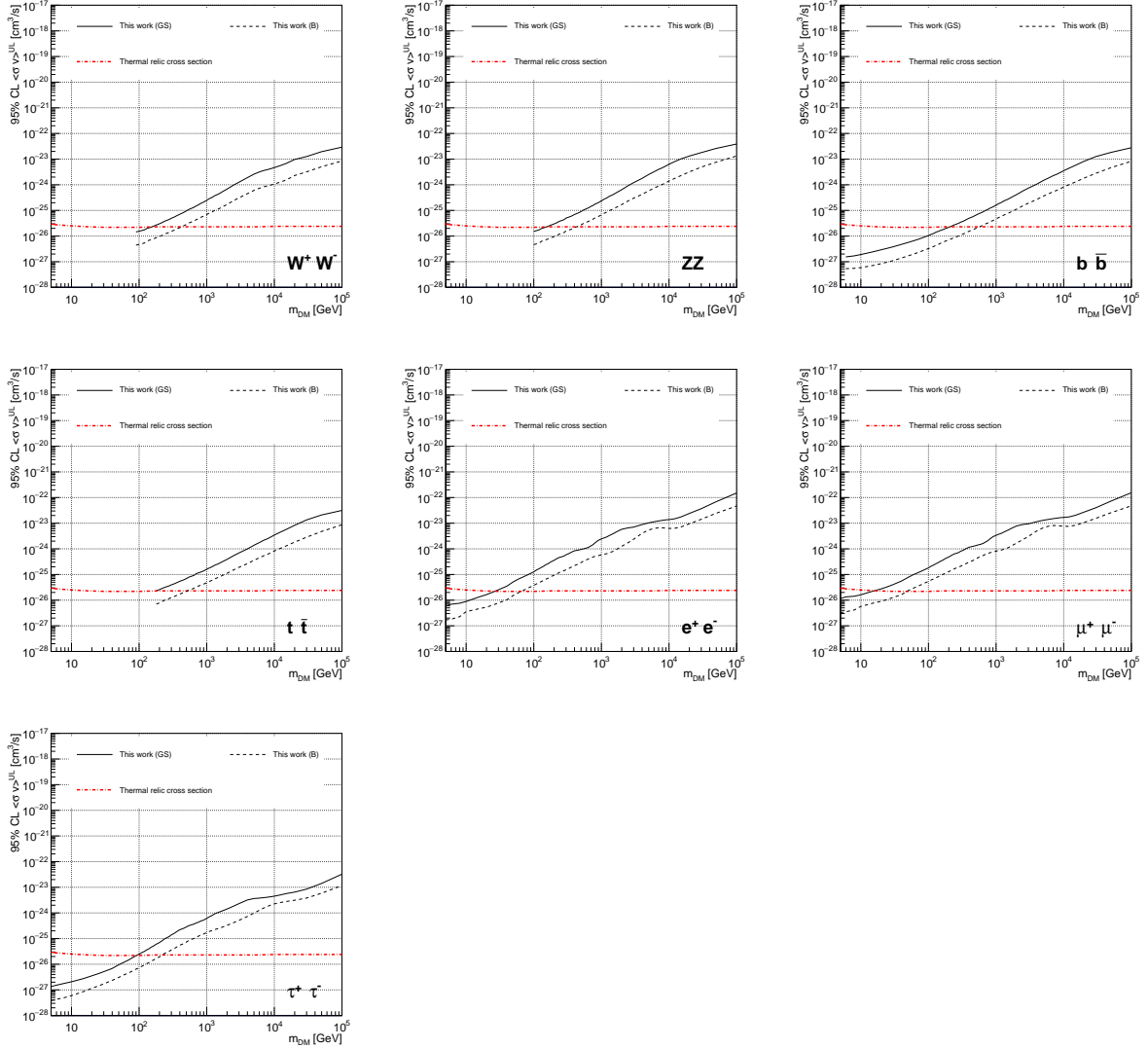


Figure 7.10 Comparisons of the combined limits at 95% confidence level for each of the eight annihilation channels when using the  $J$  factors from Ref. [53] ( $\mathcal{GS}$  set in Table 7.1), plain lines, and the  $J$  factor from Ref. [47, 55] ( $\mathcal{B}$  set in Table 7.1), dashed lines. The cross-section given by the thermal relic is also indicated [54].

## 906 the $J$ -factor

907 This comparison demonstrates the magnitude of systematic uncertainties associated with the  
 908 choice of the  $J$ -factor calculation. The  $\mathcal{GS}$  and  $\mathcal{B}$  sets present a difference in the limits for all  
 909 channels of about This difference is explained, see Figure 7.16 and Figure 7.17 in Appendix, by the  
 910 fact that the  $\mathcal{B}$  set provides higher  $J$  factors for all dSph except for Segue I. This pushes the range  
 911 of thermal cross-section which can be excluded to higher mass.

912 **7.7 HAWC Systematics**

913 **7.7.1 Inverse Compton Scattering**

914       The DM-DM annihilation channels produce many high energy electrons regardless of the  
915   primary annihilation channel. These high energy electrons can produce high energy gamma-rays  
916   through Inverse Compton Scattering (ICS). If this effect is strong, it would change the morphology  
917   of the source and increase the total expected gamma-ray counts from any source. The PPPC [44]  
918   provides tools in Mathematica for calculating the impact of ICS for an arbitrary location in the  
919   sky for a specified annihilation channel. We calculated the change in gamma-ray counts for DM  
920   annihilation to primary  $e\bar{e}$  for RA and Dec corresponding to Segue1 and Coma Berenices. These  
921   dSphs were chosen because they are the strongest contributors to the limit.  $e\bar{e}$  was selected because  
922   it would have the largest number of high energy electrons. The effect was found to be on the order  
923   of  $10^{-7}$  on the gamma-ray spectrum. As a result, this systematic is not considered in our analysis.

924 **7.7.2 Point Source Versus Extended Source Limits**

925       The previous DM search toward dSph approximated the dSphs as point sources [46]. In  
926   this analysis, the dSphs are implemented as extended with J-factor distributions following those  
927   produced by [53]. The resolution of the cited map is much finer than HAWC's angular resolution.  
928   The vast majority of the J-factor distribution is represented on the central HAWC pixel of the dSph  
929   spatial map. However, the neighboring 8 pixels are not negligible and contribute to our limit.

930       Figure 7.11 shows a substantial improvement to the limit for Segue1. Fig. 7.12 however showed  
931   identical limits. These disparities are best explained by the relative difference in their J-Factors.  
932   Both dSphs pass almost overhead the HAWC detector, however Segue1 has the larger J-Factor  
933   between the two. Adjacent pixels to the central pixel will therefore contribute to the limits. This is  
934   the case for other dSph that are closer to overhead the HAWC detector.

935       Comparison plots for all sources and the combined limit can be found in the sandbox for the  
936   Glory Duck project.

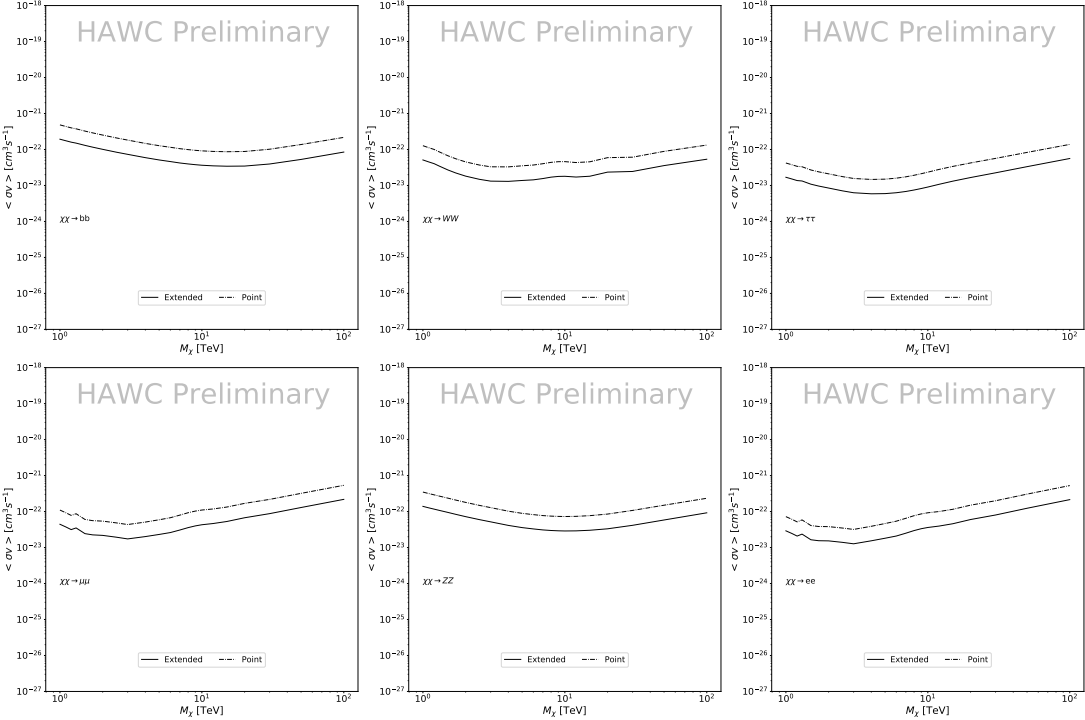


Figure 7.11 Comparisons of the combined limits at 95% confidence level for a point source analysis and extended source using [53]  $\mathcal{GS}$  J-factor distributions and PPPC [44] annihilation spectra. Shown are the limits for Segue1 which will have the most significant impact on the combined limit. 6 of the 7 DM annihilation channels are shown. Solid lines are extended source studies. Dashed lines are point source studies. Overall, the extended source analysis improves the limit by a factor of 2.

### 937 7.7.3 Impact of Pointing Systematic

938 During the analysis it was discovered that reconstruction of gamma-rays. Slides describing this  
 939 systematic can be found [here](#). Shown on the presentation is dependence on the pointing systematic  
 940 on declination. New spatial profiles were generated for every dSph and limits were computed for  
 941 the adjusted declination.

942 Section 7.7.3 demonstrates the impact of this systematic for all DM annihilation channels  
 943 studied by HAWC. The impact is a tiny improvement, yet mostly identical, to the combined limits.

## 944 7.8 J-factor distributions

### 945 7.8.1 Numerical integration of $\mathcal{GS}$ maps

946 It was discovered well after the HAWC analysis was completed that the published tables from  
 947  $\mathcal{GS}$  [45] quoted median J-factors were computed in a non-trivial manner. The assumption myself

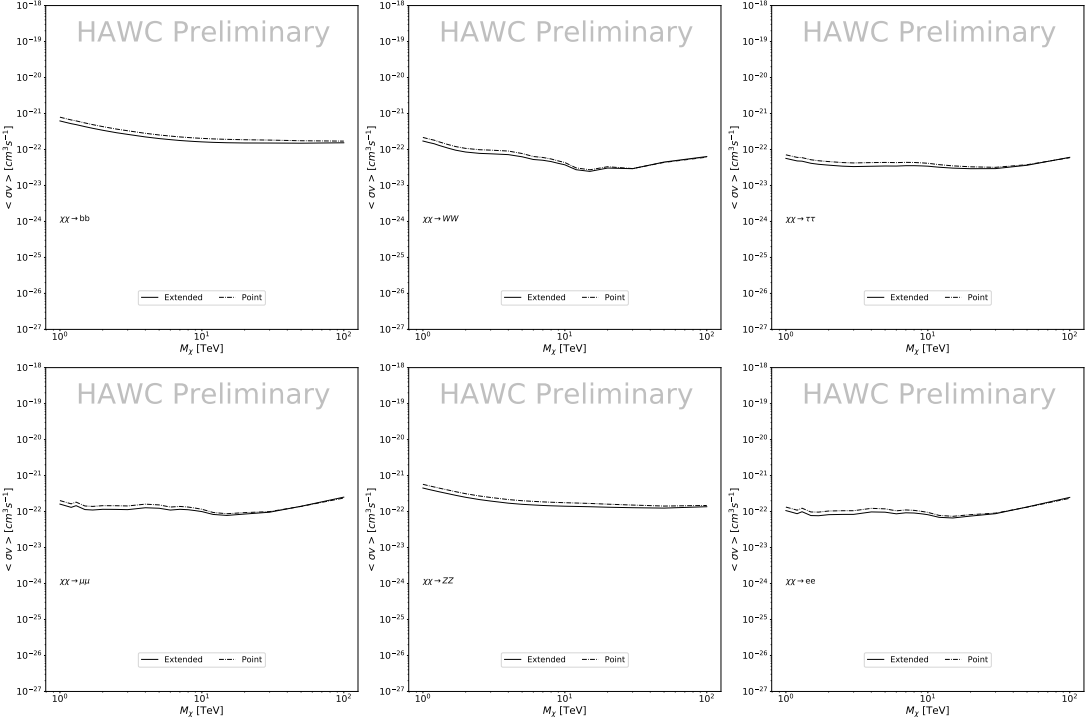


Figure 7.12 Same as Fig. 7.11 on Coma Berenices. This dSph also contributes significantly to the limit. The limits are identical in this case.

and collaborators had been that the published tables represented the  $J$ -factor as a function of  $\theta$  for the best global fit model on a per-source basis. However, this is not the case. Instead, what is published are the best fit model for each dwarf that only considers stars up to the angular separation  $\theta$ . Therefore, the model is changing for each value of  $\theta$  for each dwarf. Yet, the introduced features from unique models at each  $\theta$  are much smaller than the angular resolution of HAWC. It is not expected for these effects to impact the limits and TS greatly as a result.

Median  $J$ -factor model profiles were provided by the authors. New maps were generated and analyzed for Segue1 and Coma Berenices. Figure 7.14 shows the differential between maps generated with the method from Section 7.8.1 and from the authors of [45]. These maps were reanalyzed for all SM DM annihilation channels. Upper limits for these channels are shown in Figure 7.15

From Figure 7.15, we can see that the impact of these model difference was no substantial. The observed impact was a fractional effect which is much smaller than the impact from selecting another DM spatial distribution model as was shown in Figure 7.10.

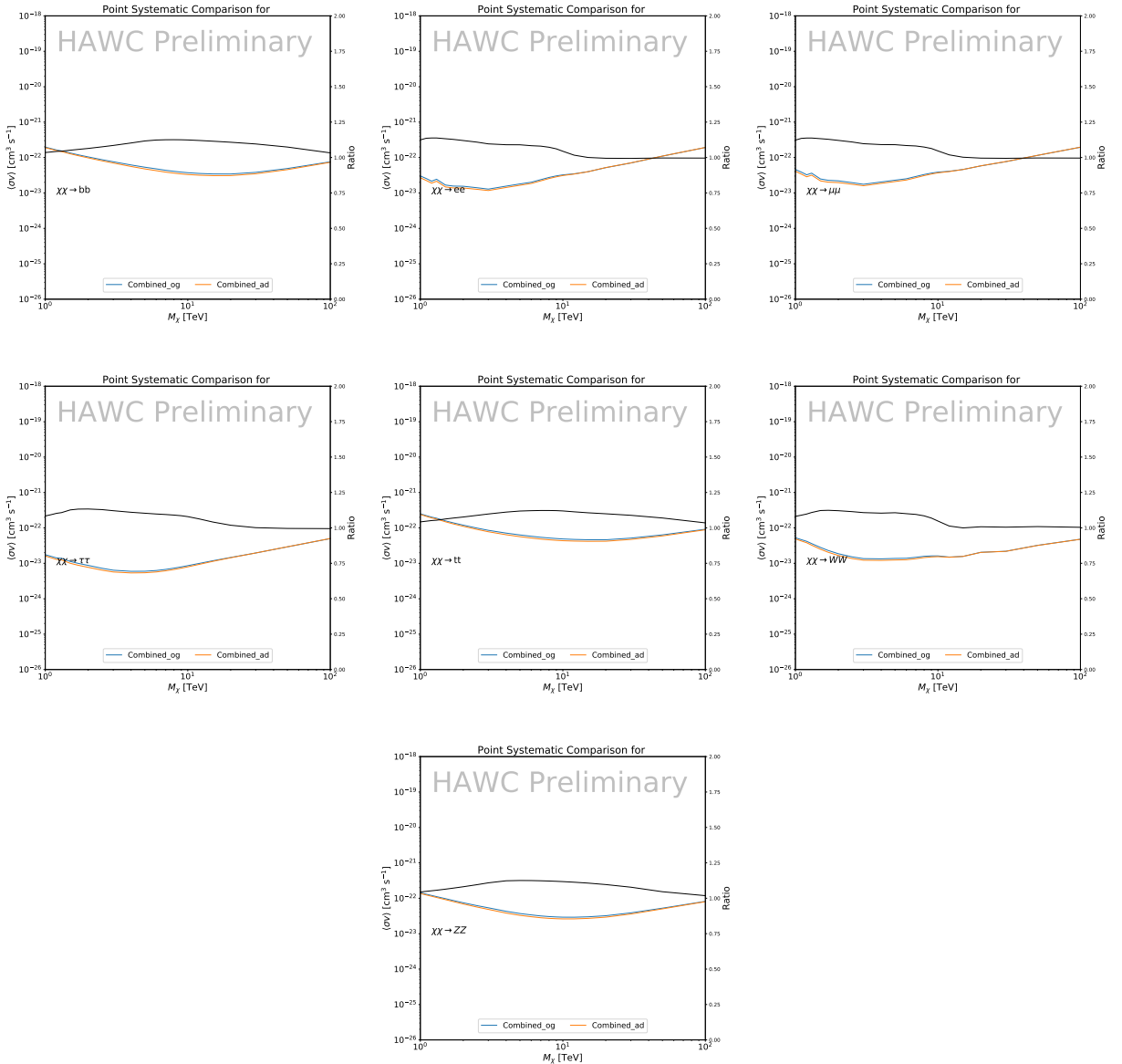


Figure 7.13 Comparison of combined limits when correcting for HAWC’s pointing systematic. All DM annihilation channels are shown. The solid black line is the ratio between published limit to the declination corrected limit. The blue solid line or “Combined\_og” represented the limits computed for Glory Duck. The solid orange line or “Combined\_ad” represented the limits computed after correcting for the pointing systematic.

## 962 7.8.2 $\mathcal{G}\mathcal{S}$ Versus $\mathcal{B}$ spatial models

963 We show in this appendix a comparison between the  $J$ -factors computed by Geringer-Sameth  
 964 *et al.* [53] (the  $\mathcal{G}\mathcal{S}$  set) and the ones computed by Bonnivard *et al.* [47, 55] (the  $\mathcal{B}$  set). The  
 965  $\mathcal{G}\mathcal{S}$   $J$ -factors are computed through a Jeans analysis of the kinematic stellar data of the selected

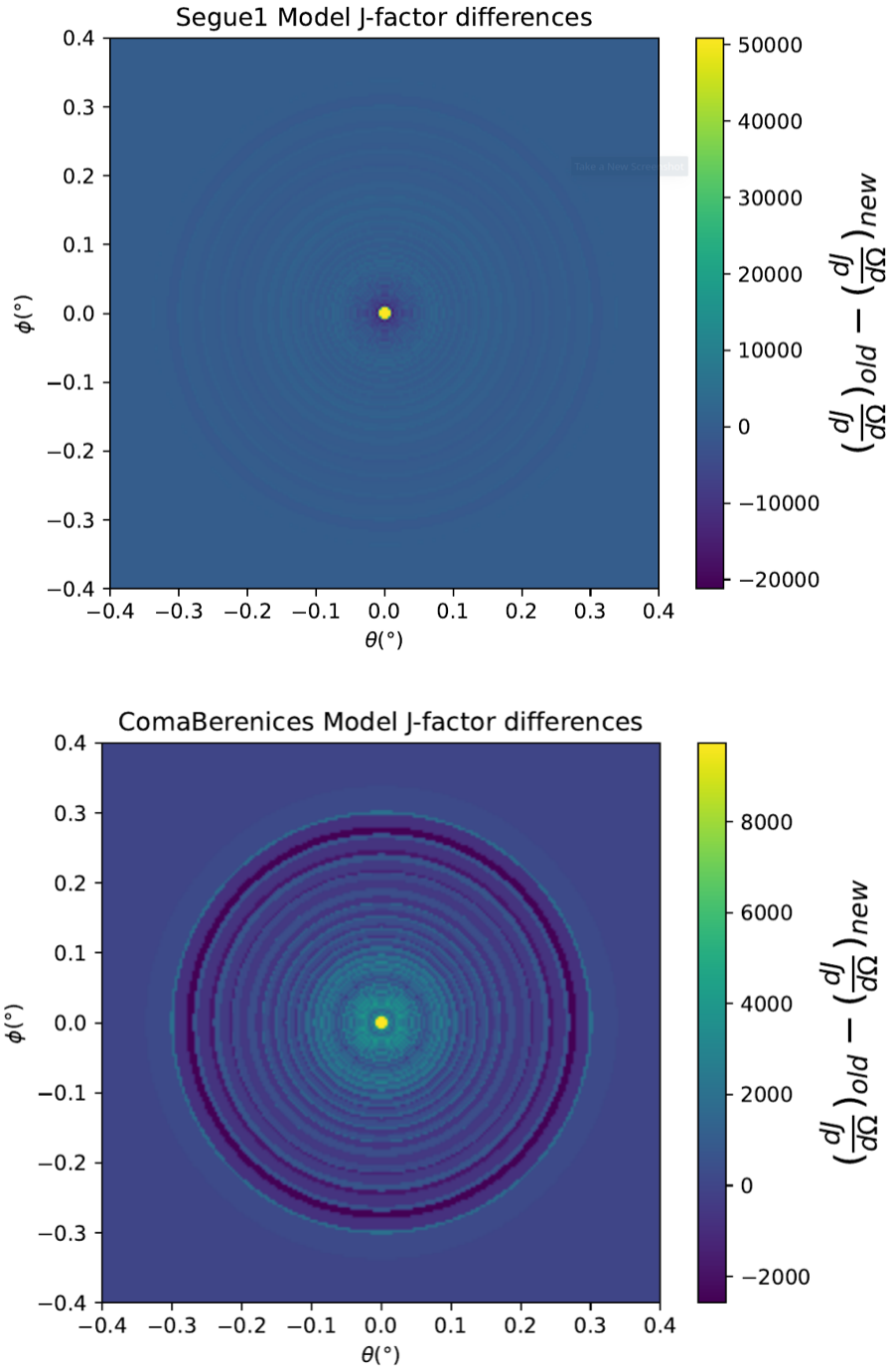


Figure 7.14 Differential map of  $dJ/\Omega$  from model built in Section 7.8.1 and profiles provided directly from authors. (Top) Differential from Segue1. (bottom) Differential from Coma Berenices. Note that their scales are not the same. Segue1 shows the deepest discrepancies which is congruent with its large uncertainties. Both models show anuli where unique models become apparent.

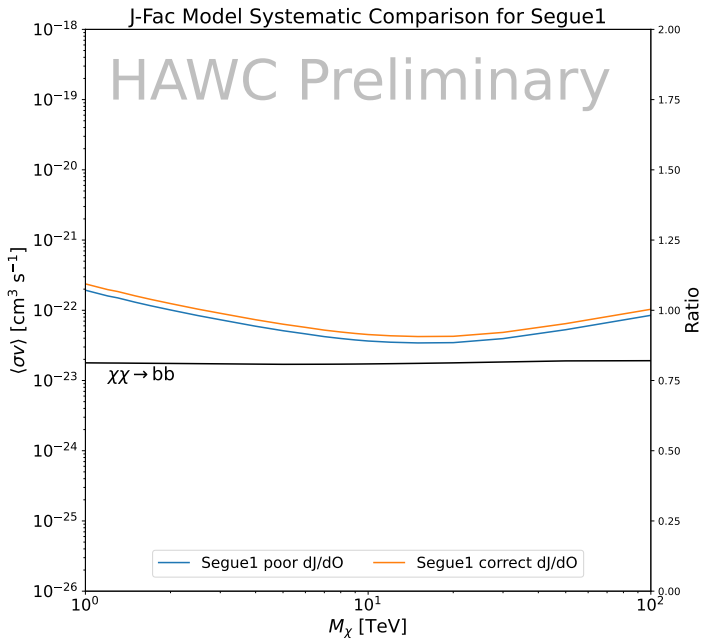
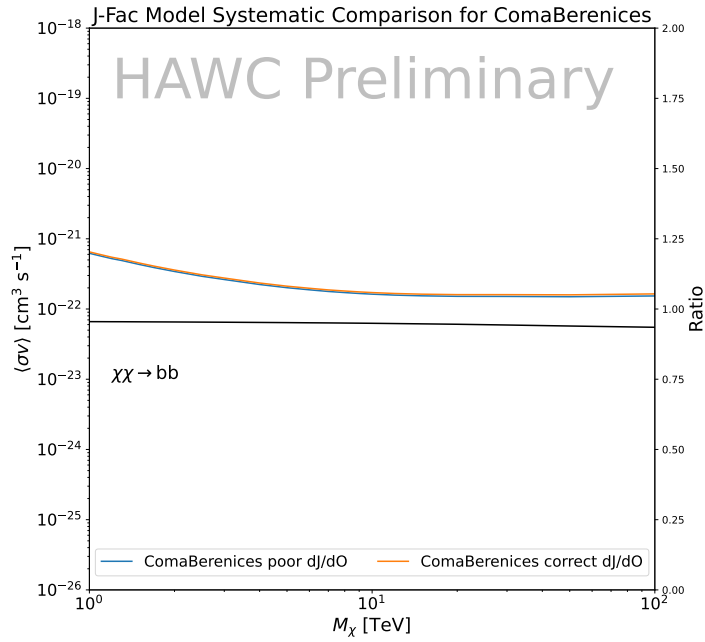


Figure 7.15 HAWC limits for Coma Berenices (top) and Segue1 (bottom) for two different map sets. Blue lines are limits calculated on maps with poor model representation. Orange lines are limits calculated on spatial profiles provided by the authors of [45]. Black line is the ratio of the poor spatial model limits to the corrected spatial models. The left y-axis measures  $\langle \sigma v \rangle$  for the blue and orange lines. The right y-axis measures the ratio and is unitless.

966 dSphs, assuming a dynamic equilibrium and a spherical symmetry for the dSphs. They adopted  
967 the generalized DM density distribution, known as Zhao-Hernquist, introduced by [58], carrying  
968 three additional index parameters to describe the inner and outer slopes, and the break of the  
969 density profile. Such a profile parametrization allows the reduction of the theoretical bias from  
970 the choice of a specific radial dependency on the kinematic data. In other words, the increase of  
971 free parameters with the use of the Zhao-Hernquist profile allows a better description of the mass  
972 density distribution of dark matter.

973 In addition, a constant velocity anisotropy profile and a Plummer light profile [59] for the stellar  
974 distribution were assumed. The velocity anisotropy profile depends on the radial and tangential  
975 velocity dispersion. However, its determination remains challenging since only the line-of-sight  
976 velocity dispersion can be derived from velocity measurements. Therefore, the parametrization of  
977 the anisotropy profile is obtained from simulated halos (see [60] for more details). They provide the  
978 values of the  $J$ -factors of regions extending to various angular radius up to the outermost member  
979 star.

980 The  $\mathcal{B}$   $J$ -factors were computed through a Jeans analysis taking into account the systematic  
981 uncertainties induced by the DM profile parametrization, the radial velocity anisotropy profile, and  
982 the triaxiality of the halo of the dwarf galaxies. They performed a more complete study of the dSph  
983 kinematics and dynamics than  $\mathcal{GS}$  for the determination of the  $J$ -factor. Conservative values of the  
984  $J$ -factors where obtained using an Einasto DM density profile [61], a realistic anisotropy profile  
985 known as the Baes & Van Hese profile [62] which takes into account that the inner regions can be  
986 significantly non-isotropic, and a Zhao-Hernquist light profile [58].

987 For both sets,  $J$ -factor values are provided for all dSphs as a function of the radius of the  
988 integration region [53, 47, 55]. Table 7.1 shows the heliocentric distance and Galactic coordinates  
989 of the twenty dSphs, together with the two sets of  $J$ -factor values integrated up to the outermost  
990 observed star for  $\mathcal{GS}$  and the tidal radius for  $\mathcal{B}$ . Both  $J$ -factor sets were derived through a Jeans  
991 analysis based on the same kinematic data, except for Draco where the measurements of [63] have  
992 been adopted in the computation of the  $\mathcal{B}$  value. The computations for producing the  $\mathcal{GS}$  and  $\mathcal{B}$

993 samples differ in the choice of the DM density, velocity anisotropy, and light profiles, for which the  
994 set  $\mathcal{B}$  takes into account some sources of systematic uncertainties.

995 Figure 7.16 and Figure 7.17 show the comparisons for the  $J$ -factor versus the angular radius  
996 for each of the 20 dSphs used in this study. The uncertainties provided by the authors are also  
997 indicated in the figures. For the  $\mathcal{GS}$  set, the computation stops at the angular radius corresponding  
998 to the outermost observed star, while for the  $\mathcal{B}$  set, the computation stops at the angular radius  
999 corresponding to the tidal radius.

1000 **7.9 Discussion and Conclusions**

1001 In this multi-instrument analysis, we have used observations of 20 dSphs from the gamma-ray  
1002 telescopes Fermi-LAT, H.E.S.S., MAGIC, VERITAS, and HAWC to perform a collective DM  
1003 search annihilation signals. The data were combined across sources and detectors to significantly  
1004 increase the sensitivity of the search. We have observed no significant deviation from the null, no  
1005 DM, hypothesis, and so present our results in terms of upper limits on the annihilation cross-section  
1006 for seven potential DM annihilation channels.

1007 Fermi-LAT brings the most stringent constraints for continuum channels below approximately  
1008 1 TeV. The remaining detectors dominate at higher energies. Overall, for multi-TeV DM mass,  
1009 the combined DM constraints from all five telescopes are 2-3 times stronger than any individual  
1010 telescope for multi-TeV DM.

1011 Derived from observations of many dSphs, our results produce robust limits given the DM  
1012 content of the dSphs is relatively well constrained. The obtained limits span the largest mass  
1013 range of any WIMP DM search. Our combined analysis improves the sensitivity over previously  
1014 published results from each detector which produces the most stringent limits on DM annihilation  
1015 from dSphs. These results are based on deep exposures of the most promising known dSphs with  
1016 the currently most sensitive gamma-ray instruments. Therefore, our results constitute a legacy of  
1017 a generation of gamma-ray instruments on WIMP DM searches towards dSphs. Our results will  
1018 remain the reference in the field until a new generation of more sensitive gamma-ray instruments  
1019 begin operations, or until new dSphs with higher  $J$ -factors are discovered.

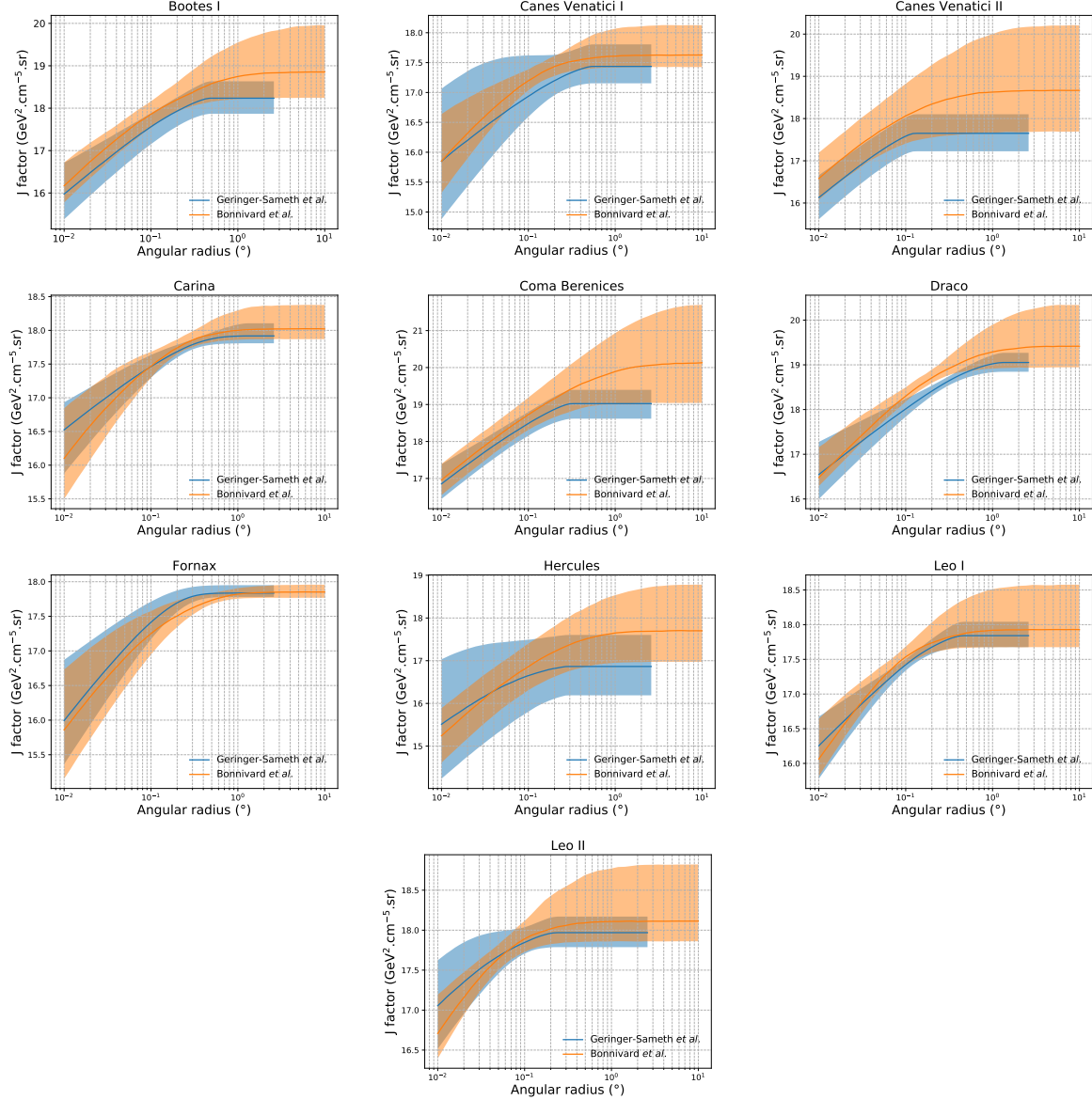


Figure 7.16 Comparisons between the  $J$ -factors versus the angular radius for the computation of  $J$  factors from Ref. [53] ( $\mathcal{GS}$  set in Table 7.1) in blue and for the computation from Ref. [47, 55] ( $\mathcal{B}$  set in Tab. 7.1) in orange. The solid lines represent the central value of the  $J$ -factors while the shaded regions correspond to the  $1\sigma$  standard deviation.

This analysis serves as a proof of concept for future multi-instrument and multi-messenger combination analyses. With this collaborative effort, we have managed to sample over four orders in magnitude in gamma-ray energies with distinct observational techniques. Determining the nature of DM continues to be an elusive and difficult problem. Larger datasets with diverse measurement techniques could be essential to tackling the DM problem. A future collaboration using similar

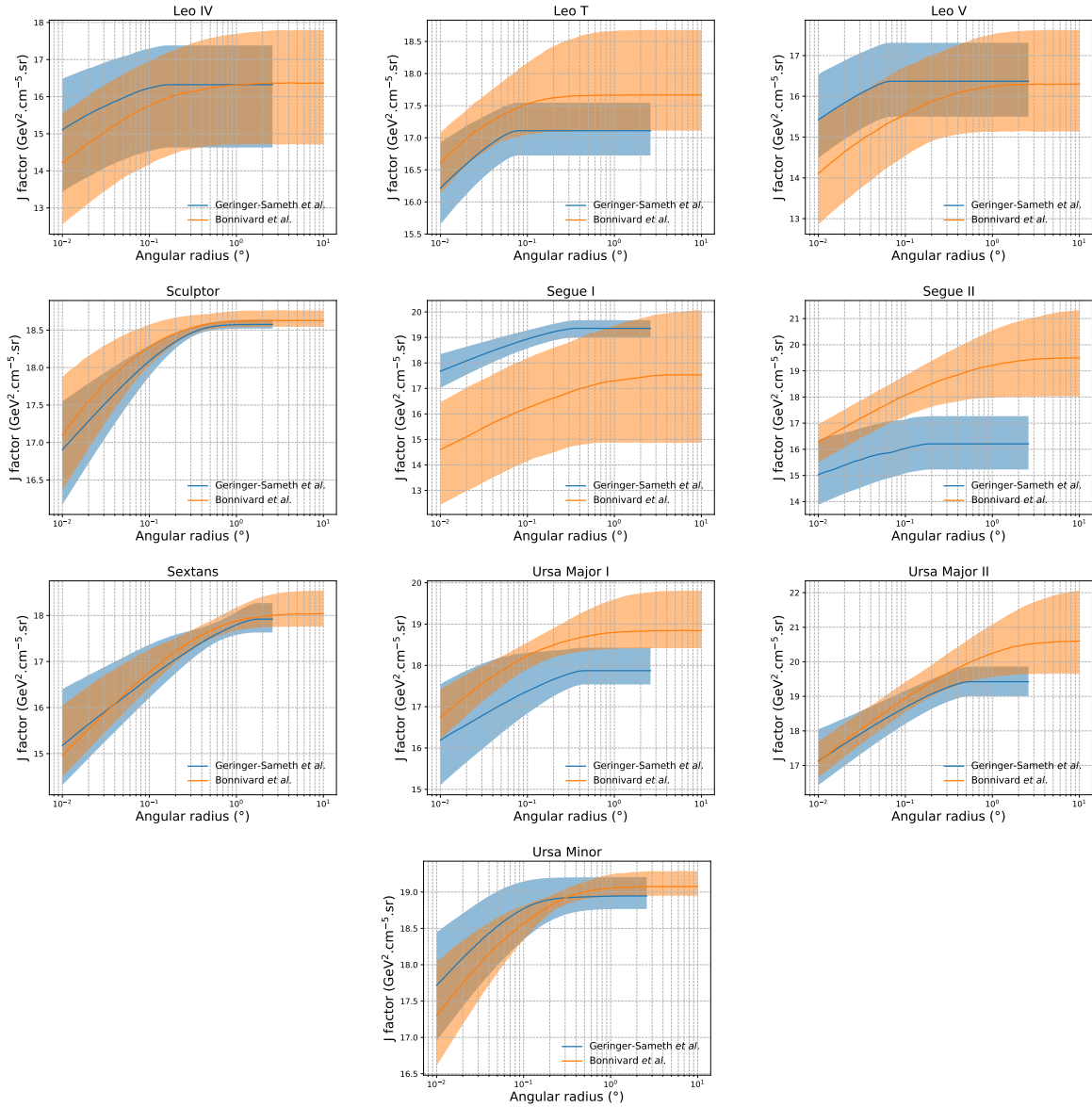


Figure 7.17 Comparisons between the  $J$ -factors versus the angular radius for the computation of  $J$  factors from Ref. [53] ( $\mathcal{GS}$  set in Tab. 7.1) in blue and for the computation from Ref. [47, 55] ( $\mathcal{B}$  set in Tab. 7.1) in orange. The solid lines represent the central value of the  $J$ -factors while the shaded regions correspond to the  $1\sigma$  standard deviation.

1025 techniques as the ones described in this paper could grow even beyond gamma rays. The models we  
 1026 used for this study include annihilation channels with neutrinos in the final state. Advanced studies  
 1027 could aim to merge our results with those from neutrino observatories with large data sets. Efforts  
 1028 are already underway to add data from the IceCube, ANTARES, and KM3NeT observatories to  
 1029 these gamma-ray results.

1030 From this work, a selection of the best candidates for observations, according to the latest  
1031 knowledge on stellar dynamics and modelling techniques for the derivation of the  $J$ -factors on  
1032 the potential dSphs targets, is highly desirable at the time that new experiments are starting their  
1033 dark matter programs using dSphs. Given the systematic uncertainty inherent to the derivation of  
1034 the  $J$ -factors, an informed observational strategy would be to select both objects with the highest  
1035  $J$ -factors that could lead to DM signal detection, and objects with robust  $J$ -factor predictions, i.e.  
1036 with kinematic measurements on many bright stars, which would strengthen the DM interpretation  
1037 reliability of the observation outcome.

1038 This analysis combines data from multiple telescopes to produce strong constraints on astro-  
1039 physical objects. From this perspective, these methods can be applied beyond just DM searches.  
1040 Almost every astrophysical study can benefit from multi-telescope, multi-wavelength gamma-ray  
1041 studies. We have enabled these telescopes to study the cosmos with greater precision and detail.  
1042 Many astrophysical searches can benefit from multi-instrument gamma-ray studies, for which our  
1043 analysis lays the foundation.

## CHAPTER 8

### 1044 MULTITHREADING HAWC ANALYSES FOR DARK MATTER SEARCHES

#### 1045 8.1 Introduction

1046 HAWC’s current software suite, plugins to 3ML, does not fully utilize computational advancements of recent decades. Said advancements include the proliferation of Graphical Processing  
1047 Units (GPUs), and multithreading on multi-core processors. The analysis described in chapter 7  
1048 took up to 3 months of human time waiting for the full gambit of data analysis and simulation  
1049 of background to run. Additionally, with the addition of a 2D binning scheme,  $f_{\text{hit}}$  and NN, the  
1050 expected compute time is expected to grow further. Although excessive computing time was, in  
1051 part, from an intense use of a shared computing cluster, it was evident that there was room for  
1052 improvement. In HAWC’s next generation dSph DM search, I decided to develop codes that would  
1053 utilize the multi-core processors on modern high performance computing clusters. The results of  
1054 this work are featured in this chapter and brought a human timing improvement to computation that  
1055 scales as  $1/N$  where  $N$  is the number of threads.

#### 1057 8.2 Dataset and Background

1058 This section enumerates the data and background methods used for HAWC’s multi-threaded  
1059 study of dSphs. Section 8.2.1 and Section 8.2.2 are most useful for fellow HAWC collaborators  
1060 looking to replicate a multithreaded dSph DM search.

##### 1061 8.2.1 Itemized HAWC files

- 1062 • Detector Resolution: `refit-Pass5-Final-NN-detRes-zenith-dependent.root`
- 1063 • Data Map: `Pass5-Final-NN-maptree-ch103-ch1349-zenith-dependent.root`
- 1064 • Spectral Dictionary: `HDMspectra_dict_gamma.npy`

##### 1065 8.2.2 Software Tools and Development

1066 This analysis was performed using HAL and 3ML [42, 43] in Python version 3. I built software  
1067 in collaboration with Michael Martin and Letrell Harris to implement the *Dark Matter Spectra from*

1068 *the Electroweak to the Planck Scale* (HDM) [64] and dSphs spatial model from [65] for HAWC  
1069 analysis. A NumPy dictionary of HDM was made for Py3. The corresponding Python3 file is  
1070 `HDMspectra_dict_gamma.npy`. These files can also be used for decay channels and tools are  
1071 provided in HDM’s [git repository](#) [64]. The analysis was performed using the Neural Network  
1072 energy estimator for Pass 5.F. A description of this estimator was provided in chapter 4. **TODO:**  
1073 **define a subsection when it’s written** All other software used for data analysis, DM profile generation,  
1074 and job submission to SLURM are also kept in my sandbox in the [Dark Matter HAWC](#) project.  
1075 The above repository also incorporates the model inputs used previously in Glory Duck, described  
1076 in chapter 7

### 1077 **8.2.3 Data Set and Background Description**

1078 The HAWC data maps used for this analysis contain 2565 days of data between runs 2104 (

1079 **TODO: Day start**) and 7476 (**TODO: day end**). They were generated from pass 4.0 reconstruction.

1080 The analysis is performed using the NN energy estimator with bin list:

1081       B1C0Ea, B1C0Eb, B1C0Ec, B1C0Ed, B1C0Ee, B2C0Ea, B2C0Eb, B2C0Ec, B2C0Ed, B2C0Ee,  
1082       B3C0Ea, B3C0Eb, B3C0Ec, B3C0Ed, B3C0Ee, B3C0Ef, B4C0Eb, B4C0Ec, B4C0Ed, B4C0Ee,  
1083       B4C0Ef, B5C0Ec, B5C0Ed, B5C0Ee, B5C0Ef, B5C0Eg, B6C0Ed, B6C0Ee, B6C0Ef, B6C0Eg,  
1084       B6C0Eh, B7C0Ee, B7C0Ef, B7C0Eg, B7C0Eh, B7C0Ei, B8C0Ee, B8C0Ef, B8C0Eg, B8C0Eh,  
1085       B8C0Ei, B8C0Ej, B9C0Ef, B9C0Eg, B9C0Eh, B9C0Ei, B9C0Ej, B10C0Eg, B10C0Eh,  
1086       B10C0Ei, B10C0Ej, B10C0Ek, B10C0El

1087 Bin 0 was excluded as it has substantial hadronic contamination and poor angular resolution.

1088 Background considerations and source selection was identical to Section 7.2, and no additional  
1089 arguments are provided here. Many of the HAWC systematics explored in Section 7.7 also apply  
1090 for this DM search and are not added upon here.

## 1091 **8.3 Analysis**

1092 The analysis and its systematics are almost identical to Section 7.3. Importantly, we use the  
1093 same Equation (7.1) and Equation (7.2) for estimating the gamma-ray flux at HAWC from our

1094 sources. We add on to the previous study with a search for DM decay. The flux equations for DM  
 1095 decay are

$$\frac{d\Phi_\gamma}{dE_\gamma} = \frac{1}{4\pi\tau m_\chi} \frac{dN_\gamma}{dE_\gamma} \times \int_{\text{source}} d\Omega \int_{l.o.s} \rho_\chi dl(r, \theta') \quad (8.1)$$

1096 with a new quantity, the  $D$  factor, defined as

$$D = \int d\Omega \int_{l.o.s} dl \rho_\chi(r, \theta') \quad (8.2)$$

1097 **8.3.1  $\frac{dN_\gamma}{dE_\gamma}$  - Particle Physics Component**

1098 For these spectra, we import HDM with Electroweak (EW) corrections and additional correc-  
 1099 tions for neutrinos above the EW scale [64]. The spectrum is implemented as a model script in  
 1100 astromodels for 3ML. A comprehensive description of EW corrections and neutrino considerations  
 1101 are provided later in [TODO: refeance MM nu duck](#).

1102 Figure 8.1 demonstrates the impact of changes from HDM on DM annihilation to W bosons.  
 1103 A class in astromodels was developed to include HDM and is aptly named `HDMspectra` within  
 1104 `DM_models.py`.

1105 **8.3.2  $J$  and  $D$ - Astrophysical Components**

1106 The J-factor profiles for each source are imported from Louis Strigari et al. (referred to with  
 1107  $\mathcal{LS}$ ) [65]. Profiles in  $\frac{dJ}{d\Omega}(\theta)$  and  $\frac{dD}{d\Omega}(\theta)$  up to  $\theta = 0.5^\circ$  were provided directly from the authors.  
 1108 Map generation from these profiles were almost identical to Section 7.3.2 except that a higher order  
 1109 trapezoidal integral was used for the normalization of the square, uniformly-spaced map:

$$p^2 \cdot \sum_{i=0}^N \sum_{j=0}^M w_{i,j} \frac{dJ}{d\Omega}(\theta_{i,j}, \phi_{i,j}) \quad (8.3)$$

1110  $p$  is the angular side of one pixel in the map.  $w_{i,j}$  is a weight assigned the following ways:

1111  $w_{i,j} = 1$  if  $\frac{dJ}{d\Omega}(\theta_{i,j}, \phi_{i,j})$  is fully within the region of integration

1112  $w_{i,j} = 1/2$  if  $\frac{dJ}{d\Omega}(\theta_{i,j}, \phi_{i,j})$  is on an edge of the region of integration

1113  $w_{i,j} = 1/4$  if  $\frac{dJ}{d\Omega}(\theta_{i,j}, \phi_{i,j})$  is on a corner of the region of integration

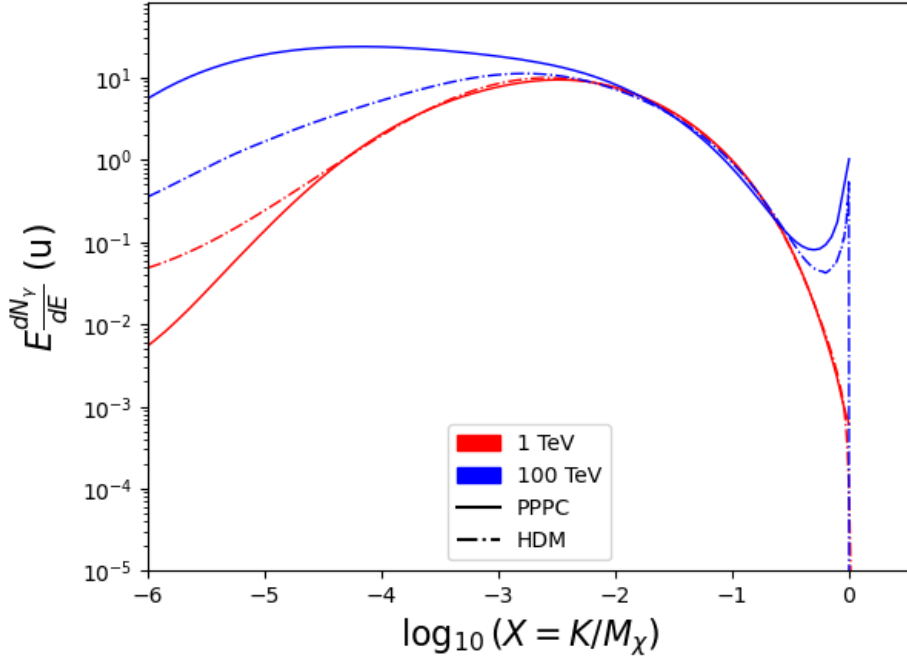


Figure 8.1 Difference between spectral hypotheses from PPPC [44] and HDM [64]. Shown is the expected DM annihilation spectrum for  $\chi\chi \rightarrow W^-W^+$ . Solid lines are spectral models with EW corrections from the PPPC. Dash-dot lines are spectral models from HDM. Red lines are models for  $M_\chi = 1$  TeV. Blue lines represent models for  $M_\chi = 100$  TeV.

1114 Maps for both annihilation and decay were generated for use in HAWC analysis in an identical  
 1115 manner.

1116  $\mathcal{LS}$  also provides profiles for  $\pm 1\sigma$  estimations to  $J$  and  $D$  for each source.

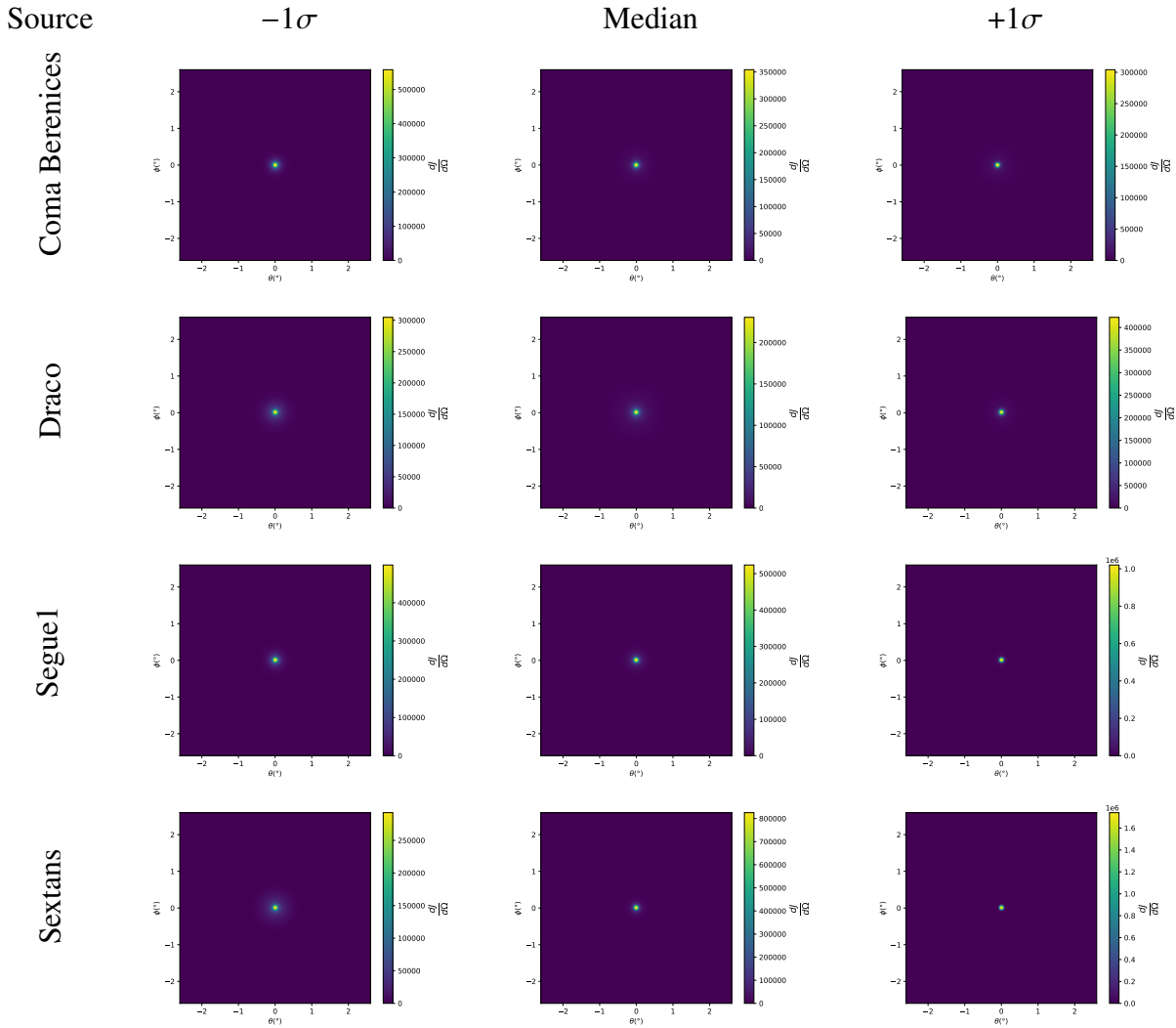


Figure 8.2 This is a caption

## **CHAPTER 9**

**1117 HEAVY DARK MATTER ANNIHILATION SEARCH WITH ICECUBE'S NORTH SKY  
1118 TRACK DATA**

## **CHAPTER 10**

### **NU DUCK**

**APPENDIX A****MULTI-EXPERIMENT SUPPLEMENTARY FIGURES**

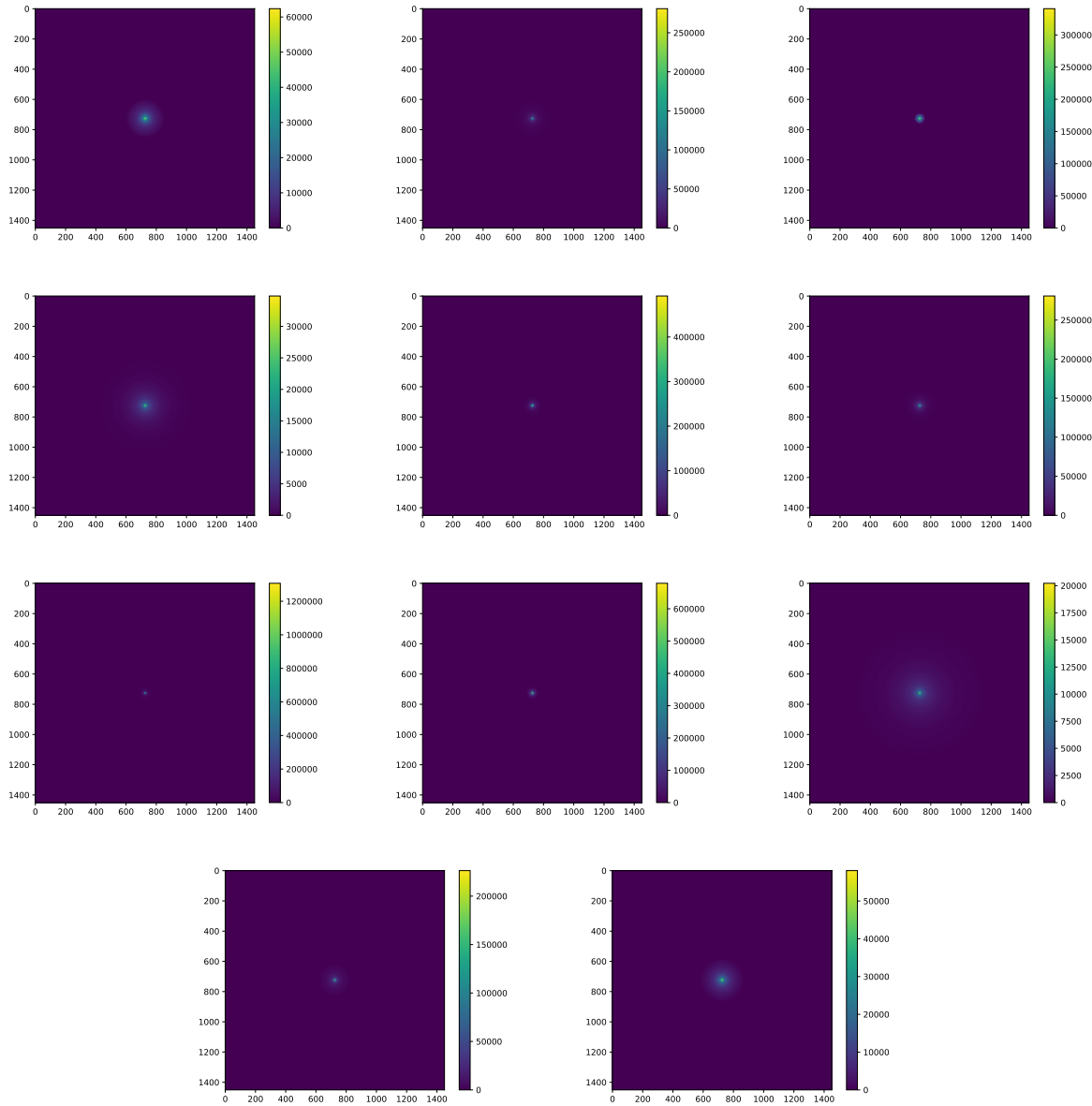


Figure A.1 Sister figure to Figure 7.3. Sources in the first row from left to right: Bootes I, Canes Venatici I, II. In second row: Draco, Hercules, Leo I. In the first row: Leo II, Leo IV, Sextans. In the final row: Ursa Major I, Ursa Major II.

## BIBLIOGRAPHY

- 1122 [1] Anne M. Green. “Dark matter in astrophysics/cosmology”. In: *SciPost Phys. Lect.*  
 1123 *Notes* (2022), p. 37. doi: [10.21468/SciPostPhysLectNotes.37](https://doi.org/10.21468/SciPostPhysLectNotes.37). URL: <https://scipost.org/10.21468/SciPostPhysLectNotes.37>.
- 1125 [2] Bing-Lin Young. “A survey of dark matter and related topics in cosmology”. In: *Frontiers*  
 1126 *of Physics* 12 (Oct. 2016). doi: <https://doi.org/10.1007/s11467-016-0583-4>.  
 1127 URL: <https://doi.org/10.1007/s11467-016-0583-4>.
- 1128 [3] Gianfranco Bertone, Dan Hooper, and Joseph Silk. “Particle dark matter: evidence,  
 1129 candidates and constraints”. In: *Physics Reports* 405.5 (2005), pp. 279–390. ISSN:  
 1130 0370-1573. doi: <https://doi.org/10.1016/j.physrep.2004.08.031>. URL:  
 1131 <https://www.sciencedirect.com/science/article/pii/S0370157304003515>.
- 1132 [4] Gianfranco Bertone and Dan Hooper. “History of dark matter”. In: *Rev. Mod. Phys.*  
 1133 90 (4 Aug. 2018), p. 045002. doi: [10.1103/RevModPhys.90.045002](https://doi.org/10.1103/RevModPhys.90.045002). URL: <https://link.aps.org/doi/10.1103/RevModPhys.90.045002>.
- 1135 [5] Fritz Zwicky. “The Redshift of Extragalactic Nebulae”. In: *Helvetica Physica Acta* 6.  
 1136 (1933), pp. 110–127. doi: [10.5169/seals-110267](https://doi.org/10.5169/seals-110267).
- 1137 [6] Vera C. Rubin and Jr. Ford W. Kent. “Rotation of the Andromeda Nebula from a  
 1138 Spectroscopic Survey of Emission Regions”. In: *ApJ* 159 (Feb. 1970), p. 379. doi:  
 1139 [10.1086/150317](https://doi.org/10.1086/150317).
- 1140 [7] K. G. Begeman, A. H. Broeils, and R. H. Sanders. “Extended rotation curves of spiral galax-  
 1141 ies: dark haloes and modified dynamics”. In: *Monthly Notices of the Royal Astronomical So-*  
 1142 *ciety* 249.3 (Apr. 1991), pp. 523–537. ISSN: 0035-8711. doi: [10.1093/mnras/249.3.523](https://doi.org/10.1093/mnras/249.3.523).  
 1143 eprint: <https://academic.oup.com/mnras/article-pdf/249/3/523/18160929/mnras249-0523.pdf>. URL: <https://doi.org/10.1093/mnras/249.3.523>.
- 1145 [8] *Different types of gravitational lenses*. website. Feb. 2004. URL: <https://esahubble.org/images/heic0404b/>.
- 1147 [9] Douglas Clowe et al. “A Direct Empirical Proof of the Existence of Dark Matter”. In: *apjl*  
 1148 648.2 (Sept. 2006), pp. L109–L113. doi: [10.1086/508162](https://doi.org/10.1086/508162). arXiv: [astro-ph/0608407](https://arxiv.org/abs/astro-ph/0608407)  
 1149 [[astro-ph](#)].
- 1150 [10] Planck Collaboration and N. et. al. Aghanim. “Planck 2018 results I. Overview and the  
 1151 cosmological legacy of Planck”. In: *A&A* 641 (2020). doi: [10.1051/0004-6361/201833880](https://doi.org/10.1051/0004-6361/201833880). URL: <https://doi.org/10.1051/0004-6361/201833880>.
- 1153 [11] Wayne Hu. *Matter Density Animation*. web. 2024. URL: <http://background.uchicago.edu/~whu/animbut/anim2.html>.

- 1155 [12] Wenlong Yuan et al. “A First Look at Cepheids in a Type Ia Supernova Host with JWST”. in:  
1156 *The Astrophysical Journal Letters* 940.1 (Nov. 2022). doi: [10.3847/2041-8213/ac9b27](https://doi.org/10.3847/2041-8213/ac9b27).  
1157 URL: <https://dx.doi.org/10.3847/2041-8213/ac9b27>.
- 1158 [13] Wendy L. Freedman. “Measurements of the Hubble Constant: Tensions in Perspective”. In:  
1159 *The Astrophysical Journal* 919.1 (Sept. 2021), p. 16. doi: [10.3847/1538-4357/ac0e95](https://doi.org/10.3847/1538-4357/ac0e95).  
1160 URL: <https://dx.doi.org/10.3847/1538-4357/ac0e95>.
- 1161 [14] Jodi Cooley. “Dark Matter direct detection of classical WIMPs”. In: *SciPost Phys. Lect.  
1162 Notes* (2022), p. 55. doi: [10.21468/SciPostPhysLectNotes.55](https://doi.org/10.21468/SciPostPhysLectNotes.55). URL: <https://scipost.org/10.21468/SciPostPhysLectNotes.55>.
- 1164 [15] “Search for new phenomena in events with an energetic jet and missing transverse momentum  
1165 in  $pp$  collisions at  $\sqrt{s} = 13$  TeV with the ATLAS detector”. In: *Phys. Rev. D* 103  
1166 (11 July 2021), p. 112006. doi: [10.1103/PhysRevD.103.112006](https://doi.org/10.1103/PhysRevD.103.112006). URL: <https://link.aps.org/doi/10.1103/PhysRevD.103.112006>.
- 1168 [16] *Jetting into the dark side: a precision search for dark matter*. website. July 2020. URL:  
1169 <https://atlas.cern/updates/briefing/precision-search-dark-matter>.
- 1170 [17] Celine Armand et. al. “Combined dark matter searches towards dwarf spheroidal galaxies  
1171 with Fermi-LAT, HAWC, H.E.S.S., MAGIC, and VERITAS”. in: *Proceedings of Science*.  
1172 Vol. 395. Mar. 2022. doi: <https://doi.org/10.22323/1.395.0528>.
- 1173 [18] Tracy R. Slatyer. “Les Houches Lectures on Indirect Detection of Dark Matter”. In: *SciPost  
1174 Phys. Lect. Notes* (2022), p. 53. doi: [10.21468/SciPostPhysLectNotes.53](https://doi.org/10.21468/SciPostPhysLectNotes.53). URL:  
1175 <https://scipost.org/10.21468/SciPostPhysLectNotes.53>.
- 1176 [19] Christian W Bauer, Nicholas L. Rodd, and Bryan R. Webber. “Dark matter spectra from  
1177 the electroweak to the Planck scale”. In: *Journal of High Energy Physics* 2021.1029-8479  
1178 (June 2021). doi: [https://doi.org/10.1007/JHEP06\(2021\)121](https://doi.org/10.1007/JHEP06(2021)121).
- 1179 [20] Riccardo Catena and Piero Ullio. “A novel determination of the local dark matter density”.  
1180 In: *Journal of Cosmology and Astroparticle Physics* 2010.08 (Aug. 2010), p. 004. doi:  
1181 [10.1088/1475-7516/2010/08/004](https://doi.org/10.1088/1475-7516/2010/08/004). URL: <https://dx.doi.org/10.1088/1475-7516/2010/08/004>.
- 1183 [21] B. P. Abbott et al. “Observation of Gravitational Waves from a Binary Black Hole Merger”.  
1184 In: *Phys. Rev. Lett.* 116 (6 Feb. 2016), p. 061102. doi: [10.1103/PhysRevLett.116.061102](https://doi.org/10.1103/PhysRevLett.116.061102). URL: <https://link.aps.org/doi/10.1103/PhysRevLett.116.061102>.
- 1186 [22] R. Abbasi et. al. “Observation of high-energy neutrinos from the Galactic plane”. In: *Science*  
1187 380.6652 (June 2023), pp. 1338–1343.
- 1188 [23] NASA Goddard Space Flight Center. *Fermi’s 12-year view of the gamma-ray sky*. website.

- 1189 2022. URL: <https://svs.gsfc.nasa.gov/14090>.
- 1190 [24] Marco Cirelli et al. “PPPC 4 DM ID: a poor particle physicist cookbook for dark matter  
1191 indirect detection”. In: *Journal of Cosmology and Astroparticle Physics* 2011.03 (Mar.  
1192 2011), p. 051. doi: [10.1088/1475-7516/2011/03/051](https://doi.org/10.1088/1475-7516/2011/03/051). URL: <https://dx.doi.org/10.1088/1475-7516/2011/03/051>.
- 1194 [25] Javier Rico. “Gamma-Ray Dark Matter Searches in Milky Way Satellites—A Comparative  
1195 Review of Data Analysis Methods and Current Results”. In: *Galaxies* 8.1 (Mar. 2020), p. 25.  
1196 doi: [10.3390/galaxies8010025](https://doi.org/10.3390/galaxies8010025). arXiv: [2003.13482](https://arxiv.org/abs/2003.13482) [astro-ph.HE].
- 1197 [26] W. B. Atwood et al. “The Large Area Telescope on the Fermi Gamma-Ray Space Telescope  
1198 Mission”. In: *apj* 697.2 (June 2009), pp. 1071–1102. doi: [10.1088/0004-637X/697/2/1071](https://doi.org/10.1088/0004-637X/697/2/1071). arXiv: [0902.1089](https://arxiv.org/abs/0902.1089) [astro-ph.IM].
- 1200 [27] M. Ackermann et al. “Searching for Dark Matter Annihilation from Milky Way Dwarf  
1201 Spheroidal Galaxies with Six Years of Fermi Large Area Telescope Data”. In: *prl* 115.23,  
1202 231301 (Dec. 2015), p. 231301. doi: [10.1103/PhysRevLett.115.231301](https://doi.org/10.1103/PhysRevLett.115.231301). arXiv:  
1203 [1503.02641](https://arxiv.org/abs/1503.02641) [astro-ph.HE].
- 1204 [28] Mattia Di Mauro, Martin Stref, and Francesca Calore. “Investigating the effect of Milky  
1205 Way dwarf spheroidal galaxies extension on dark matter searches with Fermi-LAT data”.  
1206 In: *Phys. Rev. D* 106 (12 Dec. 2022), p. 123032. doi: [10.1103/PhysRevD.106.123032](https://doi.org/10.1103/PhysRevD.106.123032).  
1207 URL: <https://link.aps.org/doi/10.1103/PhysRevD.106.123032>.
- 1208 [29] F. et al. Aharonian. “Observations of the Crab Nebula with H.E.S.S.”. In: *Astron. Astrophys.*  
1209 457 (2006), pp. 899–915. doi: [10.1051/0004-6361:20065351](https://doi.org/10.1051/0004-6361:20065351). arXiv: [astro-ph/0607333](https://arxiv.org/abs/astro-ph/0607333).
- 1211 [30] J. Albert et al. “VHE  $\gamma$ -Ray Observation of the Crab Nebula and its Pulsar with the MAGIC  
1212 Telescope”. In: *The Astrophysical Journal* 674.2 (Feb. 2008), p. 1037. doi: [10.1086/525270](https://doi.org/10.1086/525270). URL: <https://dx.doi.org/10.1086/525270>.
- 1214 [31] N. Park. “Performance of the VERITAS experiment”. In: *Proceedings, 34th International  
1215 Cosmic Ray Conference (ICRC2015): The Hague, The Netherlands, July, 30th July - 6th  
1216 August*. Vol. 34. 2015, p. 771. arXiv: [1508.07070](https://arxiv.org/abs/1508.07070) [astro-ph.IM].
- 1217 [32] A. Abramowski et al. “H.E.S.S. constraints on Dark Matter annihilations towards the Sculptor  
1218 and Carina Dwarf Galaxies”. In: *Astropart. Phys.* 34 (2011), pp. 608–616. doi: [10.1016/j.astropartphys.2010.12.006](https://doi.org/10.1016/j.astropartphys.2010.12.006). arXiv: [1012.5602](https://arxiv.org/abs/1012.5602) [astro-ph.HE].
- 1220 [33] A. Abramowski et al. “Search for dark matter annihilation signatures in H.E.S.S. observations  
1221 of Dwarf Spheroidal Galaxies”. In: *Phys. Rev. D* 90 (2014), p. 112012. doi: [10.1103/PhysRevD.90.112012](https://doi.org/10.1103/PhysRevD.90.112012). arXiv: [1410.2589](https://arxiv.org/abs/1410.2589) [astro-ph.HE].

- 1223 [34] H. Abdalla et al. “Searches for gamma-ray lines and ‘pure WIMP’ spectra from Dark  
1224 Matter annihilations in dwarf galaxies with H.E.S.S”. in: *JCAP* 11 (2018), p. 037. doi:  
1225 [10.1088/1475-7516/2018/11/037](https://doi.org/10.1088/1475-7516/2018/11/037). arXiv: [1810.00995 \[astro-ph.HE\]](https://arxiv.org/abs/1810.00995).
- 1226 [35] J. Aleksić et al. “Optimized dark matter searches in deep observations of Segue 1 with  
1227 MAGIC”. in: *JCAP* 1402 (2014), p. 008. doi: [10.1088/1475-7516/2014/02/008](https://doi.org/10.1088/1475-7516/2014/02/008).  
1228 arXiv: [1312.1535 \[hep-ph\]](https://arxiv.org/abs/1312.1535).
- 1229 [36] V.A. Acciari et al. “Combined searches for dark matter in dwarf spheroidal galaxies observed  
1230 with the MAGIC telescopes, including new data from Coma Berenices and Draco”. In: *Physics of the Dark Universe* (2021), p. 100912. issn: 2212-6864. doi: <https://doi.org/10.1016/j.dark.2021.100912>. URL: <https://www.sciencedirect.com/science/article/pii/S2212686421001370>.
- 1234 [37] M. L. Ahnen et al. “Indirect dark matter searches in the dwarf satellite galaxy Ursa Major II  
1235 with the MAGIC Telescopes”. In: *JCAP* 1803.03 (2018), p. 009. doi: [10.1088/1475-7516/2018/03/009](https://doi.org/10.1088/1475-7516/2018/03/009). arXiv: [1712.03095 \[astro-ph.HE\]](https://arxiv.org/abs/1712.03095).
- 1237 [38] S. et al. Archambault. “Dark matter constraints from a joint analysis of dwarf Spheroidal  
1238 galaxy observations with VERITAS”. in: *prd* 95.8 (Apr. 2017). doi: [10.1103/PhysRevD.95.082001](https://doi.org/10.1103/PhysRevD.95.082001). arXiv: [1703.04937 \[astro-ph.HE\]](https://arxiv.org/abs/1703.04937).
- 1240 [39] Louise Oakes et al. “Combined Dark Matter searches towards dwarf spheroidal galaxies with  
1241 Fermi-LAT, HAWC, HESS, MAGIC and VERITAS”. in: *Proceedings of Science*. 2019.
- 1242 [40] Celine Armand et al. on behalf of the Fermi-LAT, HAWC, HESS, MAGIC, VERITAS.  
1243 “Combined Dark Matter searches towards dwarf spheroidal galaxies with Fermi-LAT,  
1244 HAWC, HESS, MAGIC and VERITAS”. in: *Proceedings of Science*. 2021.
- 1245 [41] Daniel Kerszberg et al. on behalf of the Fermi-LAT, HAWC, HESS, MAGIC, and VER-  
1246 TIAS collaborations. “Search for dark matter annihilation with a combined analysis of  
1247 dwarf spheroidal galaxies from Fermi-LAT, HAWC, H.E.S.S., MAGIC and VERITAS”. in:  
1248 *Proceedings of Science*. 2023.
- 1249 [42] A. U. Abeysekara et al. “Observation of the Crab Nebula with the HAWC Gamma-Ray  
1250 Observatory”. In: *The Astrophysical Journal* 843.1 (June 2017), p. 39. doi: [10.3847/1538-4357/aa7555](https://doi.org/10.3847/1538-4357/aa7555). URL: <https://doi.org/10.3847/1538-4357/aa7555>.
- 1252 [43] Giacomo Vianello et al. *The Multi-Mission Maximum Likelihood framework (3ML)*. 2015.  
1253 arXiv: [1507.08343 \[astro-ph.HE\]](https://arxiv.org/abs/1507.08343).
- 1254 [44] Marco Cirelli et al. “PPPC 4 DM ID: a poor particle physicist cookbook for dark matter  
1255 indirect detection”. In: *Journal of Cosmology and Astroparticle Physics* 2011.03 (Mar.  
1256 2011). issn: 1475-7516. doi: [10.1088/1475-7516/2011/03/051](https://doi.org/10.1088/1475-7516/2011/03/051). URL: <http://dx.doi.org/10.1088/1475-7516/2011/03/051>.

- 1258 [45] Alex Geringer-Sameth, Savvas M. Koushiappas, and Matthew Walker. “DWARF GALAXY  
1259 ANNIHILATION AND DECAY EMISSION PROFILES FOR DARK MATTER EXPERI-  
1260 MENTS”. in: *The Astrophysical Journal* 801.2 (Mar. 2015), p. 74. ISSN: 1538-4357. doi:  
1261 [10.1088/0004-637X/801/2/74](https://doi.org/10.1088/0004-637X/801/2/74). URL: <http://dx.doi.org/10.1088/0004-637X/801/2/74>.
- 1263 [46] A. Albert et al. “Dark Matter Limits from Dwarf Spheroidal Galaxies with the HAWC  
1264 Gamma-Ray Observatory”. In: *The Astrophysical Journal* 853.2 (Feb. 2018), p. 154. ISSN:  
1265 1538-4357. doi: [10.3847/1538-4357/aaa6d8](https://doi.org/10.3847/1538-4357/aaa6d8). URL: <http://dx.doi.org/10.3847/1538-4357/aaa6d8>.
- 1267 [47] V. Bonnivard et al. “Spherical Jeans analysis for dark matter indirect detection in dwarf  
1268 spheroidal galaxies - Impact of physical parameters and triaxiality”. In: *Mon. Not. Roy.  
1269 Astron. Soc.* 446 (2015), pp. 3002–3021. doi: [10.1093/mnras/stu2296](https://doi.org/10.1093/mnras/stu2296). arXiv:  
1270 [1407.7822 \[astro-ph.HE\]](https://arxiv.org/abs/1407.7822).
- 1271 [48] M. Ackermann et al. “Searching for Dark Matter Annihilation from Milky Way Dwarf  
1272 Spheroidal Galaxies with Six Years of Fermi Large Area Telescope Data”. In: *prl* 115.23,  
1273 231301 (Dec. 2015), p. 231301. doi: [10.1103/PhysRevLett.115.231301](https://doi.org/10.1103/PhysRevLett.115.231301). arXiv:  
1274 [1503.02641 \[astro-ph.HE\]](https://arxiv.org/abs/1503.02641).
- 1275 [49] M. L. Ahnen et al. “Limits to Dark Matter Annihilation Cross-Section from a Combined  
1276 Analysis of MAGIC and Fermi-LAT Observations of Dwarf Satellite Galaxies”. In: *JCAP*  
1277 1602.02 (2016), p. 039. doi: [10.1088/1475-7516/2016/02/039](https://doi.org/10.1088/1475-7516/2016/02/039). arXiv: [1601.06590](https://arxiv.org/abs/1601.06590)  
1278 [astro-ph.HE].
- 1279 [50] Javier Rico et al. *gLike: numerical maximization of heterogeneous joint  
1280 likelihood functions of a common free parameter plus nuisance parameters*.  
1281 <https://doi.org/10.5281/zenodo.4601451>. Version v0.09.03. Mar. 2021. doi: [10.5281/zenodo.4601451](https://doi.org/10.5281/zenodo.4601451). URL: <https://doi.org/10.5281/zenodo.4601451>.
- 1283 [51] Tjark Miener and Daniel Nieto. *LklCom: Combining likelihoods from different experiments*.  
1284 <https://doi.org/10.5281/zenodo.4597500>. Version v0.5.3. Mar. 2021. doi: [10.5281/zenodo.4597500](https://doi.org/10.5281/zenodo.4597500). URL: <https://doi.org/10.5281/zenodo.4597500>.
- 1286 [52] T. Miener et al. “Open-source Analysis Tools for Multi-instrument Dark Matter Searches”.  
1287 In: *arXiv e-prints*, arXiv:2112.01818 (Dec. 2021), arXiv:2112.01818. arXiv: [2112.01818](https://arxiv.org/abs/2112.01818)  
1288 [astro-ph.IM].
- 1289 [53] Alex Geringer-Sameth and Matthew Koushiappas Savvas M. and Walker. “Dwarf galaxy  
1290 annihilation and decay emission profiles for dark matter experiments”. In: *Astrophys.  
1291 J.* 801.2 (2015), p. 74. doi: [10.1088/0004-637X/801/2/74](https://doi.org/10.1088/0004-637X/801/2/74). arXiv: [1408.0002](https://arxiv.org/abs/1408.0002)  
1292 [astro-ph.CO].
- 1293 [54] Gianfranco Bertone, Dan Hooper, and Joseph Silk. “Particle dark matter: evidence, can-

- 1294 didates and constraints”. In: *Physics Reports* 405.5-6 (Jan. 2005), pp. 279–390. ISSN:  
1295 0370-1573. doi: [10.1016/j.physrep.2004.08.031](https://doi.org/10.1016/j.physrep.2004.08.031). URL: <http://dx.doi.org/10.1016/j.physrep.2004.08.031>.
- 1297 [55] V. Bonnivard et al. “Dark matter annihilation and decay in dwarf spheroidal galaxies: The  
1298 classical and ultrafaint dSphs”. In: *Mon. Not. Roy. Astron. Soc.* 453.1 (2015), pp. 849–867.  
1299 doi: [10.1093/mnras/stv1601](https://doi.org/10.1093/mnras/stv1601). arXiv: [1504.02048 \[astro-ph.HE\]](https://arxiv.org/abs/1504.02048).
- 1300 [56] A. et al. Albert. “Searching for Dark Matter Annihilation in Recently Discovered Milky Way  
1301 Satellites with Fermi-LAT”. in: *Astrophys. J.* 834.2 (2017), p. 110. doi: [10.3847/1538-4357/834/2/110](https://doi.org/10.3847/1538-4357/834/2/110). arXiv: [1611.03184 \[astro-ph.HE\]](https://arxiv.org/abs/1611.03184).
- 1303 [57] Mattia Di Mauro and Martin Wolfgang Winkler. “Multimessenger constraints on the dark  
1304 matter interpretation of the Fermi-LAT Galactic Center excess”. In: *prd* 103.12, 123005  
1305 (June 2021), p. 123005. doi: [10.1103/PhysRevD.103.123005](https://doi.org/10.1103/PhysRevD.103.123005). arXiv: [2101.11027 \[astro-ph.HE\]](https://arxiv.org/abs/2101.11027).
- 1307 [58] HongSheng Zhao. “Analytical models for galactic nuclei”. In: *Mon. Not. Roy. Astron. Soc.*  
1308 278 (1996), pp. 488–496. doi: [10.1093/mnras/278.2.488](https://doi.org/10.1093/mnras/278.2.488). arXiv: [astro-ph/9509122 \[astro-ph\]](https://arxiv.org/abs/astro-ph/9509122).
- 1310 [59] H. C. Plummer. “On the Problem of Distribution in Globular Star Clusters: (Plate 8.)”  
1311 In: *Monthly Notices of the Royal Astronomical Society* 71.5 (Mar. 1911), pp. 460–470.  
1312 ISSN: 0035-8711. doi: [10.1093/mnras/71.5.460](https://doi.org/10.1093/mnras/71.5.460). eprint: <https://academic.oup.com/mnras/article-pdf/71/5/460/2937497/mnras71-0460.pdf>. URL:  
1314 <https://doi.org/10.1093/mnras/71.5.460>.
- 1315 [60] Daniel R. Hunter. “Derivation of the anisotropy profile, constraints on the local velocity  
1316 dispersion, and implications for direct detection”. In: *JCAP* 02 (2014), p. 023. doi:  
1317 [10.1088/1475-7516/2014/02/023](https://doi.org/10.1088/1475-7516/2014/02/023). arXiv: [1311.0256 \[astro-ph.CO\]](https://arxiv.org/abs/1311.0256).
- 1318 [61] Barun Kumar Dhar and Liliya L. R. Williams. “Surface mass density of the Einasto family  
1319 of dark matter haloes: are they Sersic-like?” In: *Mon. Not. Roy. Astron. Soc.* (2010). doi:  
1320 [10.1111/j.1365-2966.2010.16446.x](https://doi.org/10.1111/j.1365-2966.2010.16446.x).
- 1321 [62] M. Baes and E. Van Hese. “Dynamical models with a general anisotropy profile”. In:  
1322 *Astron. Astrophys.* 471 (2007), p. 419. doi: [10.1051/0004-6361:20077672](https://doi.org/10.1051/0004-6361:20077672). arXiv:  
1323 [0705.4109 \[astro-ph\]](https://arxiv.org/abs/0705.4109).
- 1324 [63] Matthew G. Walker, Edward W. Olszewski, and Mario Mateo. “Bayesian analysis of re-  
1325 solved stellar spectra: application to MMT/Hectochelle observations of the Draco dwarf  
1326 spheroidal”. In: *mnras* 448.3 (Apr. 2015), pp. 2717–2732. doi: [10.1093/mnras/stv099](https://doi.org/10.1093/mnras/stv099).  
1327 arXiv: [1503.02589 \[astro-ph.GA\]](https://arxiv.org/abs/1503.02589).
- 1328 [64] Nicholas L. Rodd et al. “Dark matter spectra from the electroweak to the Planck scale”. In:

- 1329            *J. High Energy Physics* 121.10.1007 (June 2021).
- 1330 [65] Pace, Andrew B and Strigari, Louis E. “Scaling relations for dark matter annihilation and  
1331 decay profiles in dwarf spheroidal galaxies”. In: *Monthly Notices of the Royal Astronomical  
1332 Society* 482.3 (Oct. 2018), pp. 3480–3496. ISSN: 0035-8711. doi: [10.1093/mnras/sty2839](https://doi.org/10.1093/mnras/sty2839).
- 1333